Design of New Wearable Antennas and Textile-based Transmission Lines

Rahil Joshi

Submitted for the degree of Doctor of Philosophy

School of Engineering & Physical Sciences

Heriot-Watt University

Edinburgh, United Kingdom

May 2020

Abstract

Flexible wearable antennas and their components are a fast growing research topic in modern communication systems. They are developed for various wearable applications, such as health monitoring, fitness tracking, rescuing, and telecommunications. Wearable antennas need to be compact, lightweight, flexible, and robust.

In this thesis, two dual-band wearable antennas were developed, each with a different design approach. The first antenna is a dual-band flexible folded shorted patch (FSP) antenna which operates at 400 MHz and 2.4 GHz. It uses polydimethylsiloxane (PDMS), which is low cost, flexible and robust, and is used as a substrate for wearable the FSP antenna. In addition, the FSP antenna also exploits the TM_{010} and TM_{001} modes. A comparative study was carried out to analyze the far-field radiation and directivity at the TM_{010} and TM_{001} modes between the FSP antenna and a conventional patch antenna using cavity model analysis. The proposed FSP antenna is suitable for military search and rescue operations and emergency services.

The second antenna is a dual-band flexible circular polarized (CP) patch antenna operational at 1.575 GHz and 2.45 GHz. Kevlar was used as a substrate for the proposed antenna. The patch consists of truncated corners and four diagonal slits. An artificial magnetic conductor (AMC) plane was integrated within the design in order to reduce the backward scattered radiation towards the human body and also to improve the realized gain of the antenna. The AMC unit cell design consists of square slits, a square ring and was integrated as a 3×3 array of square patch AMC unit cells. The proposed antenna developed is suitable for WBAN and WLAN applications.

A circular polarized (CP) patch antenna with a PDMS substrate was also designed and fabricated to test the durability and resiliency of PDMS as a polymer-based material suitable for use in wearable antennas. Robustness tests such as bent, wet,

and temperature tests were performed and reported.

Two prototypes of flexible wearable coaxial transmission lines were also designed and fabricated. Polyester (PES) and polytetrafluoroethylene (PTFE) textile materials were used to design prototypes of these cables. Shielding effectiveness and DC losses were measured and compared for the fabricated cables. The cables were also tested for bending, twisting and for suitability in environmental conditions. The highly flexible nature of these cables makes them suitable to use with wearable antennas for various applications. For example, the proposed cables can be used with previously detailed FPS antenna for military search and rescue operations.

It should be mentioned that this thesis was done in collaboration with Leonardo, UK and J&D Wilkie, UK.

Dedication

To mom, dad and uncle for being my constant role models and supporting hand throughout different stages of my life so far.

Acknowledgements

I would like to give my most sincere infinite thanks to my supervisor Dr. Symon K. Podilchak for his constant motivation, guidance and most importantly believing in me. His knowledge, support and positive attitude was always refreshing which helped me shape my research.

I would also like to thank my supervisor Dr. Dimitris Anagnostou for his guidance and knowledge which helped me develop my research. I would like to extend my sincere gratitude toward Dr. Ping Jack Soh and his team from Universiti Malaysia, Perlis who are experts in wearable antennas technologies, from whom I acquired invaluable knowledge that helped me during my research. Words are not enough to thank Dr. Constantin Constantinides who was my mentor and friend when I started my Ph.D.

I need to express my immense and countless thanks to the extraordinary talents Barry, Gordon, Gary and Steven Selkirk, who work in the electronics workshop at Heriot-Watt University. A very special thanks to Andrew Houston (Andy) who had been patient and saved with my antenna structures from being a complete disaster.

I would like to express my heartiest thanks to my dearest friend Vicky who has always by my side during my Ph.D. This whole journey would have never been possible without the support and help from all my dear colleagues who made this process easier and became my second family, Alexios Costouri, Salvatore Liberto, Simona Sibo, Spyridon Daskalakis, Eva Bergmen, Khaled Aliqab, Rafael Adorna, Cristian Alistarh, María Jesús Cañavate, Panagiota Kontou, Konstantin Kossenas, Yuepei Li, Callum Hodgkinson, Florian Vidal, Clare Bentyne, Louis Dufour, Charalampos (Harris) Stoumpos, Zain Shafiq and Romwald Lihakanga.

Special thanks to Francesco Rigobello and Salvador Mercader Pellicer for handling

Research Thesis Submission

Please note this form should be bound into the submitted thesis.

Name:	Rahil Joshi		
School:	ISSS, EPS		
Version: *(i.e. First, Resubmission, Final)*	Final	Degree Sought:	Ph.D. Electrical Engineering

Declaration

In accordance with the appropriate regulations I hereby submit my thesis and I declare that:

1. The thesis embodies the results of my own work and has been composed by myself
2. Where appropriate, I have made acknowledgement of the work of others
3. The thesis is the correct version for submission and is the same version as any electronic versions submitted*.
4. My thesis for the award referred to, deposited in the Heriot-Watt University Library, should be made available for loan or photocopying and be available via the Institutional Repository, subject to such conditions as the Librarian may require
5. I understand that as a student of the University I am required to abide by the Regulations of the University and to conform to its discipline.
6. I confirm that the thesis has been verified against plagiarism via an approved plagiarism detection application e.g. Turnitin.

ONLY for submissions including published works

Please note you are only required to complete the Inclusion of Published Works Form (page 2) if your thesis contains published works)

7. Where the thesis contains published outputs under Regulation 6 (9.1.2) or Regulation 43 (9) these are accompanied by a critical review which accurately describes my contribution to the research and, for multi-author outputs, a signed declaration indicating the contribution of each author (complete)
8. Inclusion of published outputs under Regulation 6 (9.1.2) or Regulation 43 (9) shall not constitute plagiarism.

*   *Please note that it is the responsibility of the candidate to ensure that the correct version of the thesis is submitted.*

Signature of Candidate:	Rahil Joshi	Date:	30.08.2020

Submission

Submitted By *(name in capitals):*	RAHIL JOSHI
Signature of Individual Submitting:	Rahil Joshi
Date Submitted:	30.08.2020

For Completion in the Student Service Centre (SSC)

Limited Access	Requested	Yes		No		Approved	Yes		No	
*E-thesis Submitted (**mandatory for final theses)**										
Received in the SSC by *(name in capitals):*						Date:				

Inclusion of Published Works

Please note you are only required to complete the Inclusion of Published Works Form if your thesis contains published works under Regulation 6 (9.1.2)

Declaration

This thesis contains one or more multi-author published works. In accordance with Regulation 6 (9.1.2) I hereby declare that the contributions of each author to these publications is as follows:

Citation details	R. Joshi, S. K. Podilchak, D. Anagnostou, C. Constantinides, M. N. Ramli, H. Lago and P. J. Soh, "Analysis and Design of Dual-Band Folded Shorted Patch Antennas for Robust Wearable Applications," *IEEE Open Journal of Antennas and Propagation*, vol 1, pp. 239-252, 2020, doi: 10.1109/OJAP.2020.2991343.
R. Joshi	Theoretical analysis, simulations, measurements, post-processing and writing of the paper.
S. K. Podilchak, D. Anagnostou and P.J. Soh	Supervision, guidance, corrections
Signature	Rahil Joshi
Date:	30.08.2020

Citation details	R. Joshi, E. F. N. M. Hussin, P. J. Soh, M. F. Jamlos, H. Lago, A. A. Al-Haldi and S. K. Podilchak, "Dual-Band, Dual-Sense Textile Antenna with AMC Backing for Localization using GPS and WBAN/WLAN," in *IEEE Access,* vol. 8, pp. 89468-89478, 2020, doi: 10.1109/ACCESS.2020.2993371.
R. Joshi	Theoretical analysis, simulations, measurements, post-processing, optimization and writing of the paper.
E. F. N. M. Hussin	Simulations, measurement and manufacturing.
S. K. Podilchak and P. J. Soh	Supervison, guidance and correction
Signature:	Rahil Joshi
Date:	30.08.2020

Please included additional citations as required.

Contents

List of Figures

List of Tables

Glossary

TM	Transverse magnetic
WBAN	Wireless body area network
UWB	Ultra wideband
PIFA	Planar inverted F antenna
GSM	Global system for mobile communications
WLAN	Wireless local area network
GPS	Global positioning system
LCP	Liquid crystal polymer
PDMS	Polydimethylsiloxane
RFID	Radio frequency identification
EBG	Electromagnetic bandgap
HIS	High impedance surface
AMC	Artificial magnetic conductor
PMS	Perfect magnetic conductor
SAR	Specific absorption rate
FSP	Folded-shorted patch
CP	Circular polarized
ISM	Industrial, scientific and medical
MIMO	Multiple input multiple output
UV	Ultra violet
RPA	Rectangular patch antenna

TE	Transverse electric
TEM	Transverse electromagnetic
FBW	Fractional bandwidth
UHF	Ultra high frequency
IFA	Inverted F antenna
BW	Bandwidth
PRS	Partial reflected surface
RF	Radio Frequency
EMI	Electromagnetic interfernce
PES	Polyester
PTFE	Polytetrafluoroethylene
VNA	Vector network analyzer

List of Scalar Symbols

c Speed of light

f Frequency

μ Permeability

μ_r Relative dielectric permeability

ω Angular frequency

ϵ Permittivity

η Intrinsic impedance of the medium

k Wavenumber

Z Input Impedance

R Real resistance

X Complex reactance

R_R Radiation resistance

R_L Loss resistance

Q Quality factor

δ_{eff} Effective loss tangent

ϵ_r Relative dielectric permittivity/constant

L Length

H Height

W Width

AF Array factor

U_{max} Maximum radiation intensity

D Directivity

U_o Radiation intensity of the isotropic source

P_{rad} Radiated power

r_i	Radius of inner conductor
r_o	Radius of the inner layer of an outer conductor
Z_o	Characteristic impedance
D_o	Diameter of the inner layer of outer conductor
D_i	Diameter of the inner conductor
α	Attenuation constant
α_c	Attenuation constant due to conductor loss
α_d	Attenuation constant due to dielectric loss
λ	Wavelength
λ_o	Free-space wavelength
λ_g	Guided wavelength
ϵ_r	Relatove dielectric permittivity
ϵ_{reff}	Effective relative dielectric permittivity/constant

List of Vector Symbols

$\mathbf{R}$	Distance from any point in the source to the observation
$\hat{\mathbf{n}}$	Normal unit vector
$\mathbf{E}$	Electric field
$\mathbf{H}$	Magnetic field
$\mathbf{J}$	Electric current density
$\mathbf{M}$	Magnetic current density
$\mathbf{A}$	Electric vector potential
$\mathbf{F}$	Magnetic Vector potential
$\mathbf{J_s}$	Electric current density in closed surface
$\mathbf{M_s}$	Magnetic current density in closed surface
r, θ, ϕ	Components of spherical coordinate system
$\hat{\mathbf{a}}_r, \hat{\mathbf{a}}_\theta, \hat{\mathbf{a}}_\phi$	Unit vector associated with each components
E_θ	Electric field for θ component
E_ϕ	Electric field for ϕ component
H_θ	Magnetic field for θ component
H_ϕ	Magnetic field for ϕ component
$\mathbf{J_x}, \mathbf{J_y}, \mathbf{J_z}$	Components of electric current density
$\mathbf{M_x}, \mathbf{M_y}, \mathbf{M_z}$	Components of magnetic current density

List of publications

Journal papers

1. **Rahil Joshi**, Symon K. Podilchak, Dimitris E. Anagnostou, Constantin Constantinides, Muhammad Nazrin Ramli, Herwansyah Lago, Ping Jack Soh, "Analysis and Design of Dual-Band Folded Shorted Patch Antennas for Robust Wearable Applications,"*IEEE Open Journal of Antennas and Propagation*, vol. 1, pp. 239-252, 2020.

2. **Rahil Joshi**, Ezzaty Faridah Nor Mohd Hussin, Ping Jack Soh, Mohd Faizal Jamlos, Herwansyah Lago, Azremi Abdullah Al-Hadi, Symon K. Podilchak, "Dual-Band, Dual-Sense Textile Antenna with AMC Backing for Localization using GPS and WBAN/WLAN," *IEEE Access*, vol. 8, pp. 89468-89478, 2020.

3. Qassim S. Abdullahi, **Rahil Joshi**, Symon K. Podilchak, Sadeque R. Khan, Meixuan Chen, Jean Rooney, John Rooney, Danmei Sun, Marc P. Y. Desmulliez, Apostolos Georgiadis, Dimitris Anagnostou, "Design of Wireless Power Transfer System for Assisted Living Applications," *Wireless Power Transfer*, vol. 6, no. 1, pp 41-56, 2019.

4. Danmei Sun, Meixuan Chen, Symon K. Podilchak, Apostolos Georgiadis Qassim S. Abdullahi, **Rahil Joshi**, Sohail Yasin, Jean Rooney, John Rooney, "Investigating flexible textile-based coils for wireless charging wearable electronics," *Journal of Industrial Textiles*, Feb. 2019.

5. A. G. Koutinos, D. E. Anagnostou, **R. Joshi**, S. K. Podilchak, G. A. Kyriacou, M. T. Chryssomallis, "Modified easy to fabricate E-shaped compact patch antenna with wideband and multiband functionality," *IET Microwaves, Antennas & Propagation*, vol. 12, no. 3, pp. 326-331, Feb. 2018.

Journal papers to be submitted

1. **Rahil Joshi**, Symon K. Podilchak, Bob Low and Ping Jack Soh, "Design and Analysis of Flexible Textile Based Transmission Lines," *IEEE Microwave Theory and Techniques*.

Conferences

1. Bashar Bahaa Qas Elias, Ping Jack Soh, Azremi abdulla Al-Hadi, **Rahil Joshi**, Yuepei Li, and Symon K. Podilchak, "Design of a Quad Band CPW-fed Compact Flexible Patch Antenna for Wearable Applications," *2020 14th European Conference on Antennas and Propagation (EuCAP)*, Copenhagen, Denmark, 2020, pp. 1-5.

2. Qassim S. Abdullahi, **Rahil Joshi**, Symon K. Podilchak, Meixuan Chen, Jean Rooney, John Rooney, Danmei Sun, Apostolos Georgiadis, Dimitris Anagnostou, "A Wireless Power Charger System using a 2-D Near-Field Array for Assisted Living Applications," *2019 13th European Conference on Antennas and Propagation (EuCAP)*, Krakow, Poland, 2019, pp. 1-5.

3. **Rahil Joshi**, Symon K. Podilchak, Constantin Constantinides, Ping Jack Soh, "Dual-Band Folded-Shorted Patch Antenna for Military Search and Rescue Operations and Emergency Communications," *2018 18th International Symposium on Antenna Technology and Applied Electromagnetics (ANTEM)*, Waterloo, ON, 2018, pp. 1-2.

4. **Rahil Joshi**, Constantin Constantinides, Symon K. Podilchak, Muhammad Nazrin Ramli, Herwansyah Lago, Ping Jack Soh, "Robust and compact PDMS antennas for search and rescue operations and emergency communications," *12th European Conference on Antennas and Propagation (EuCAP 2018)*, London, 2018, pp. 1-5.

Chapter 1

Introduction

1.1 Wearable Antenna: Review

As the name suggests, wearable antennas are specifically designed to be worn by a user. Research on wearable antennas has been intensive in recent years due to their ability to integrate within clothing and function as a wireless device. Wearable antennas are commonly used in sectors such as healthcare, defense, sports, fitness, telecommunications and transportation. The wearable antenna needs to be flexible and lightweight so that it is comfortable for the user and should also be compact, and robust to changing environments, such as temperature, humidity, and water resistance.

There is a wide range of wearable antennas that have been developed for various applications. In [1], a low cost and smart wearable textile antenna array system was designed and analyzed for biomedical telemetry applications. This system was designed to be worn by medical personnel, who examine patients, or by the patients themselves, to transmit telemetry signals. In [2], an intelligent health monitoring system was developed that used an implantable antenna. A wearable antenna for soldiers that was fabricated from a textile material was presented in [3]. A dual-polarized textile antenna for rescue workers was developed and presented in [4]. It also gave rise to the development of antennas for protective garments, such as those used by firefighters. In [5], two dual-polarized textile patch antennas are introduced which are located on the front and backside of a firefighter′s suit. Wearable antennas are also developed in different shapes and sizes. These include a finger ring shaped
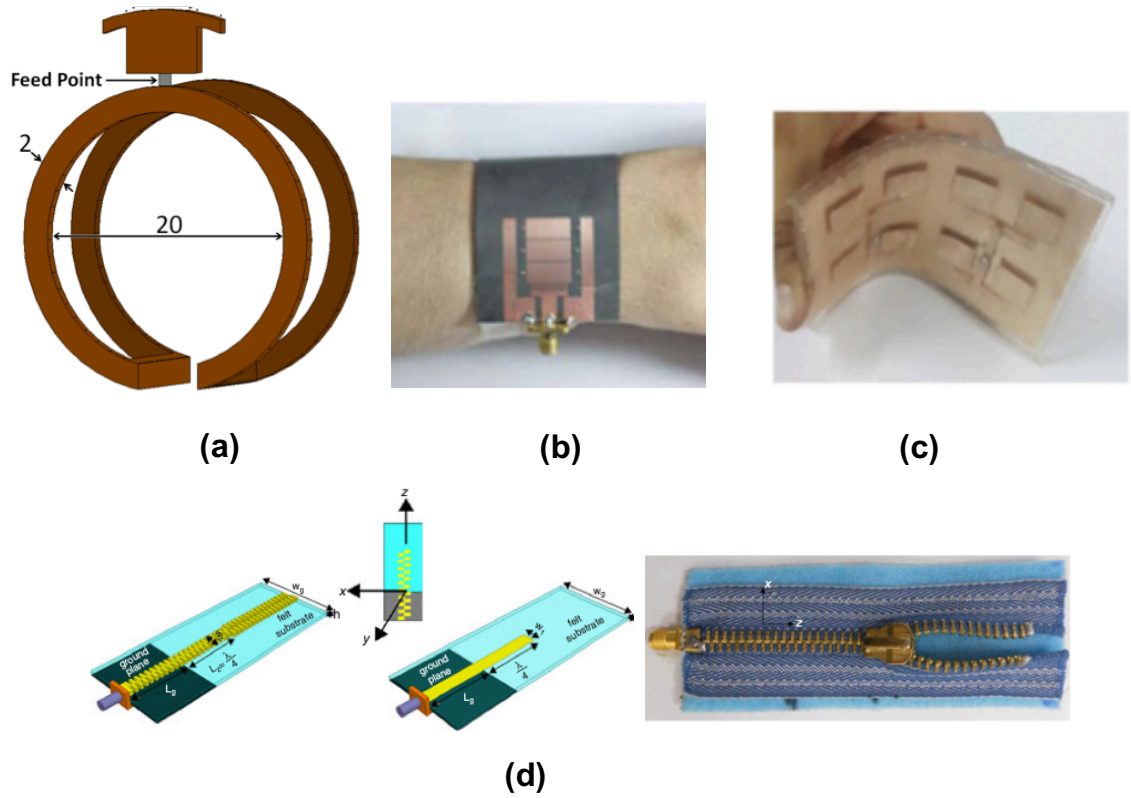
Figure 1.1: Wearable antenna designs available in different shapes and sizes: (a) Finger-ring like structure [6], (b) wrist wearable antenna [7], (c) flexible MIMO antenna array [11] and (d) zip-shaped flexible monople antenna [10].

UWB antenna [6], a wrist wearable antenna for WBAN applications [7], a dual-band button-shaped antenna [8], and logo shaped wearable antennas [9]. A novel zip-shaped monopole antenna operating at 2.5 GHz was presented in [10]. Figure 1.1 illustrates various designs of wearable antennas available in literature.

Not all wearable antennas developed are flexible; there have also been rigid wearable antennas. Most rigid wearable antennas developed are UWB antennas. For example, in [12], a UWB button-shaped antenna was designed. The metallic button, considered to be a top-loaded monopole, acts as a radiating element. It was placed on top of velcro, the other side of which was shielded by copper that acts as the ground plane of the antenna. The antenna produces an unobstructive feature which is suitable for wearable antennas. A novel planar inverted F antenna (PIFA) for wearable applications was introduced in [13]. This antenna was designed on a rigid ground plane and tested for on-body performance. The antenna maintained good radiation performance even when placed on the body. Similarly, in [14], a spiral PIFA antenna was developed using a rigid FR4 substrate. This antenna was

developed for implantable devices. Rigid wearable antennas can only be successfully implemented on a specific location of the body, such as the upper arm, but to be more practical, wearable antennas need to be flexible.

To summarize, wearable antennas need to be flexible, lightweight and compact so they are comfortable for the user while the antenna is being worn. For example, consider a user who is walking up to 10 to 16 hours a day in harsh weather conditions and is carrying heavy equipment. If they were wearing a cumbersome antenna then, as a result, they may experience fatigue. Most importantly, wearable antennas need to be robust and durable for any environment, for example the device should not rust, be able to withstand multiple cycles of washing and drying, and should be resistant to the different temperature ranges.

1.1.1 Review on Flexible Substrate Materials

Textiles are one of the most preferred choice of material as a substrate for wearable antenna as it provides a degree of freedom in terms of flexibility. They are also lightweight, have a low dielectric constant (1-1.9) and are relatively low cost. For example, in [15], a dual-band textile antenna was presented for GSM and WLAN applications. Fleece was used as a substrate so that antenna can be flexible and lightweight. In [16], a circularly polarized patch antenna was designed where polyamide spacer fabric was used as a substrate. More common textile materials, such as jeans and felt, were also used to develop wearable antennas. Wearable textile antennas using jeans as a substrate were presented in [17–19]. Three different wearable antennas were fabricated using felt as a substrate in [20]. In [21] five different materials i.e., fleece, upholstery fabric, vellux, felt and Condura were tested as a textile antenna subtrate, each analyzed for its effectiveness in GPS applications.

Polymer-based materials are also used as a substrate for wearable antennas, they have a low water absorption rate and are more resistant toward temperature compared to textile materials. In [22], a tapered slot UWB wearable antenna using liquid crystal polymer (LCP) was designed and fabricated. LCP has a low water absorption factor and is flexible, low cost, and has low moisture permeability. Another polymer-based substrate material that has gained traction in recent years is polydimethylsiloxane (PDMS). It is a silicone-based polymer that is flexible, low

cost, hydrophobic, and has low moisture permeability. In [23], a dual-band textile antenna on the PDMS substrate for body-centric communication was presented. In [24], an RFID passive tag antenna was designed to investigate the washing durability of the PDMS embedded conductive material. It was concluded that PDMS embedded conductive material has physical robustness characteristics that help it to survive harsh environments.

Another topic that has seen tremendous growth in recent years is metasurfaces. Depending on the design metasurfaces may be integrated within the substrate of antennas. In wearable antennas, metasurfaces are used to enhance the bandwidth of the antenna and to reduce backward radiation towards the human body. In [25], the performance of the dual-band coplanar patch antenna integrated with electromagnetic bandgap (EBG) substrate was described, designed and fabricated. EBG acts as a high impedance surface (HIS) which also enhances the gain of the antenna. An overview of EBG integrated with wearable antennas was presented in [26]. Another commonly used metasurface is an artificial magnetic conductor (AMC) surface. A wearable reconfigurable antenna integrated with AMC is proposed in [27]. By integrating AMC in the design, the SAR level was reduced. Similarly, a low profile textile monopole antenna integrated with a compact AMC substrate was reported in [28]. Both EBG and AMC are based on the principles of an ideal perfect magnetic conductor (PMC).

In summary, textile and polymer-based materials are most commonly used as substrate material for wearable antennas. Table 1.1 summarizes the main characteristics of fleece, felt, LCP, and PDMS, all of which have been used to develop wearable antennas. Before the design of wearable antennas, key characteristics such as flexibility, durability, and robustness of the substrate is an essential factor that needs to be considered. Textile material has a low dielectric constant and is flexible but has a high water absorption factor. In comparison, polymer material has hydrophobic characteristics, which makes it more suitable as a substrate for the wearable antenna.

Table 1.1: Summary of the Characteristics of the Textile and Polymer Based Materials

Material	ϵ_r	$\tan \delta$	Flexible	Hydrophobic
Fleece [29]	1.04	-	✓	✗
Felt [29]	1.30	0.02	✓	✗
LCP [30]	2.9-3.2	0.002-0.004	✓	✓
PDMS [29, 31]	2.7-2.8	0.001-0.002	✓	✓

1.2 Background of the Problem and Motivation

1.2.1 Wearable Antenna

As discussed in section 1.1, the research into wearable technology has grown rapidly over the years. Antennas are developed with different shapes, designs and sizes. Planar antennas are the most common form of wearable antenna due to their compact size and low cost. Single frequency band antennas are easier to design compared to dual-band antennas. In literature, dual-band antennas have complex designs that are difficult to fabricate. To design a simple dual-band wearable antenna is a challenging task. Once the antenna is designed and fabricated, the characterization of the antenna measurement plays a key role. However, there are several measurement challenges in regards to wearable antennas. For example, on-body performance measurements such as evaluating the effect of bending and placement of the antenna on a human phantom, which is challenging due the antenna being probe fed and the irregular shape of the phantom body.

Transverse magnetic (TM) modes play a crucial role in understanding the operation of an antenna, and can help in the optimization process. The majority of antennas operate at the TM_{010} mode (unless specified) which is broadside, compared to the higher order TM modes. For example, in the literature, most wearable antennas exploit the higher order TM_{020} or TM_{030} [32], [33] modes. These can generate multiple maxima which would require slots in the antenna design to force a stable and consistent beam pattern at broadside. The introduction of slots increases bandwidth and reduces the size of the antenna, however they also make the design more complex. Therefore, in this thesis, simple and compact wearable antenna designs are presented which provide excellent performance, are cost-effective, and are an
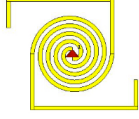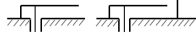
advancement on the current state of the art technology. Through this thesis, a complete antenna system for wearable applications i.e., the antenna and the connecting flexible transmission line, is proposed. The transverse magnetic (TM) operating modes in the antennas are also studied, analyzed and reported.

1.2.1.1   Proposed Solution

A dual-band antenna for military search and rescue operations is proposed in this thesis. Antennas for such an application require operation in the UHF and ISM frequency bands for satellite and WiFi connectivity. As well as requiring a large frequency spacing and compact size, these antennas must offer reasonable comfort when worn and also must be manufactured using materials that can guarantee robustness and maintained antenna performance. The antennas exposure to bending and washing can lead to a shift in operating frequency. Harsh environmental conditions can also reduce the efficiency of the antenna. Moreover, the need for operation in the UHF band conventionally requires large and protruding UHF dipoles (based on the nearly 1-meter wavelength), which limits movement/mobility for operators. These issues can be solved by the proposed compact and wearable folded shorted patch (FSP) antenna. Table 1.2 summarizes the advantages of the FSP antenna over other low-cost planar antennas that are suitable for such applications. The important features of the proposed antenna are based on a novel FSP operating by the TM_{010} [32] and TM_{001} [32] modes, whereas its robustness is improved by a flexible polymer-based material. Broadside radiation, equations to calculate the radiated far-fields and directivity for the operating modes have been newly derived and compared with full-wave simulations, indicating agreement. Results from these analysis are also compared with prototype measurements and full-wave simulations, and results are also in agreement. Such analysis for an FSP for these particular operating modes has yet to be reported in the literature and is novel solution.

Further, a dual-band patch antenna is also proposed for GPS and WiFi applications. Antennas for GPS application need to have circular polarization for their operation. In the literature, many reported wearable antennas are dual-polarized. However, these antennas often are large and have a more complex design that is difficult to manufacture. These issues can be solved by the proposed dual-band patch antenna

Table 1.2: A review on compact planar antennas

Antenna Types			
Patch Antenna [34, 35]	Spiral Antenna [36]	Dipole Antenna [32]	Folded Patch Antenna [37]
Advantages			
Low Cost	Broadband	Simple Design	Compact
Easy Fabrication	Broadside Radiation	Omnidirectional	Low Cost
Light Weight	Circular		Linear/Circular
Linear/Circular			
Disadvantages			
Narrow Bandwidth	Complex Desgin	Large size	Narrow Bandwidth

using the AMC substrate. The use of AMC also helps to reduce the backward radiation towards the user.

1.2.2   Wearable Transmission Line: Review

For any antenna system, a feed line is one of the main components, as it connects an antenna to the main power source. Some common types of transmission lines that can be used for wearable applications are coaxial lines, microstrip, waveguide, or stripline. The literature is limited on wearable transmission line. But it should be mentioned that there are few prototypes that have been developed and investigated. For example, the design and fabrication of the flexible transmission line was reported in [38,39]. Textile-based flexible striplines were presented in [40,41]. These prototypes were useful for applications in healtcare sector, GPS, and ISM frequency bands. Figure 1.2 shows various designs on fabricated flexible transmission lines which are available in literature.

In order to connect a wearable antenna and transmission line, a connector is also a crucial component. In [42], various connectors for wearable devices have been reported such as snap-on buttons, butterfly clasps, wing solutions, and conductive epoxy. In [43], a velcro was used to establish an RF connection between the patch
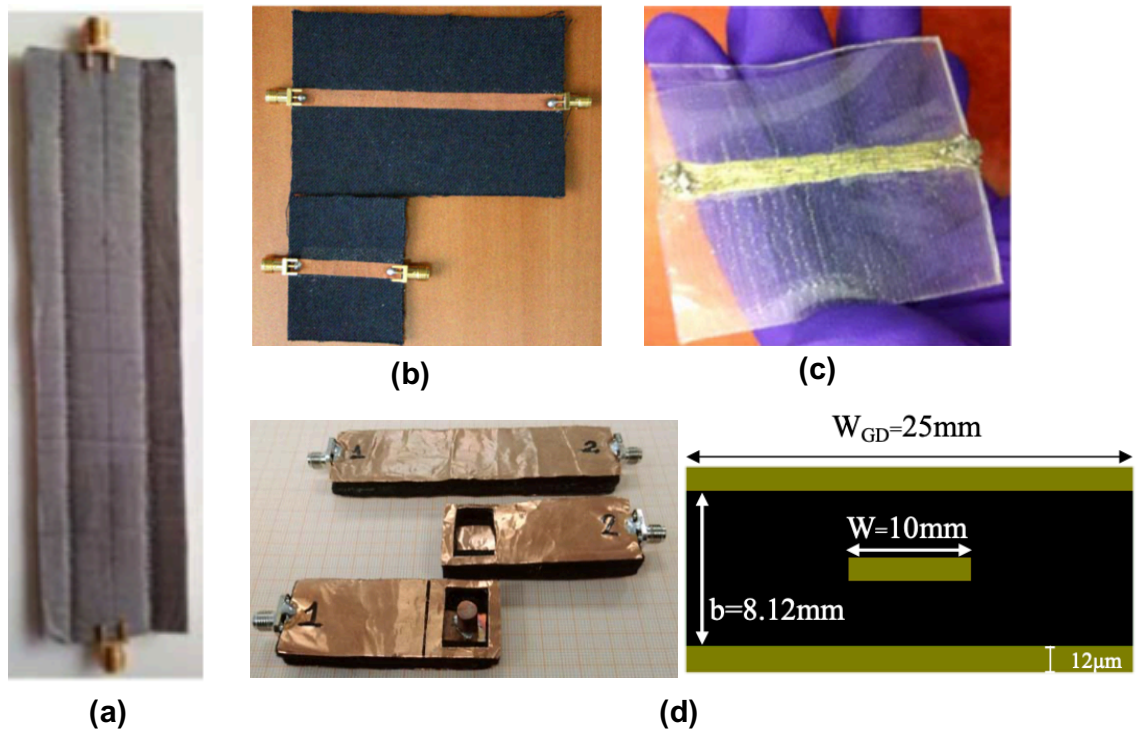
Figure 1.2: Flexible transmission line designs available in different shapes and sizes:(a) wearable textile stripline [40], (b) textile micrpstrip transmission line [38], (c) PDMS based transmission line [39], and (d) textile stripline [40].

antenna and the stripline.

Most antenna prototypes are fed either by a coaxial probe or by a microstrip transmission line. Similar to wearable antennas, the transmission line needs to be flexible, lightweight and robust to the harsh environment. Most of the transmission line available in the literature are larger in size which needs further optimization in order to use for wearable applications. Therefore, this thesis presents flexible textile-based coaxial transmission lines prototypes. These novel transmission lines are designed, simulated and fabricated for wearable applications, and are made from two different hybrid textile materials. To the best of the authors′ knowledge, no such transmission line design is available in the literature.

1.3   Document Overview

This thesis is composed of 5 chapters including this introductory chapter.

• Chapter 2 introduces two flexible transmission line prototypes which are designed, simulated and fabricated using two different hybrid textile materials. Robustness

tests such as bending and twisting, and wet tests will also be demonstrated to measure the durability of fabricated transmission line prototypes. An investigation on shielding effectiveness and DC analysis of proposed cable will also be discussed.

- Chapter 3 proposes a single-layer circularly polarized (CP) patch antenna where durability and resiliency studies were completed for the adopted polydimethylsiloxane (PDMS) substrate in terms of bending, wet, and temperature testing.

- Chapter 4 presents a dual-band dual sense circular polarized (CP) patch antenna using textile materials. This antenna uses the approach to integrate AMC within the design to minimize the effect of backward radiation on the human body. Bending tests results are discussed to show the resilency of the antenna.

- Chapter 5 a newly developed cavity model analysis approach presented, for the FSPs, which easily allows estimating the operational frequency, pattern shape, polarization, and directivity before any simulation and fabrication activity for the TM_{010} and TM_{001} modes.

- Chapter 6 proposes a novel dual-band wearable antennas. Based on the preliminary results presented in Chapter 3, the folded-shorted patch (FSP) antenna was designed and fabricated using the PDMS substrate. An analysis was also performed to characterize the relevant dimensions that are important for independently controlling or tuning the resonant frequencies for these two radiating modes.

- Chapter 7 summarizes the work presented in this thesis including possible future work.

References

[1] P. J. Soh, B. Van den Bergh, H. Xu, H. Aliakbarian, S. Farsi, P. Samal, G. A. E. Vandenbosch, D. M. M. . Schreurs, and B. K. J. C. Nauwelaers, "A smart wearable textile array system for biomedical telemetry applications," *IEEE Transactions on Microwave Theory and Techniques*, vol. 61, no. 5, pp. 2253–2261, 2013.

[2] Y. Li, W. Duan, L. Yang, and X. Zhao, "Study on the electromagnetic field distribution of an implantable antenna for an intelligent health monitoring system," *IEEE Access*, vol. 7, pp. 28 749–28 756, 2019.

[3] P. Salonen and M. Keskilammi, "Softwear antenna," in *MILCOM 2008 - 2008 IEEE Military Communications Conference*, 2008, pp. 1–6.

[4] L. Vallozzi, H. Rogier, and C. Hertleer, "A textile patch antenna with dual polarization for rescue workers' garments," in *2009 3rd European Conference on Antennas and Propagation*, 2009, pp. 1018–1021.

[5] L. Vallozzi, P. Van Torre, C. Hertleer, H. Rogier, M. Moeneclaey, and J. Verhaevert, "Wireless communication for firefighters using dual-polarized textile antennas integrated in their garment," *IEEE Transactions on Antennas and Propagation*, vol. 58, no. 4, pp. 1357–1368, 2010.

[6] H. Goto and H. Iwasaki, "A finger-ring UWB monopole antenna for BAN and PAN," in *2010 IEEE Antennas and Propagation Society International Symposium*, 2010, pp. 1–4.

[7] J. Lee, S. I. Kwak, and S. Lim, "Wrist-wearable zeroth-order resonant antenna for wireless body area network applications," *Electronics Letters*, vol. 47, no. 7, pp. 431–433, 2011.

[8] B. Sanz-Izquierdo, J. A. Miller, J. C. Batchelor, and M. I. Sobhy, "Dual-band wearable metallic button antennas and transmission in body area networks," *IET Microwaves, Antennas Propagation*, vol. 4, no. 2, pp. 182–190, Feb 2010.

[9] G. Monti, L. Corchia, E. D. Benedetto, and L. Tarricone, "Wearable logo-antenna for GPS GSM-based tracking systems," *IET Microwaves, Antennas Propagation*, vol. 10, no. 12, pp. 1332–1338, 2016.

[10] M. Mantash, A. C. Tarot, S. Collardey, and K. Mahdjoubi, "Wearable monopole zip antenna," *Electronics Letters*, vol. 47, no. 23, pp. 1266–1267, 2011.

[11] A. S. M. Alqadami, M. F. Jamlos, P. J. Soh, and G. A. E. Vandenbosch, "Assessment of PDMS technology in a MIMO antenna array," *IEEE Antennas and Wireless Propagation Letters*, vol. 15, pp. 1939–1942, 2016.

[12] B. Sanz-Izquierdo, J. C. Batchelor, and M. Sobhy, "UWB wearable button antenna," in *2006 First European Conference on Antennas and Propagation*, 2006, pp. 1–4.

[13] P. Salonen, L. Sydanheimo, M. Keskilammi, and M. Kivikoski, "A small planar inverted-F antenna for wearable applications," in *Digest of Papers. Third International Symposium on Wearable Computers*, 1999, pp. 95–100.

[14] A. Harish, M. R. Hidayat, L. O. Nur, B. S. Nugroho, and A. Munir, "Spiral-shaped printed planar inverted-F antenna for body wearable application," in *2017 11th International Conference on Telecommunication Systems Services and Applications (TSSA)*, 2017, pp. 1–4.

[15] P. Salonen, Y. Rahmat-Samii, H. Hurme, and M. Kivikoski, "Dual-band wearable textile antenna," in *IEEE Antennas and Propagation Society Symposium, 2004.*, vol. 1, 2004, pp. 463–466 Vol.1.

[16] M. Klemm, I. Locher, and G. Troster, "A novel circularly polarized textile antenna for wearable applications," in *34th European Microwave Conference, 2004.*, vol. 1, 2004, pp. 137–140.

[17] M. A. R. Osman, M. K. A. Rahim, M. Azfar. A., K. Kamardin, F. Zubir, and N. A. Samsuri, "Design and analysis UWB wearable textile antenna," in *Proceedings of the 5th European Conference on Antennas and Propagation (EU-CAP)*, 2011, pp. 530–533.

[18] C. K. Nanda, S. Ballav, A. Chatterjee, and S. K. Parui, "A body wearable antenna based on jeans substrate with wide-band response," in *2018 5th International Conference on Signal Processing and Integrated Networks (SPIN)*, 2018, pp. 474–477.

[19] E. N. F. S. E. Embong, K. N. A. Rani, and H. A. Rahim, "The wearable textile-based microstrip patch antenna preliminary design and development," in *2017 IEEE 3rd International Conference on Engineering Technologies and Social Sciences (ICETSS)*, 2017, pp. 1–5.

[20] B. Hu, G. Gao, L. He, X. Cong, and J. Zhao, "Bending and on-arm effects on a wearable antenna for 2.45 GHz body area network," *IEEE Antennas and Wireless Propagation Letters*, vol. 15, pp. 378–381, 2016.

[21] P. Salonen, Y. Rahmat-Samii, M. Schaffrath, and M. Kivikoski, "Effect of textile materials on wearable antenna performance: a case study of GPS antennas," in *IEEE Antennas and Propagation Society Symposium, 2004.*, vol. 1, 2004, pp. 459–462 Vol.1.

[22] M. Ur-Rehman, Q. H. Abbasi, M. Akram, and C. Parini, "Design of band-notched ultra wideband antenna for indoor and wearable wireless communications," *IET Microwaves, Antennas Propagation*, vol. 9, no. 3, pp. 243–251, 2015.

[23] R. B. V. B. Simorangkir, Y. Yang, L. Matekovits, and K. P. Esselle, "Dual-band dual-mode textile antenna on PDMS substrate for body-centric communications," *IEEE Antennas and Wireless Propagation Letters*, vol. 16, pp. 677–680, 2017.

[24] R. B. V. B. Simorangkir, D. Le, T. Bjrninen, A. S. M. Sayem, M. Zhadobov, and R. Sauleau, "Washing durability of PDMS-conductive fabric composite: Realizing washable UHF RFID tags," *IEEE Antennas and Wireless Propagation Letters*, vol. 18, no. 12, pp. 2572–2576, 2019.

[25] S. Zhu and R. Langley, "Dual-band wearable textile antenna on an EBG substrate," *IEEE Transactions on Antennas and Propagation*, vol. 57, no. 4, pp. 926–935, 2009.

[26] A. Y. I. Ashyap, S. H. B. Dahlan, Z. Zainal Abidin, M. I. Abbasi, M. R. Kamarudin, H. A. Majid, M. H. Dahri, M. H. Jamaluddin, and A. Alomainy, "An overview of electromagnetic band-gap integrated wearable antennas," *IEEE Access*, vol. 8, pp. 7641–7658, 2020.

[27] S. M. Saeed, C. A. Balanis, C. R. Birtcher, A. C. Durgun, and H. N. Shaman, "Wearable flexible reconfigurable antenna integrated with artificial magnetic conductor," *IEEE Antennas and Wireless Propagation Letters*, vol. 16, pp. 2396–2399, 2017.

[28] A. Alemaryeen and S. Noghanian, "On-body low-profile textile antenna with artificial magnetic conductor," *IEEE Transactions on Antennas and Propagation*, vol. 67, no. 6, pp. 3649–3656, 2019.

[29] R. Salvado, C. Loss, R. Gonçalves, and P. Pinho, "Textile materials for the design of wearable antennas: A survey," *Sensors*, vol. 12, no. 11, pp. 15 841–15 857, 2012.

[30] D. C. Thompson, O. Tantot, H. Jallageas, G. E. Ponchak, M. M. Tentzeris, and J. Papapolymerou, "Characterization of liquid crystal polymer (LCP) material and transmission lines on LCP substrates from 30 to 110 GHz," *IEEE Transactions on Microwave Theory and Techniques*, vol. 52, no. 4, pp. 1343–1352, 2004.

[31] J. Trajkovikj, J. Zrcher, and A. K. Skrivervik, "PDMS, a robust casing for flexible W-BAN antennas [EurAAP corner]," *IEEE Antennas and Propagation Magazine*, vol. 55, no. 5, pp. 287–297, 2013.

[32] C. A. Balanis, *Antenna theory: analysis and design.* John wiley & sons, 2016.

[33] J. Anguera, A. Andjar, and J. Jayasinghe, "High-directivity microstrip patch antennas based on TModd-0 modes," *IEEE Antennas and Wireless Propagation Letters*, vol. 19, no. 1, pp. 39–43, 2020.

[34] Y. Lo, D. Solomon, and W. Richards, "Theory and experiment on microstrip antennas," *IEEE Transactions on Antennas and Propagation*, vol. 27, no. 2, pp. 137–145, 1979.

[35] R. Garg, P. Bhartia, I. J. Bahl, and A. Ittipiboon, *Microstrip antenna design handbook.* Artech house, 2001.

[36] M. Richardson, C. J. Bauder, R. Kazemi, and A. E. Fathy, "Design of a rigid UWB log spiral antenna for GPR applications in harsh environment," in *2020 IEEE Radio and Wireless Symposium (RWS)*, 2020, pp. 262–264.

[37] J. L. Volakis, C.-C. Chen, and K. Fujimoto, *Small antennas: miniaturization techniques & applications.* McGraw-Hill, 2010.

[38] F. Declercq and H. Rogier, "Characterization of electromagnetic properties of textile materials for the use in wearable antennas," in *2009 IEEE Antennas and Propagation Society International Symposium*, June 2009, pp. 1–4.

[39] Z. Wang, L. Zhang, Y. Bayram, and J. L. Volakis, "Embroidered conductive fibers on polymer composite for conformal antennas," *IEEE Transactions on Antennas and Propagation*, vol. 60, no. 9, pp. 4141–4147, Sep. 2012.

[40] Z. Xu, T. Kaufmann, and C. Fumeaux, "Wearable textile shielded stripline for broadband operation," *IEEE Microwave and Wireless Components Letters*, vol. 24, no. 8, pp. 566–568, Aug 2014.

[41] A. Tsolis, A. A. Alexandridis, W. G. Whittow, and J. C. Vardaxoglou, "Investigation of textile striplines connectivity for feeding and connecting wearable antennas," in *2015 9th European Conference on Antennas and Propagation (EuCAP)*, April 2015, pp. 1–5.

[42] S. P. Pinapati, T. Kaufmann, I. Linke, D. Ranasinghe, and C. Fumeaux, "Connection strategies for wearable microwave transmission lines and antennas," in *2015 International Symposium on Antennas and Propagation (ISAP)*, Nov 2015, pp. 1–4.

[43] A. Tsolis, A. A. Alexandridis, F. Lazarakis, A. Michalopoulou, W. G. Whittow, and J. C. Vardaxoglou, "All-textile connector for a wearable patch antenna," in *The Loughborough Antennas Propagation Conference (LAPC 2018)*, Nov 2018, pp. 1–6.

Chapter 2

Textile Based Transmission Lines

In this chapter, two low-cost, light weight and flexible novel textile-based transmission line using two different textile materials are designed, simulated and fabricated. Both feed lines follow the coaxial transmission line configuration. These transmission lines are designed for wearable applications and are suitable for operation in the L, S and C band frequencies. These types of transmission lines can be an alternative to the use of rigid or semi-rigid coaxial cables. The chapter is organised as follows. Section 2.1, provides an introduction about transmission lines and its applications. In Section 2.2 and 2.3, the concept and general configuration of coaxial cables is described. In Section 2.4, electrical characterization of textile materials, design, simulation and assembly of fabicated textile transmission lines are discussed. Measurement of reflection coefficient, transmission coefficient, robustness test (bending and wet test), DC analysis and electromagnetic compatibility (EMC) test are discussed in Section 2.5 while summary of the chapter are made in Section 2.6.

2.1   Introduction

One of the important components in radio frequency (RF) circuit is the transmission line that can be designed to operate at various frequency ranges. In general, a transmission line is used to transfer a signal defined by a transverse electromagnetic (TEM) waves [1]. The basics about transmission line design and related theory are mentioned in [2, 3]. In the past decade, the invention of smart and intelligent materials and structures has led to the development of products in the field of

defense, transportation, medical, sports and telecommunications. This trend has led to the development of the integrated wireless communication systems and textile based antennas, and the whole system can be categorized as a wearable textile system as mentioned in [4]. Previous chapters have demonstrated different designs of flexible wearable antennas for on-body communications to external transceivers. However, the design of any RF circuit will not be optimum without considering the connecting transmission lines [5]. The transmission line is used in an antenna to function properly as an antenna feeding network or antenna interface circuit. The transmission lines are required to connect and realize the feeding circuit when considering wearable antennas [6,7].

2.2 Concept of Textile Coaxial Cables

The majority of previously published works on wearable antennas lacks discussion about the feeding network of the antenna. For example, for RF applications a transmission line is required at both the receiver and transmitter side because it acts as a feedline. In reality, to connect any wearable antennas when operating at RF and microwave frequencies, a flexible transmission line is essential. There is also a limited literature available on flexible transmission lines, and only a few authors have investigated the performance of flexible transmission lines.

In the past decade, research on the smart fibre and fabrics has led to the development of e-textile or intelligent textiles that can sense and detect environmental changes depending on the application. For example, the Jacquard [8] is the product developed by Google that enables the access to digital life for the user by using or wearing their garments. Recently, Levis (a fashion cloth merchandiser) has manufactured a range of jackets that are embedded with the Jacquard technology. The general information about smart fabrics, fibres and clothing are outlined in [9]. E-textiles are developed for the body-centric applications, henceforth it should be flexible, low cost and lightweight. Based on the properties some early prototypes of e-textiles were developed such as textile touch sensors [10] to control smart devices, radio frequency identification (RFIDs) for the sports application [11] and body-worn e-textile antenna for wireless and GPS communications [12,13]. There are common methods by which smart materials can be incorporated into the textile structure are
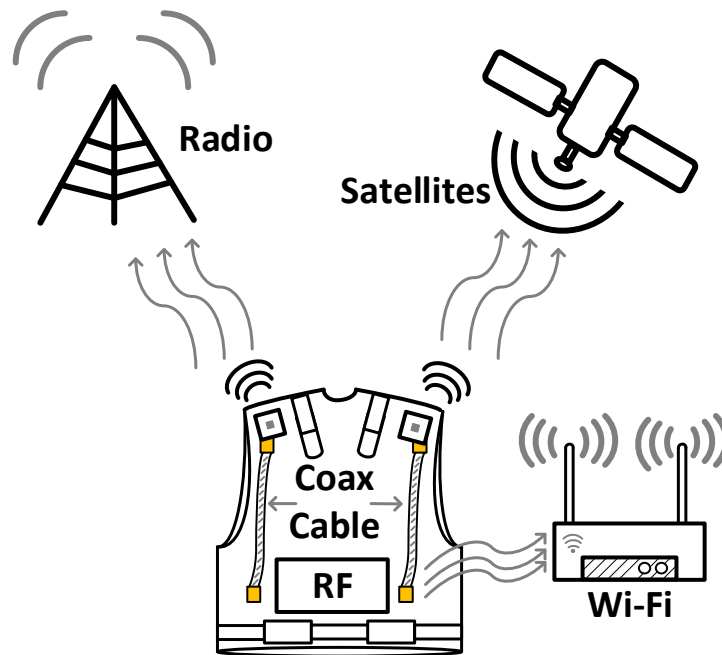
Figure 2.1: Illustration of a flexible coaxial cable connected to wearable antenna that is placed on the ballistics jacket and its application for various frequency ranges. For example, if a coaxial cable is connected to an antenna then that can be used for satellite communications, radio communications and other wireless applications such as GPS and Wi-Fi.

by embroidering, sewing, knitting, weaving, braiding and printing. There are also various fabrication techniques that can be used for flexbile transmission line such as conductive fibres, conductive fabrics and conductive inks.

These earlier developments and studies on e-textile laid the foundation for textile based products and the possibility for the RF components to be manufactured by using textile materials. For example, in [14], the electrical characterization of the conductive textile materials has been presented for the flexible transmission lines. The approximate value of fineness and weight per unit area of the textile threads are mentioned keeping in mind wearable attributes. Additionally, fibre or fabric needs to be conducting and should be suitable for data transmission. There are some methods mentioned in the literature to create conductive threads such as filling fibre with metal or carbon, coating of fibre with conductive polymers or metal, and use of continuous of short fibres that are entirely made of conductive material [15]. This combination of metal fibres with synthetic fibres leads to the formation of processed yarns that can be woven or knitted.

In this chapter, a wearable flexible transmission line is designed, simulated, fabri-

cated, and intvestigated for broadband operation with a measured frequency range from DC to 6 GHz. The proposed transmission line is designed for applications related to military search and rescue operation, emergency services, Wi-Fi communication, navigations, and any RF hardware that can be worn. The idea is to embed textile based transmission line along with wearable antennas inside a bulletproof jacket as shown in Fig. 2.1. Other specific applications are signal transmission in underground tunnels, Wi-Fi signals for long distance flights, and connections for wearable health monitoring systems. The textile transmission lines should be lightweight and thin so that it is comfortable while being worn. Flexibility and robustness are some of the necessary characteristics. Since the design is developed to be worn by a user, a textile material is preferred over any other materials for fabrication of these transmission lines.

2.3   General Configuration

Fundamental structures in electronic circuits are the transmission lines. The types of transmission line that is introduced in this chapter is the coaxial or coax transmission line. To the best knowledge of the author, no similar textile-based transmission line has been reported previously which adopts the classic coaxial cable configuration. The coaxial cable which is made from textile material also follows the same physical structure as any standard commercially available coaxial cables. The general structure of the standard coaxial cable is illustrated in Fig.2.2. A standard coaxial cable is constructed using four layers. Layer 1 is the inner conductor which is also be known as the centre conductor or inner core. This inner core is surrounded by the layer 2 which is a dielectric insulator, layer 3 is a metallic mesh often called an outer conductor or an outer core, and layer 4 is the outer wrapping or outer jacket enabling shielding (see Fig. 2.2) [2, 16].

The inner conductor of the coaxial cable is metallic as it carries the signal, whereas the outer conductor is a braided mesh made from the metal that helps to shield the cable from the electromagnetic interference (EMI). The dielectric between an inner and outer conductor is a low-loss material that acts as an insulator [17]. Fig. 2.3 shows the cross-section of a standard coaxial transmission line [18]. The radius of an inner conductor (layer 1) is r_i, the radius of the inner layer of an outer conductor
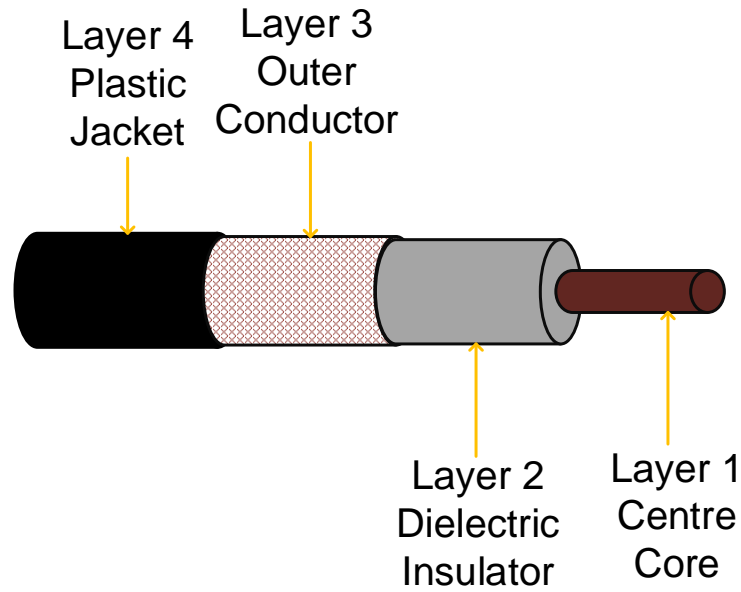
Figure 2.2: Layout showing the general configuration of the standard coaxial cable commercially available. Different layers are labeled classifying each segment of the standard coaxial cable.

(layer 3) is r_o and the dielectric constant of the dielectric insulator (layer 2) is ϵ_r.

The characteristic impedance (Z_o) is an important parameter that needs to be carefully examined and analyzed before designing the textile cable, as it determines the matching within the system. In literature, Z_o is purely a function of inductance and capacitance disturbed along the transmission line length and can be calculated using (2.3.1) [2]:

$$Z_o = \frac{138}{\sqrt{\epsilon_r}} \times \log\left(\frac{r_o}{r_i}\right)$$

or

$$Z_o = \frac{138}{\sqrt{\epsilon_r}} \times \log\left(\frac{D_o}{D_i}\right)$$

(2.3.1)

Where,

$$D_o = \text{Diameter of the inner layer of outer conductor,}$$

$$D_i = \text{Diameter of the inner conductor}$$
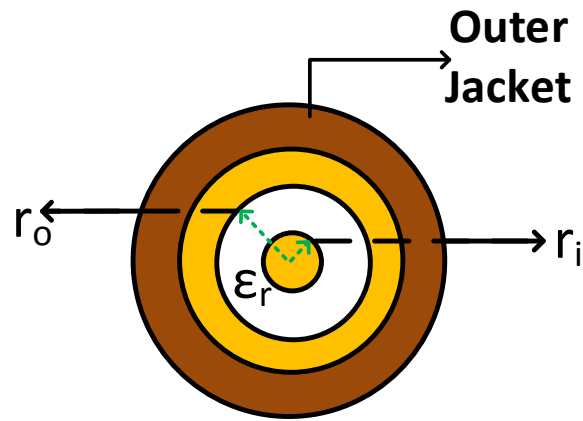
Figure 2.3: Cross sectional view of the coaxial cable showing inner conductor radius r_i, outer conductor radius r_o and relative dielectric permittivity of the dielectric insulator (ϵ_r).

The impedance of the coaxial cable cable highly depends on r_o, r_i and ϵ_r. Coaxial cables are typically designed either at 50 Ω or 75 Ω, and it should be precisely matched to the source and load impedance. Any significant mismatch can give rise to reflected power back toward the source, data loss, and signal corruption. The characteristic impedance of cables, in general, is not related to the length of the cable.

Attenuation denoted as α is another major performance parameter for coax cables. As the signal moves through the feeder there can be loss of power that can arise from several factors and is present on all cables [19]. For example, attenuation of the cable depends on the length of the coaxial cable. The coax loss or attenuation is specified in terms of a loss, normally in decibels over a given length. Also, the attenuation of the cable is dependent on the three main parameters: resistive loss, dielectric loss and radiated loss [20]. The attenuation is also increased due to the braid contamination, moisture entry, degradation of the braid, and from the cable
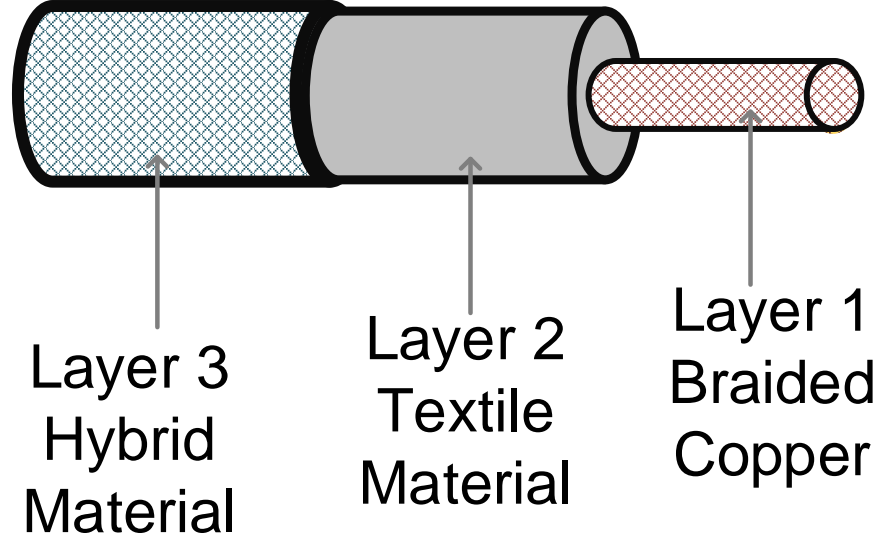
Figure 2.4: The layout of proposed textile based coaxial cable illustrating the different textile layers.

flexing. Cable attenuation can be calculated using (2.3.2) [2, 19].

$$\alpha = \alpha_d + \alpha_c$$

$$\alpha_d = \frac{ktan\delta}{2}$$

$$\alpha_c = \left(\frac{R_D}{D_o} + \frac{R_d}{D_i}\right)\frac{1}{2\eta ln\frac{D_o}{D_i}} \qquad (2.3.2)$$

$$\eta = \sqrt{\frac{\mu}{\epsilon}}$$

$$R = 10.88 \times 10^{-3} \times \sqrt{\frac{10^7}{\sigma}\frac{1}{\lambda_g}}$$

In (2.3.2), α_d is the attenuation due to dielectric loss of the cable, and α_c is the attenuation due to conductor loss of the cable. η is the intrinsic impedance of the medium, λ_g is the guided wavelength, σ is the conductivity of material, R_D and R_d are the resistive losses for the metallic mediums; i.e. for an outer and inner conductor, respectively. From these parameters, the theoretical attenuation can be calculated for the coaxial cables. The choice of textile material when considering implementation is another essential factor to be assessed for the designers. The tex-

tile material that is used for wearable applications has properties such as flexibility, stretching and recovery after deformation, and due to these properties, the material should be fine and lightweight. We know that for the data transmission, separate conductor lines are required and fine metal threads suits this purpose best as they can provide a reasonable electrical conductivity[1]. This combination of fabric mixed together with metal threads leads to the formation of a hybrid material. In [21], a hybrid material called PETEX has been reported which is the combination of fabric and copper wire, and it has a DC resistance of 17.2 Ω/m. In [14], six prototypes were developed and presented that were made from the polyester yarn twisted together with copper and have DC resistance from 7.31 Ω/m to 17.05 Ω/m depending on the prototypes. These results prove that the metal increases the conductivity of the hybrid material depending on the density of the metal and hence can offer high mobility of electric current with decent overall electrical performance.

2.4   Design of the Textile Coaxial Cables

The coaxial cable made from the textile material follows the same topology as the standard coaxial cable and is shown in Fig. 2.4. The textile coaxial cable presented has three layers. Layer 1 is the inner layer that is purely a metallic braid, followed by layer 2 which is a dielectric insulator enclosed around the inner conductor and is a flexible pure textile material, and layer 3 is a mesh of hybrid material. Layer 4 which is an outer shield in the standard coaxial cable is not used in this simple textile coaxial cable prototypes.

The textile materials used for the cables should have high elasticity[2] and should be easily bendable so that it is comfortable while being worn [14]. In this work, initially, polyester (PES) material was examined and characterized. Also, polytetrafluoroethylene (PTFE) textile material was also examined. These materials were selected as they are durable, resistant to shrinking, offer fast drying times when

---

[1]Copper (Cu) and Silver (Ag) have high electrical conductivity and most commonly used in electrical components.

[2]High elasticity is defined as the ability of an object or material to resume its normal shaped after being stretched or compressed. For example, textile material needs to have high elasticity so that when bend or twisted it can regain its normal form easily. The deformation should not stay longer or permanently.

compared to other fabrics, are lightweight, and have a low dielectric constant. Copper threads are used to ensure the data transmission, and that the metal can carry the fields. Braiding techniques have been adopted in this work to get a strong and tight physical structure [22]. A 2D braiding technology consists of two pairs of yarns twisted together over each other (specifically one above the other) and also to provide mechanical stability an axial yarns[3] are introduced as mentioned in [22]. It is worth mentioning that in literature most of the work on wearable textile systems (for example, wearable textile antenna) are developed using either weaving [14, 24] or embroidery [25, 26] technique. Moreover, the use of braiding technique was recommended by the project officer of this work Bob Low (J&D Wilkie ltd). Two yarns were made for each material and they are called PES yarn and PTFE yarn.

2.4.1 Electrical Characterization

Once the yarns are manufactured, the next step is to characterize them when considering implementation for textile based transmission lines. Many methods in the literature are mentioned for the material characterization such as free-space methods, transmission-line method, near-field sensors and resonant cavity. The free-space method uses two lens focusing antennas with material to characterized in between two antennas and the two antennas are connected to the vector network analyzer (VNA) [27]. With the help of this configuration reflection coefficient and transmission coefficients to measure the dielectric constant and loss tangent of the material at the microwave frequencies. In the transmission line method the material is employed as filling material for the transmission line and this filling gives the information needed for material properties. Transmission lines such as waveguide [28], stripline [29] and microstrip [30] are used for this method. In the near-field sensor method, open-ended coaxial lines are used and the material to be characterized is placed right at the opening which helps to estimate the reflection coefficient of the material [31]. The resonant cavity method is a more accurate method as compared to the other three methods. In this method, material is placed in the cavity res-

---

[3]These are usually biaxial or triaxial yarns in the configuration. A biaxial yarn construction is two sets of yarns traveling in the opposite direction passing under and over the other yarns. A triaxial yarn consist of the third set of longitudinal yarns in addition to biaxial interlacing yarns [23].

onator and the shift in resonant frequency is measured [32]. These four methods are also further discussed in detail in [33]. Inspired from these methods, in our work, to electrically characterize the textile yarns two approaches were adopted: (1) measurement using an antenna and (2) using a ring resonator. These methods were adopted as they are cost-effective and with the least modeling task requirement as compared to the material characterization methods mentioned earlier.

2.4.1.1 Electrical Characterization Using the Patch Antenna

In this method, initially, the reflection coefficient of an already characterized antenna is measured and then the antenna is wrapped with the textile material until a shift in the resonant frequency is noticed. Using traditional microstrip patch antenna design equations [34] (2.4.1), one can calculate the effective relative permittivity
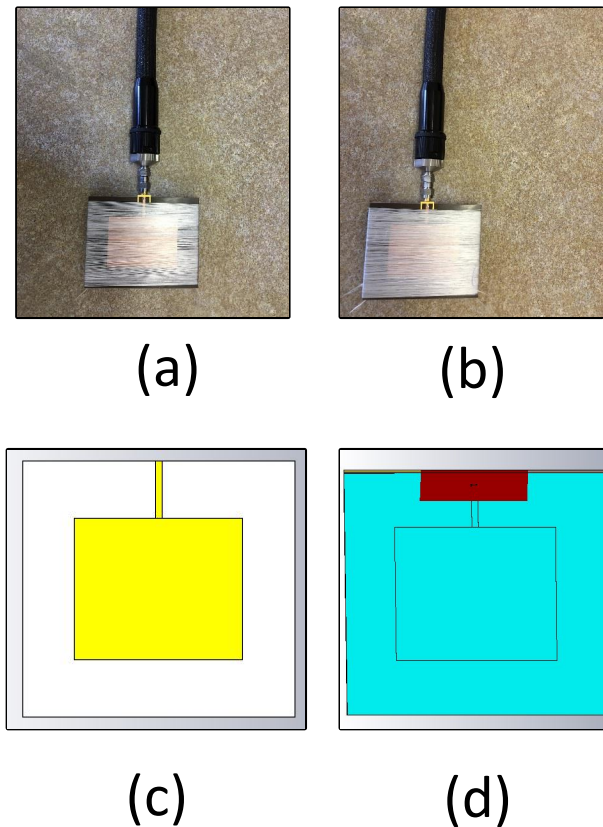
Figure 2.5: Electrical characterization of the textile yarns using patch antennas: (a) Single layer of yarn wrapped around patch antenna, (b) double layer of yarn wrapped around patch antenna, (c) simulated model of the patch antenna and (d) simulated model showing textile yarn wrapped around patch antenna.
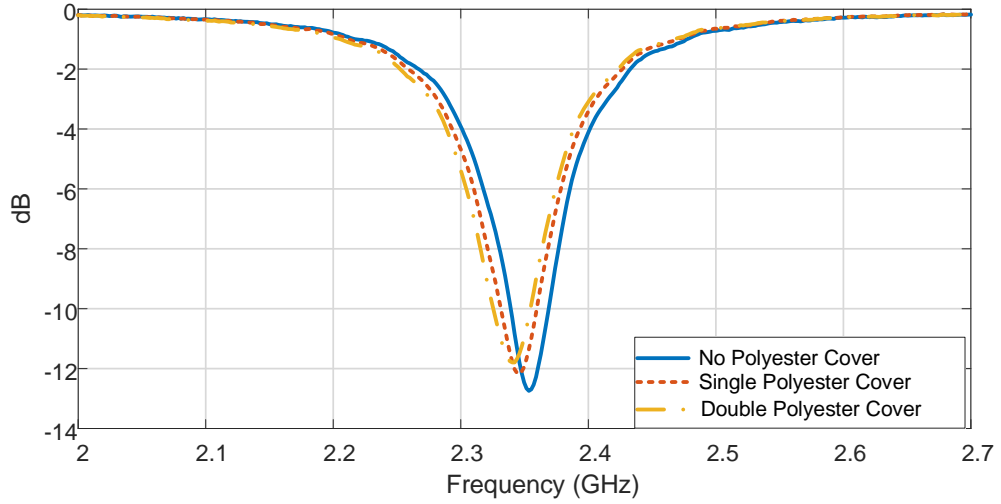
Figure 2.6: Measured reflection coefficient ($|S_{11}|$) for the three cases as described in the legend to extract the material properties of the polyester.

(ϵ_{reff}) of the material, where $c = 3 \times 10^8$ m/s. By using the thickness and width of the substrate of the patch antenna together with ϵ_{reff} the permittivity (ϵ_r) of the textile material can be calculated using (2.4.2) [2, 5, 34]. In addition, these results are verified using the simulations by designing a patch antenna in CST which is wrapped with textile material of interest.

$$\lambda = \frac{c}{f\sqrt{\epsilon_{reff}}} \tag{2.4.1}$$

$$\epsilon_{reff} = \frac{\epsilon_r + 1}{2} + \frac{\epsilon_r - 1}{2}\left(1 + \sqrt{\frac{1}{12\left(\frac{H}{W}\right)}}\right) \tag{2.4.2}$$

Following the procedure described using the patch antenna, the PES yarn was characterized by using a patch antenna operating at 2.35 GHz. Initially, the S_{11} of the patch antenna was measured and recorded. Then, the layer of PES yarn was wrapped around the patch antenna so that the whole antenna was covered (see Fig. 2.5(a)) and the frequency response was recorded. Then another layer of PES yarn was wrapped on top of the already covered antenna (see Fig. 2.5(b)). Figure 2.6 shows the S_{11} for all the three cases and it can be observed that there is a frequency shift. Once the operating frequency of the patch antenna covered with textile material is known, the ϵ_{reff} can be calculated, and then ϵ_r can be determined using (2.4.2) by using MATLAB. For verification, CST [35] simulation was used and the

PES was wrapped around the patch antenna (see Fig. 2.5(c) and (d)). The ϵ_r of the PES yarn from simulations and measurement was found to be 2.0 ± 0.05.

2.4.1.2 Electrical Characterization Using the Ring Resonator

In this method, the characterization of the textile yarn is done by using a ring resonator. The idea here was to measure the frequency response of an already characterized ring resonator and then have a thread of textile material yarn pass through the ring resonator gap (see Fig. 2.8) until a shift in the resonant frequency is noted within the measurements. In this study, a curve fitting method was used to estimate the value of ϵ_r. The PES thread was wrapped around the ring resonator gap and S_{21} was measured. The results from these measurements show that the value of the ϵ_r for the PES material 2.1 ± 0.05 which is close to the value obtain from the first approach.

2.4.1.3 Summary of Electrical Characterization

Both techniques were used to characterize the PES and PTFE yarn. These two techniques are used so that the values derived for the permittivity can be compared to be consistent with the accuracy of the value derived. The comparison of the value of permittivity calculated by using both the techniques is listed in Table 2.1. It can be observed that the values of both PES and PTFE yarns are almost the
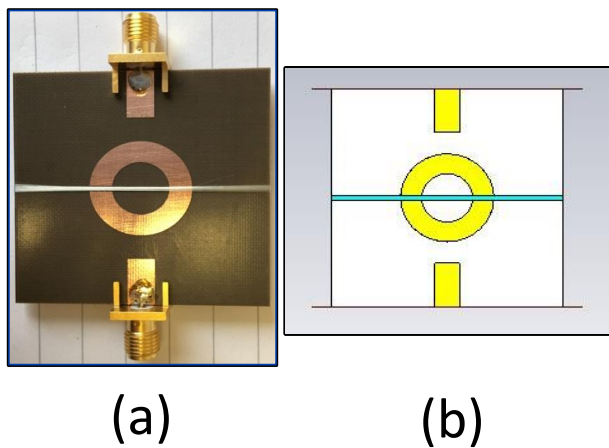
Figure 2.7: (a) Fabricated ring resonator structure showing the polyester thread passing through the gap and (b) equivalent simulation model of the ring resonator.
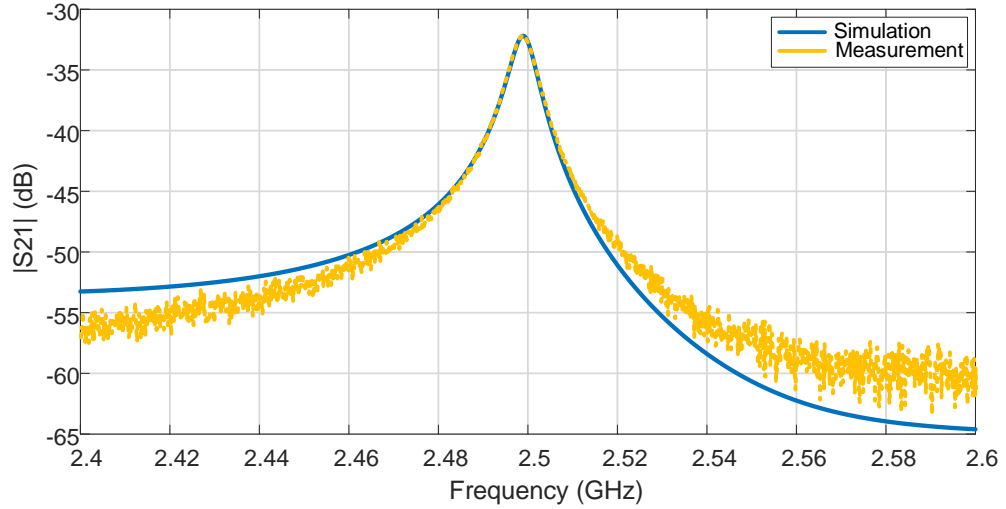
Figure 2.8: Simulated and measured transmission coefficient ($|S_{21}|$) using the ring resonator technique.

Table 2.1: Summary of PES and PTFE yarns permittivity (ϵ_r) value using two electrical characterization approaches

Patch Antenna Approach	
Textile Material	ϵ_r
PES	2.0
PTFE	2.1
Ring Resonator Approach	
PES	2.1
PTFE	2.2

same for both the methods. This step helps to calculate an important parameter for the materials used within the textile cables.

2.4.2 Impedance of the Textile Cable

Using (2.3.1), the impedance of the textile cable can be calculated before the fabrication. In section 2.4, the relative permittivity of the PES yarn was derived. The textile coaxial cable presented in this work is 50 Ω, we can estimate the diameter for the inner conductor and the outer conductor. A parametric study was carried out i.e., the value of D_i and D_o were varied to identify the dimensions, which was needed to achieve the 50 Ω characteristic impedance for the cables. This also helps to decide

the braid thickness of the inner and outer conductors for the textile cables. Table 2.2 lists some of the results from this parametric analysis. From the parametric analysis, the approximate value of D_i and D_o are found out to be 0.95 mm and 3.0 mm, respectively. Given the theory presented above, the relevant parameters such as ϵ_r, Z_o, D_i and D_o can be estimated for the construction for the textile coaxial cable. Now, the next step is to design and simulate the textile cables to verify the design prototypes.

2.4.3   Simulation Model

The textile coaxial cable was designed and simulated with the help of the simulation tool AWR. The schematic of the simulated coaxial model is shown in Fig. 2.9. The dominant mode of propagation in the coaxial line is TEM mode [36] and the implementation of this model is based on the TEM line. The values of D_i and D_o has been calculated in section 2.4.3 (see Table 2.2). A and F are the parameter that depends on the attenuation constant of the cable. K is the dielectric constant that can be used to evaluate the characteristic impedance (Z_o) of the cable.

The S_{11} of the simulated textile coaxial cable is shown in Fig. 2.10(a). The value of D_i, D_o and K from the simulation is found out to be 0.41 mm, 2.01 mm, and 1.977, respectively. The S_{11} is below -10 dB for up to 6 GHz and shows a consistent performance. The insertion phase of the textile cable is shown is in Fig. 2.10(b) for

Table 2.2: Variation in D_i and D_o for impedance (Z) calculation (using Equation 2.3.1)

$\epsilon_r = 2.1$		
D_i [mm]	D_o [mm]	Z [Ω]
0.5	3.0	74.10
0.6	3.0	66.56
0.7	3.0	60.18
0.8	3.0	54.66
0.9	3.0	49.79
0.9	2.5	42.35
0.8	2.5	47.12
0.7	2.5	52.64

Di = Inner Diameter (mm)
Do = Outer Diameter (mm)
L = Length (mm)
K = Dielectric Constant
A = Cable Loss in dB/meter
F = Frequency loss (GHz)

Port
P =1
Z = 50 Ohm

Port
P =2
Z = 50 Ohm
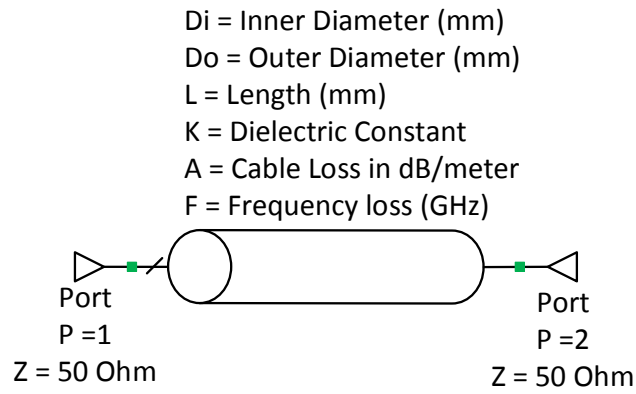
Figure 2.9: Simulated model of the textile coaxial cable
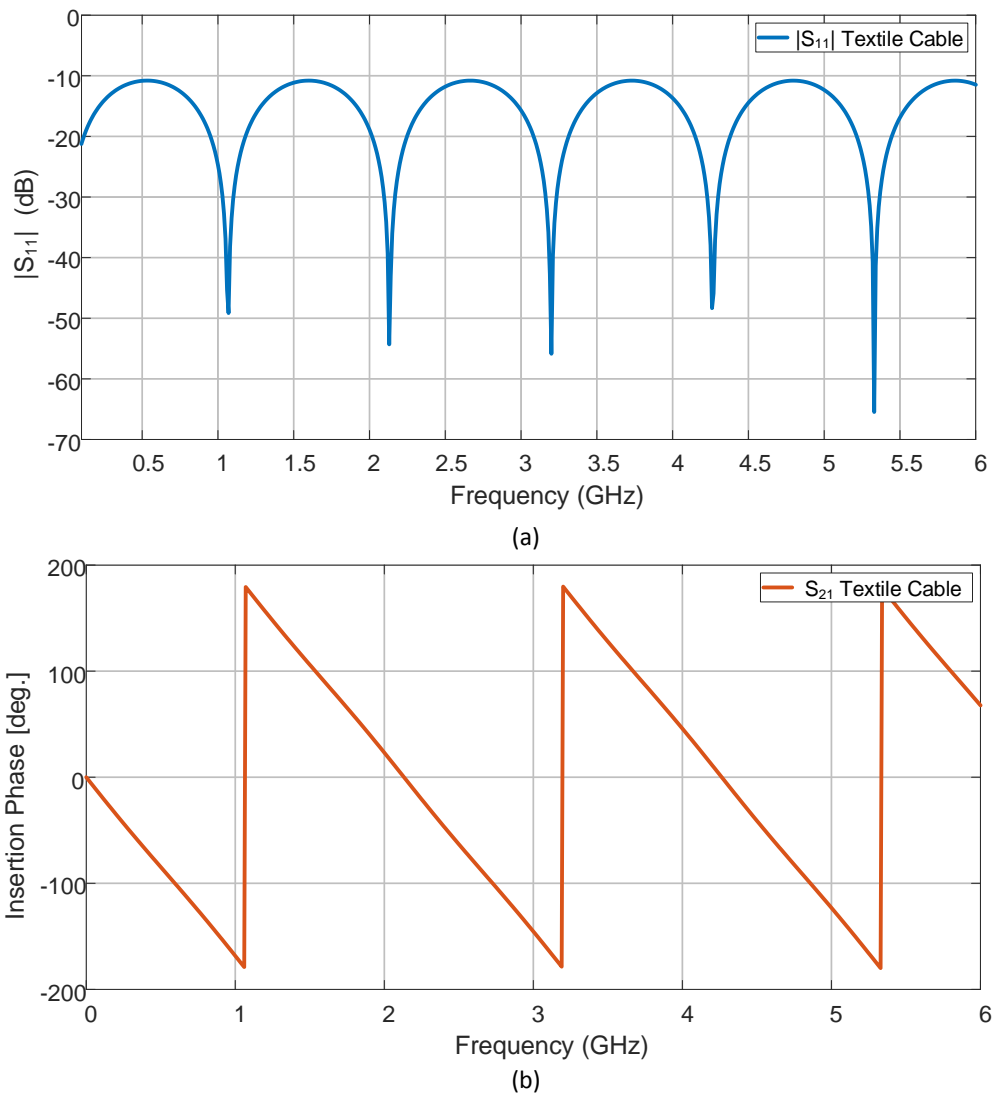
Figure 2.10: (a)Simulated S_{11} of the textile coaxial cable in dB and (b) simulated insertion phase in degrees.

the frequency range up to 6 GHz. These simulated results of the S-parameters were from the initial design gave robust evidence that a textile based coaxial cable can

Table 2.3: Details of Outer Conductor Braiding Pitch in Textile Cable Prototypes

Cable Samples	Pitch [mm]
Polyester Sample 1	12
Polyester Sample 2	15
Polyester Sample 3	30
PTFE Sample 1	12
PTFE Sample 2	12

work.

Although the results in Fig. 2.10 are not satifactory but were the benchmark for the design of the textile coaxial cable. These results gave the evidence that simulation model works well and can be further optimized to obtain better performance. The Z_o of the cable was calculated for different braid fineness for the outer conductor. Three prototypes for the PES cables were simulated that has three different braiding pitch. The details about the braiding pitch of these three polyester prototypes are listed in Table 2.4. The idea behind using three variant of braiding pitches was to investigate the performance of the cables in terms of shielding effectiveness and ohmic losses. In addition, two prototypes of the PTFE cables were manufactured that are of the same braiding pitch as polyester sample 1 prototype (see Table 2.4).

2.4.4 Development of the Textile Coaxial Cables

The development of the textile coaxial cables is divided into three steps. Firstly, the simulated model is designed using the AWR simulation tool for all the cable prototypes. Second, to compare the results from simulations with theoretical equations programmed in MATLAB. Lastly, once the satisfactory results have been obtained the cables were manufactured.

Initially, the D_i and D_o are calculated to match the desired 50 Ω characteristic impedance of the cables. Once these parameters are calculated the attenuation constant of each textile cable prototypes is calculated using (2.3.2). A plot of attenuation constant (α) of all the textile cable prototypes in dB/m across frequency is shown in Fig. 2.11. PTFE sample 2 has the lowest attenuation whereas the polyester samples have sightly higher attenuation.

Now to design a simulated model all the important parameters such as Z_o, D_i, D_o, ϵ_r (ϵ_r is K in Fig. 2.9) and α (α is A in Fig. 2.9) can be calculated and estimated. From the electrical characterization process, the ϵ_r for the PES and PTFE yarns were found out to be 1.97 and 2.1, respectively. Fig 2.12 shows the cross-section of the fabricated textile cable. The inner conductor is made from pure copper, the dielectric layer is made from polyester or PTFE and the outer conductor is a hybrid material i.e. the mix of copper and polyester material. Polyester Prototypes (polyester sample 1, 2 and 3) have dielectric layer as braided polyester and PTFE prototypes (PTFE sample 1 and 2) has a dielectric layer as PTFE material.

The diameter of the inner conductor and outer conductor of the fabricated cables is
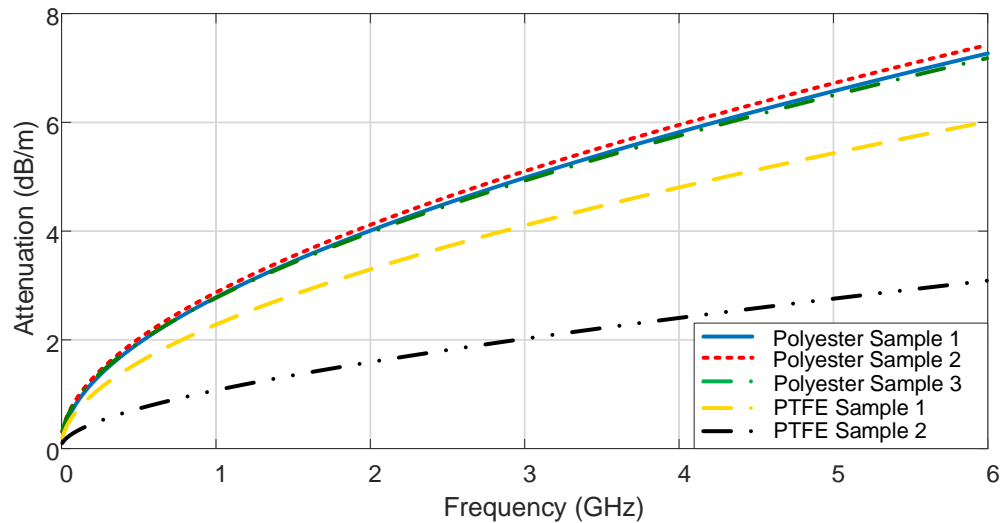
Figure 2.11: Simulated attenuation of all the textile coaxial cable prototypes in dB/m.
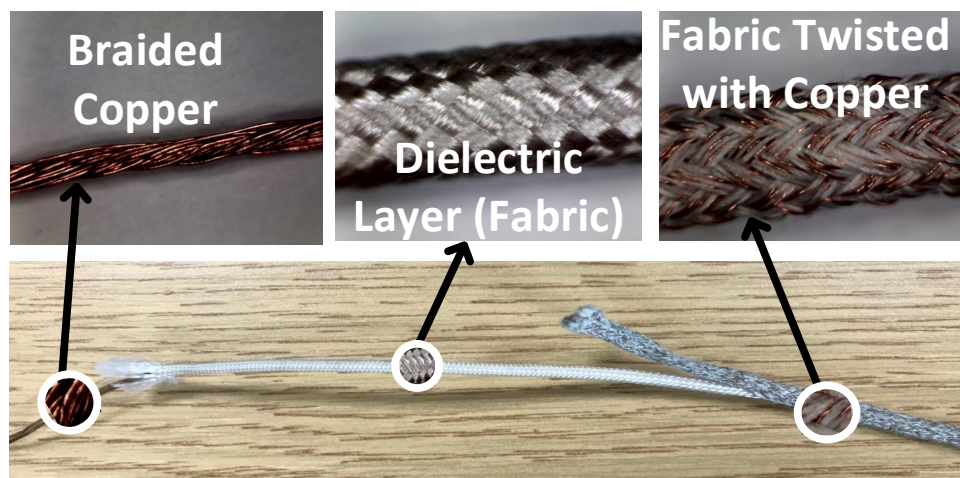
Figure 2.12: The layout of the fabricated textile cable prototype showing each layers.

Table 2.4: Inner Diameter, Outer Diameter and Characteristic Impedance of the Fabricated Textile Cable

Cable Samples	D_i [mm]	D_o [mm]	Z_o [Ω]
Polyester Sample 1	0.50	1.85	52.80
Polyester Sample 2	0.50	2.05	57.60
Polyester Sample 3	0.50	1.99	55.80
PTFE Sample 1	0.60	2.10	53.70
PTFE Sample 2	0.60	2.0	50.80

also measured using high resolution digital microscope. These measured diameter helps to calculate the approximate value of the characteristic impedance of the fabricated cables. The dimension of the inner and outer conductor together with an impedance of the fabricated cables (both prototypes) is listed in Table 2.4. PTFE prototypes have characteristics close to 50 Ω as compared to PES prototypes.
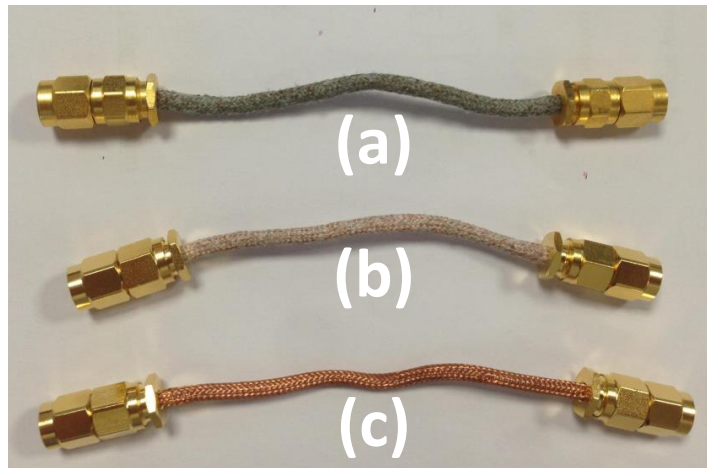
Figure 2.13: Fabricated textile coaxial cables with the connectors (a) Polyester sample (sample 1 with 12 mm braid thickness), (b) PTFE sample 1 and (c) PTFE sample 2.

The two fabricated prototypes of the textile coaxial cables with the connector are shown in Fig. 2.13 (a),(b) and (c). To be specific PES prototypes has inner conductor as braided pure copper threads. The dielectric insulator is made of PES threads and an outer conductor is made of PES twisted together with pure copper. The outer conductor of the PES prototypes in terms of composition has 6% polyester and 94% copper. On the other hand, the PTFE prototypes have an inner conductor as braided pure copper. The dielectric core is made of braided PTFE threads and
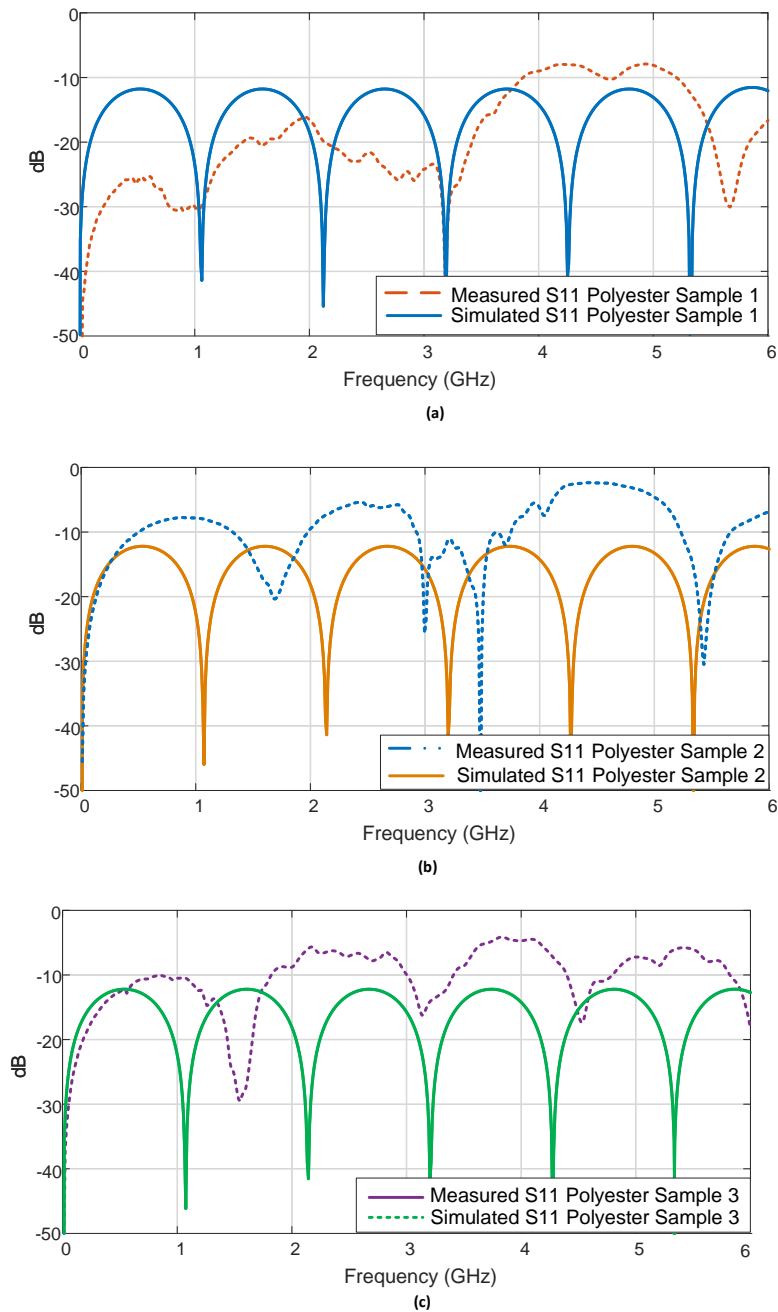
Figure 2.14: Measured and simulated reflection coefficient S_{11} in dB of the prototypes fabricated: (a) polyester sample 1, (b) polyester sample 2, and (c) polyester sample 3.

the outer conductor is braided pure copper for PTFE sample 2. PTFE sample 1 has an outer conductor same as polyester prototypes. Textile material twisted with metal ensures that all parts of the cables are flexible, easily bendable and at the same time maintain good conductivity. It should be mentioned that the cables were manufactured by J&D Wilkie, using a process that was not disclosed. The assembly of connectors were done in Heriot-Watt University.
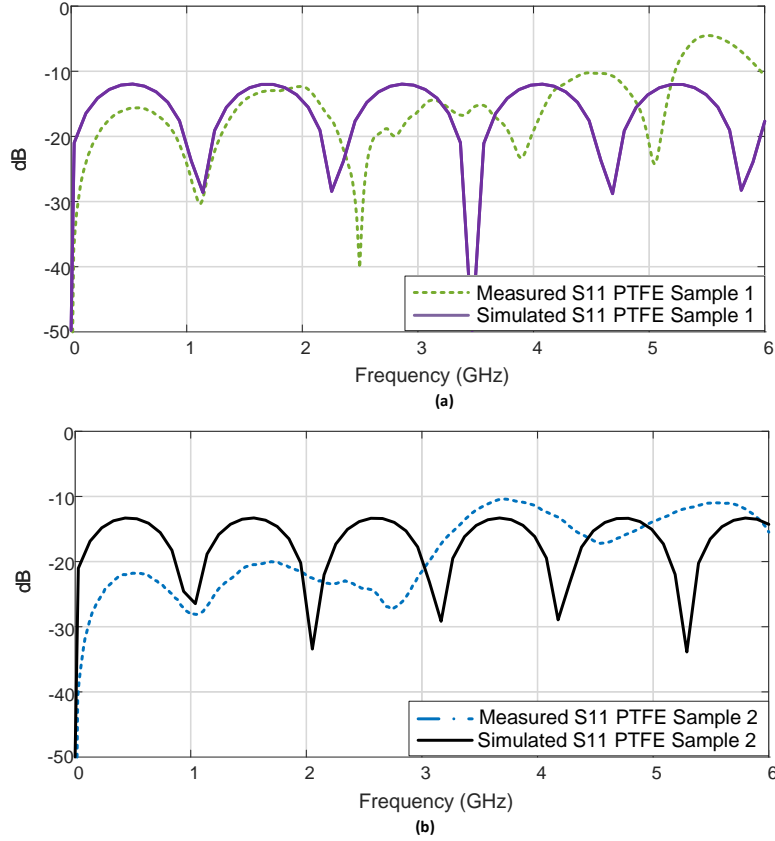
Figure 2.15: Measured and simulated reflection coefficient S_{11} in dB of the prototypes fabricated: (a) PTFE sample 1 and (b) PTFE sample 2.

2.5 Measurement Results

2.5.1 Refelction Coeficient (S_{11}), Insertion Phase and Transmission Coefficient (S_{21})

The S-parameters of all the fabricated cable prototypes were simulated and measured for up to 6 GHz. The comparison of the simulated and measured S_{11} for all the prototypes are shown in Figs. 3.3 and 2.15. Polyester sample 1 has $S_{11} \leq$ -10 dB up to 5 GHz and beyond that the performance of this sample starts declining slightly (see Fig. 3.3(a)). On other hand, polyester sample 2 has poor S_{11} performance (see Fig. 3.3(b)) as compared to polyester sample 3 has much better response (see Fig. 3.3(c)). However, also the performance of the polyester sample 3 starts degrading after 2 GHz. The simulated and measured insertion phase of the fabricated cable prototypes is shown in Figs. 2.16 and 2.17. From Fig. 2.18, it can be observed that the S_{21} of the polyester sample 1 is above -2 dB up to 3.5 GHz whereas sample 2 and 3 has S_{21} above -2 dB only up to 2 GHz. The poor performance of sample 2 and
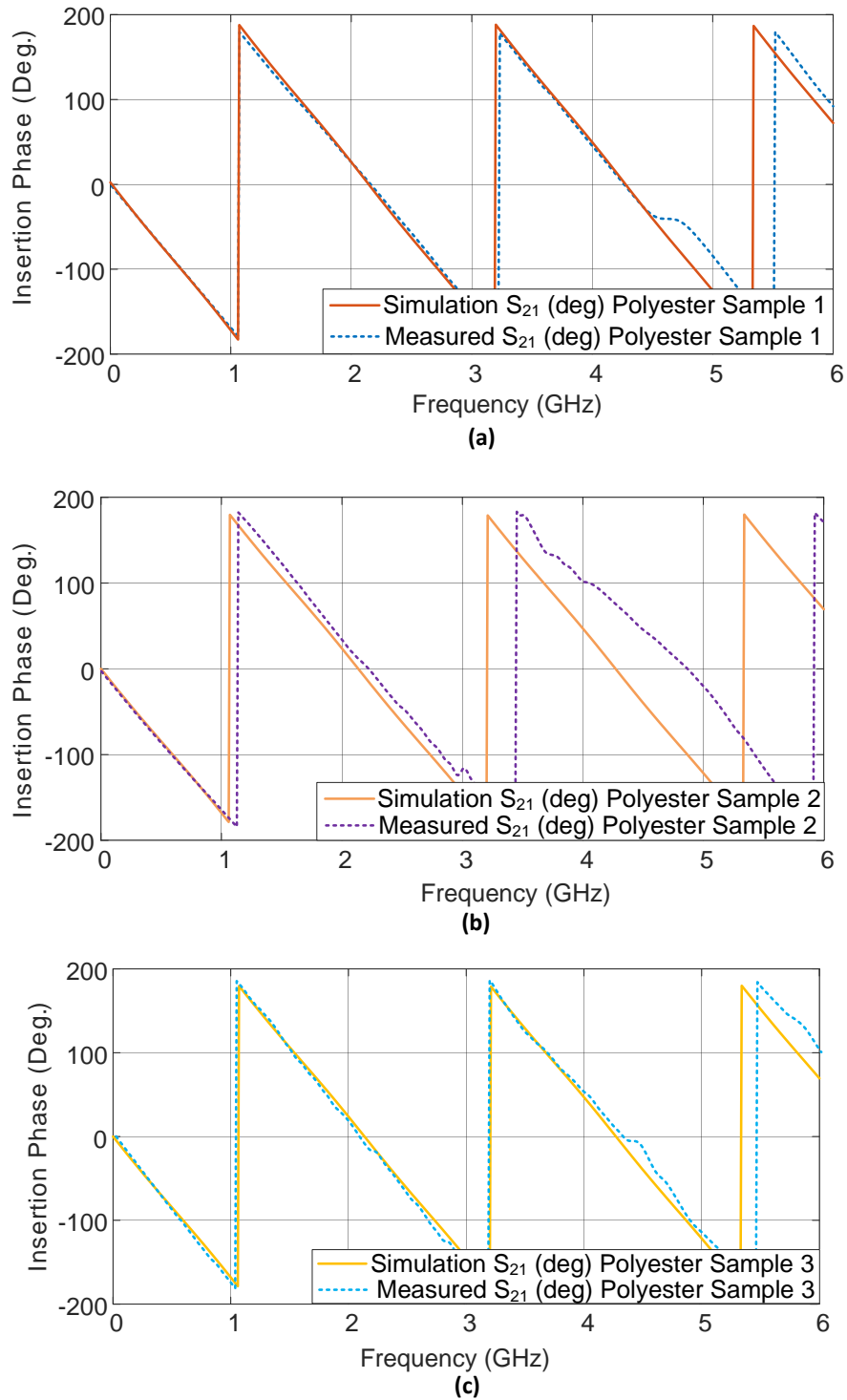
Figure 2.16: Measured and simulated insertion phase in degrees of the prototypes fabricated: (a) polyester sample 1, (b) polyester sample 2 and (c) polyester sample 3

sample 3 is possible due to differences in the braid pitches, fabrication imperfection, and thickness of the outer conductor.

On the contrary, both PTFE prototypes have very good performance as compared to the PES prototypes. The S_{11} of PTFE sample 1 is below -10 dB up to 5.5
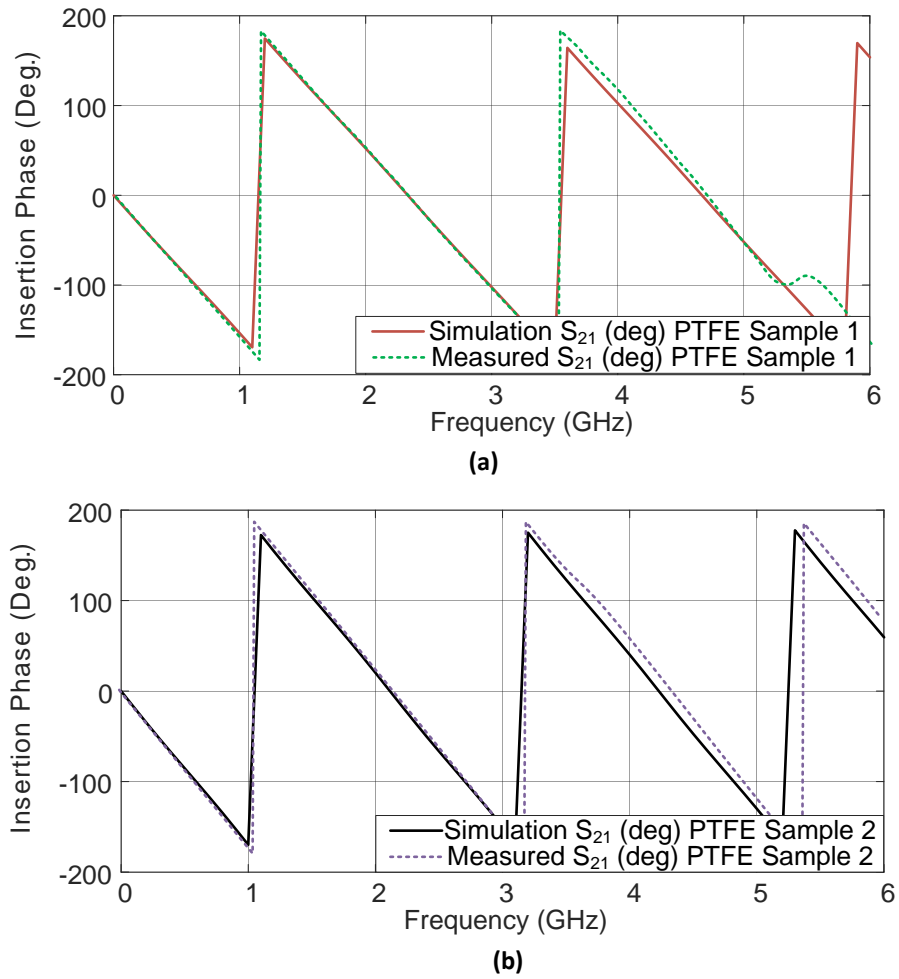
Figure 2.17: Measured and simulated insertion phase in degrees of the prototypes fabricated: (a) PTFE sample 1 and (b) PTFE sample 2.
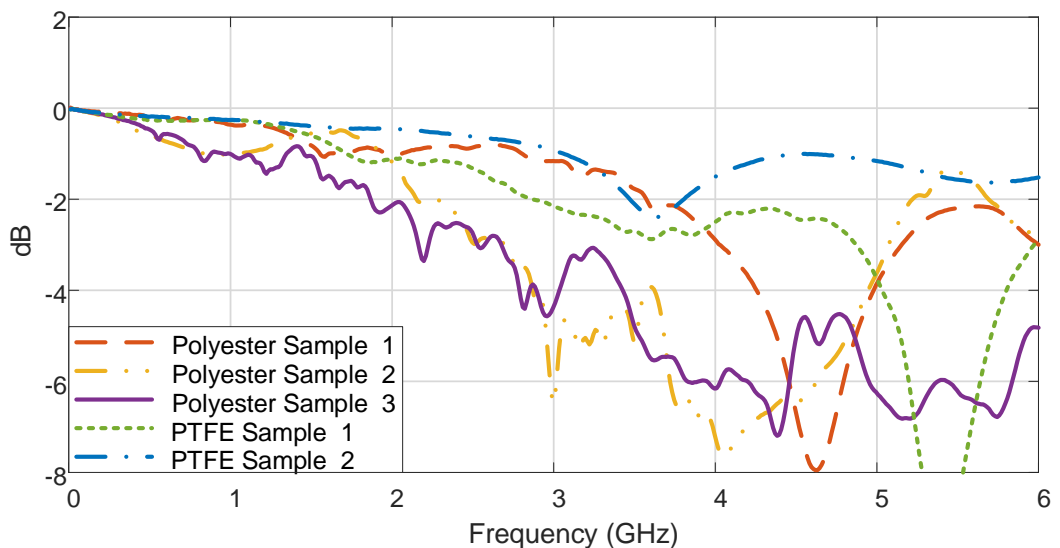
Figure 2.18: Measured transmission coefficient S_{21} of the fabricated prototypes.

GHz and has S_{21} above -2 dB up to 3 GHz (see Figs. 2.15(a) and 2.18). On the other hand, PTFE sample 2 has the S_{11} below -10 dB up to 6 GHz and the S_{21} is

above -2 dB (see Figs. 2.15(b) and 2.18). PTFE sample 2 works very well with the desired performance as compared to other fabricated prototypes. Polyester sample 1 and PTFE sample 1 shows a similar performance and possible due to the same characteristic impedance of both the cables.

2.5.2 Bending Test

The behavior of the textile cable prototypes under the bent condition is one of the important factors for wearable applications and it also demonstrates the physical robustness of the cables. It is difficult to keep the textile cable straight while being placed on-body. To evaluate the performance of the textile cable under bent condition, it has been tested in three different ways. First, the cable was bent 90°, second, it was bent to 180° and lastly, it was bent to its maximum tolerance by forming a loop-like structure. The S_{11} and S_{21} of the coaxial was measured for all the three cases. Fig. 2.19(a), (b) and (c) shows the S_{11} and S_{21} when the cables prototypes are bent at 90°, 180° and loop-like structure, respectively. For the 90° bent, the measured S_{11} for the polyester samples 1 and 3 is below -10 dB up to 3.5 GHz and the measured S_{21} is above -2 dB up to 3.5 GHz. However, on comparison, the polyester sample 2 yields S_{11} below -10 dB up to 1.7 GHz and the S_{21} above -2 dB for up to 1.8 GHz. After approximately 2 GHz, the performance of polyester sample 2 starts declining which is in relevance to the performance measured when the cable (polyester sample 2) was in straight condition. An analogous behavior can be noticed for the 180° bent and loop-like condition for the polyester sample 2 cable. There is not much significant difference can be observed for the polyester sample 1 and 3 for the 180° bent and loop condition. An expected discrepancy can be observed in all polyester samples after 4.5 GHz for both S_{11} and S_{21} is possible due to the resiliency of the operation of the cables in bent conditions. The S_{11} (see Fig. 3.3) shows the performance of the cables when they are in straight form and it can be noticed that the performance of polyester samples starts degrading after 4.5 GHz and same can be noticed for the S_{21}.

On comparison the PTFE sample 1 has $S_{11} \leq$ -10 dB up to 5.5 GHz whereas PTFE sample 2 has $S_{11} \leq$ -10 dB for all the bend cases. For the PTFE sample 1, the measured S_{21} is above -2 dB up to 3 GHz and is between -3 dB to 3.5 dB from

3 GHz to 3.8 GHz, and after 3.8 GHz to 6 GHz it is above -2 dB, for the 90°
bent condition. On the contrast, the PTFE sample 2 cable shows very consistent
performance up to 3.8 GHz with S_{21} above -2 dB and is between -2 dB to 3.5 dB up
to 6 GHz. Similar performance is noticed for both the PTFE prototypes for 180°
bent and loop-like condition.

From the above measurement results, it has been demonstrated that the textile
cables can yield an efficient performance for bending and twisting. Nonetheless, the
PTFE cable prototypes show better results than polyester cable prototypes with
very good insertion loss above -2 dB at DC to 3.5 GHz and in between -2 to -3.5
dB from 3.5 GHz to 6 GHz.
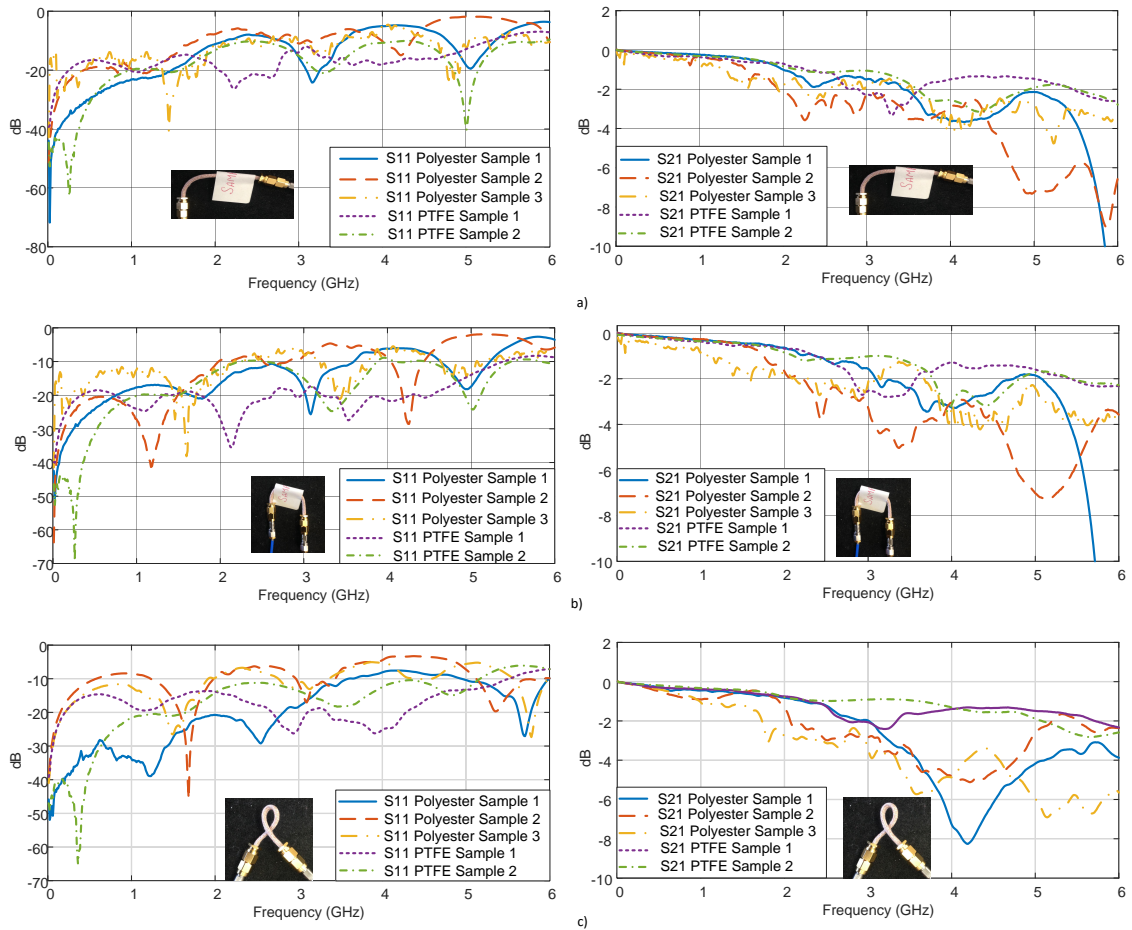
Figure 2.19: Measured S_{11} and S_{21} of all the textile coaxial cable prototypes from the bending
test. All the cables were bent at (a)90°, (b)180° and (c) loop-like structure.
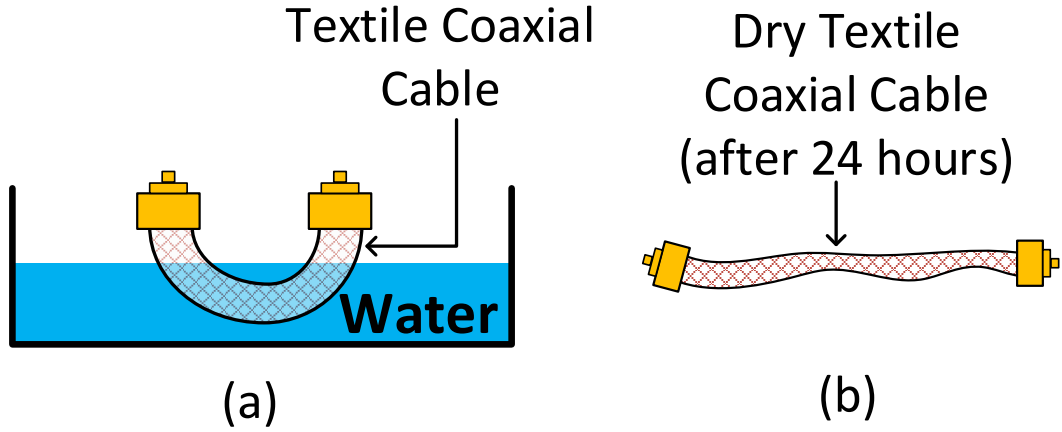
Figure 2.20: Experimental set up of wet test showing 2 cases: (a) When cable is immersed in the water and (b) when cable is dried after 24 hours being wet.

Table 2.5: Summary of the Simulated Textile Cables after Wet Analysis

Dry Condition			Wet Condition		
Frequency [GHz]	ϵ_r	$tan\delta$	Frequency [GHz]	ϵ_r	$tan\delta$
0-2	2.10	0.03	0-2	8.60	0.25
2-3	1.97	0.04	2-3	9.10	0.21
0-5	1.97	0.035	0-5	8.70	0.19

2.5.3 Wet Test

Like a bending test, to check the robustness of the textile cables a wet test has been performed on the textile cables. The wet test has been considered for two conditions: (1) completely wet and (2) 24 hours later (once dried) as shown in Fig. 2.20. These considerations are based on the environment when cables are worn by the user. Cables are already measured for dry conditions and are the situation when the cable is not in contact with water. Completely wet is the condition where cables are in contact with water either partially or completely. Finally, the cables are measured in the condition where they have been in contact with water, for example, rain or human sweat and dried out completely after 24 hours. Figure 2.21(a) and (b) shows the measured S_{21} and S_{11} of the textile coaxial cables for the two conditions, respectively. It can be observed that the performance of the cable is not very efficient when it is wet. But the fabricated cables regains its performance
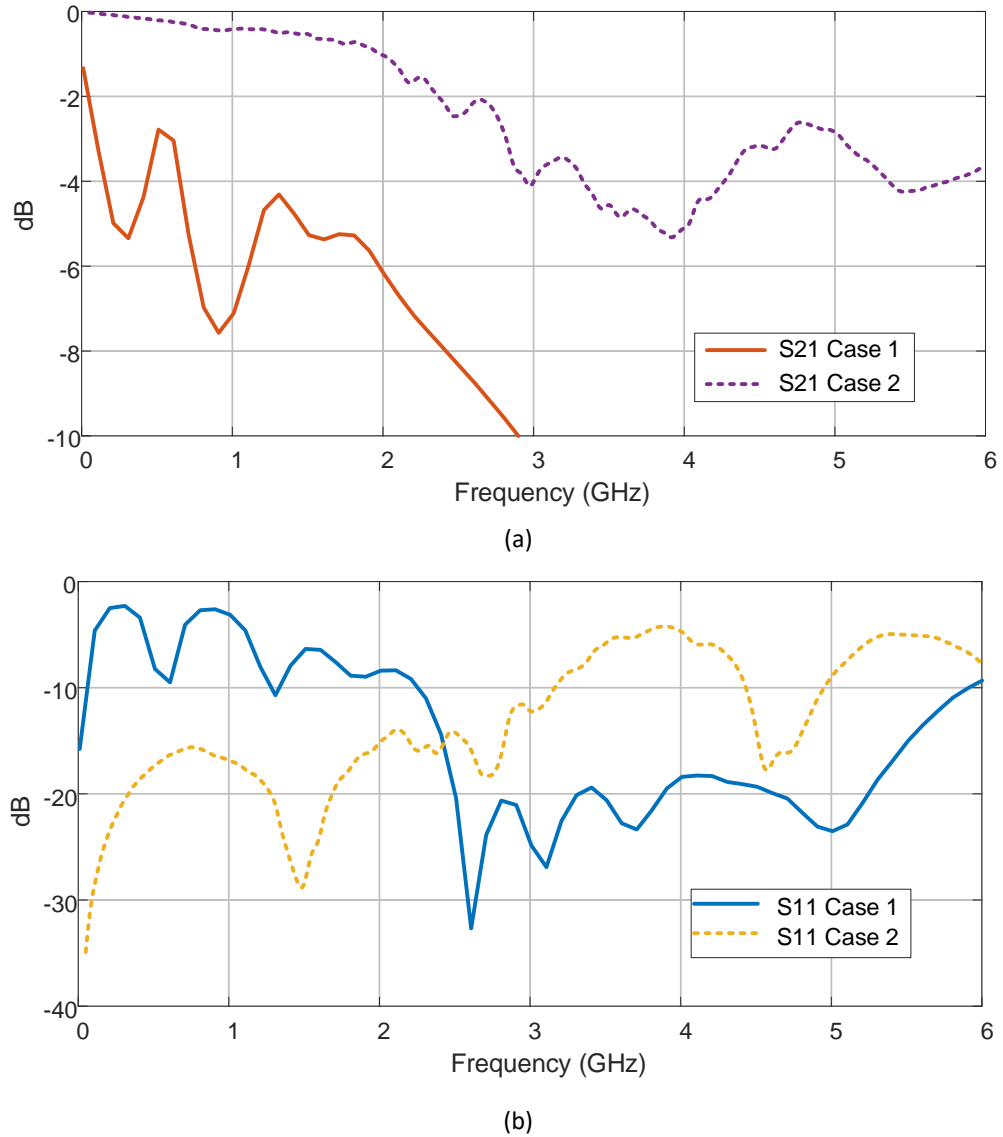
Figure 2.21: Wet test was performed for in two ways: Case 1 when cable is completely wet and case 24 hours after being wet. (a) Measured S_{21} of the fabricated textile coaxial cable. (b) Measured S_{11} of the cables for both cases.

once dry and maintains the same results as shown for dry condition (see Fig. 3.3). The reason for the poor performance of the cable in wet conditions is due to the high dielectric constant and losses in water. To investigate further these losses a model of the textile coaxial cable was designed in the simulations. The results were investigated for both dry and wet conditions. Table 2.5 shows the variation of relative dielectric permittivity (ϵ_r) and loss tangent ($tan\delta$) over different frequency ranges for dry and wet conditions. Based on results, for wet condition cables works best between 0-3 GHz with $\epsilon_r = 8.0$-9.0 and $tan\delta = 0.23$-0.26. For dry condition, $\epsilon_r = 2.10$ and $tan\delta = 0.03$-0.075.

2.5.4   Electromagnetic Coupling (EMC) Test

Another important parameter that needs to be taken into account is the electromagnetic shielding of the cables. Shielding effectiveness can simply be defined as the materials' ability to reduce the transmission of propagating fields in order to electromagnetically isolate one region from another. The electromagnetic performance of the cable can be deteriorated by electromagnetic interference. A good quality coaxial cable has a tight and dense braid. The shield in a poor quality cable is loose and will practically unravel itself when the jacket is removed.

The EMC test was done by using the three-port system as shown in the schematic in Fig. 2.22. The device under test (DUT) is the textile coaxial cable prototypes and the power source is a UHF, a GSM, and an X-band antennas with the power of +15 dBm transmitting to the DUT. If the coupling between each antenna and the DUT is below -40 dB then the cable is considered to be electromagnetically shielded up to 10 GHz. Table 2.6 shows the coupling values at the UHF, GSM and X-band frequencies of the cables measured in this test. From the EMC test, it can be seen that the cables have good shielding effectiveness for audio frequencies and radio frequencies.
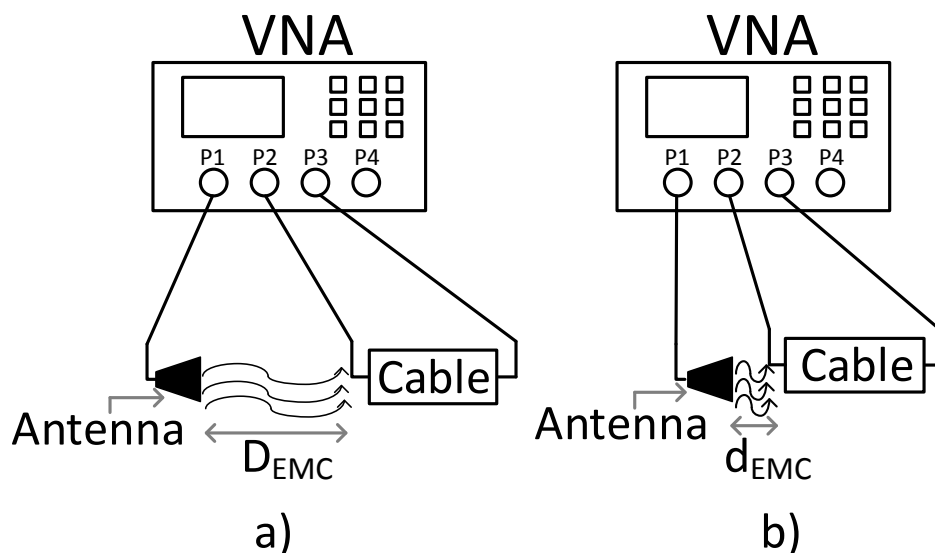
Figure 2.22: Illustration for the setup of EMC test on the fabricated textile coaxial cables. D_{EMC} and d_{EMC} are the far and near distances, respectively, between the antenna and the cable under test.
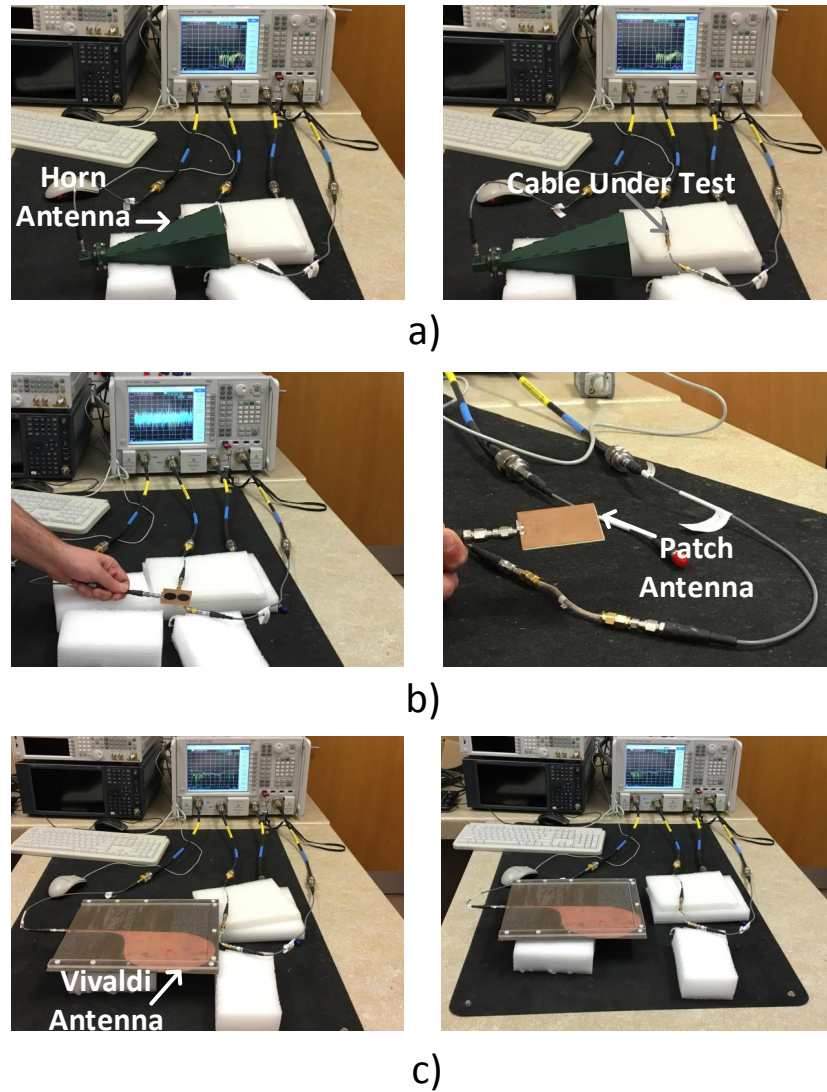
Figure 2.23: Measurement setup of the EMC test using three different antenna operating at (a) X-band, (b) L-band and (c) UHF band.

It is worth mentioning here that the shielding effectiveness of the textile cables is not as good as the commercial cable due to the presence of a cover that is completely metallic around the outer conductor of the cable. This metallic cover acts as a shield and hence has a good shielding effect. The textile cable prototypes presented in this work have outer conductor yarn as a combination of polyester and copper; so this mesh spacing can allow electromagnetic energy to couple into the line. Generally, it is shown that with an increase in the frequency the coupling values increase due to the mesh spacing is closer to the size of the wavelength.

Table 2.6: Performance of fabricated cable during EMC test

Frequency [GHz]	d_{EMC} [mm]	Polyester Sample 1	Polyester Sample 2	Polyester Sample 3
0.4	60	-59.10 dB	-70.30 dB	-53.00 dB
2.45	100	-43.90 dB	-44.10 dB	-65.00 dB
2.45	0	-30.50 dB	-31.20 dB	-45.50 dB
10	30	-55.70 dB	-60.80 dB	-49.20 dB

2.5.5 DC analysis

A Kelvin 4-wire resistance method [37] has been used to perform DC analysis on the fabricated coaxial cable prototypes. This method is used as it eliminates any effect of fixture resistance to obtain a precise resistance value of the DUT. Inspired from Kelvin 4-wire resistance measurement method, an experimental setup was designed to measure the DC resistance of the textile cable prototypes as shown in Fig. 2.24(a) and (b). This setup was designed in-house in Heriot-Watt University by the author. To check whether the setup is working accurately the ohmic losses of the inner conductor for a four-inch commercial cable were measured. From the datasheet provided by the supplier of the commercial cable, the ohmic loss of the inner conductor of the commercial cable is found out to be 212.6 mΩ/m and the value achieved from our measurement setup is 214.6 mΩ/m. This gave us the surety that our measurement set up was working meticulously and can measure efficiently. Prior to the measurement of the DC resistive losses of the textile cables the conductivity of each type of the textile cables was calculated. The comparison of the DC resistive losses for the inner conductor of the textile cable prototypes was measured, calculated, and are shown in table 2.7. The results show PTFE sample 2 has a slightly lower ohmic loss as compared to the other fabricated prototypes. Also, the DC resistive losses for all the textile cables are lower than the commercial cables. Table 2.8 lists DC resistive losses for the outer conductor of the textile coaxial cables. The polyester-based cables have reduced DC losses as compared to the PTFE cables due to the higher conductivity and thickness of the material used for the outer conductor. We know that the copper has large conductivity due to high current density and even low electric field pulls a lot current through it [38]. So, in that case, a thin copper wire has large resistance and thick copper wire will have smaller resistance.

In PTFE sample 1, the outer conductor has an equal distribution of the copper and polyester with the thickness of 0.95 mm and the effective conductivity is 2.59×10^6 S/m that is smaller as compared to the effective conductivity of the polyester cables and the PTFE sample 2. Hence, the DC resistance of the PTFE sample 1 cable is higher (see table 2.8). On the other hand, PTFE sample 2 copper as its outer conductor that increases the effective conductivity and should technically have lower ohmic losses. But the outer conductor of PTFE sample 2 is thinner as compared to other prototypes that will allow less flow of charge which eventually contributes
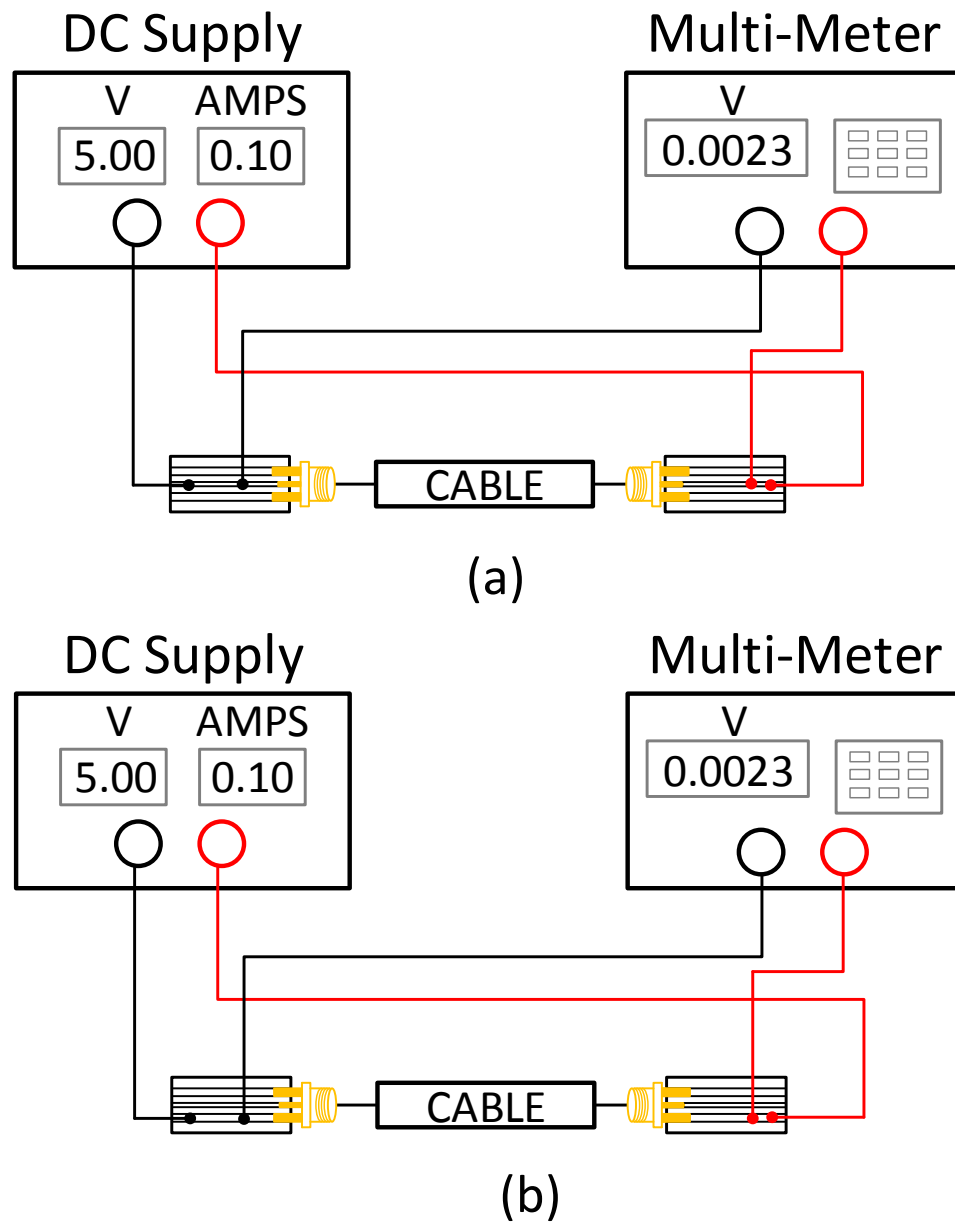
Figure 2.24: An experiment set up of DC analysis for the manufactured textile cable prototypes. (a) DC analysis for the inner conductor and (b) DC analysis for the outer conductor.

Table 2.7: DC Resistive Losses: Inner Conductor

Cables	Measured Voltage [V]	Resistance (Ω)	Length [cm]	Ohmic Losses [Ω/m]
Polyester Sample 1	0.0019	0.019	10.6	0.18
Polyester Sample 2	0.0018	0.018	10.1	0.17
Polyester Sample 3	0.0018	0.018	10.1	0.17
PTFE Sample 1	0.0019	0.019	11.2	0.17
PTFE Sample 2	0.0017	0.017	11.2	0.15

to the increase in the DC resistance. The ohmic loss per meter for all textile cable samples is on the order of 0.1 Ω/m or less.

Table 2.8: DC Resistive Losses: Outer Core

Cables	Measured Voltage [V]	Resistance (Ω)	Length [cm]	Ohmic Losses [Ω/m]
Polyester Sample 1	0.0076	0.076	10.6	0.072
Polyester Sample 2	0.0008	0.008	10.1	0.079
Polyester Sample 3	0.0008	0.008	10.3	0.076
PTFE Sample 1	0.0013	0.013	11.2	0.116
PTFE Sample 2	0.0011	0.011	11.2	0.097

Based on the theory, if we increase the cross-sectional area of the fabricated cable then it will decrease the ohmic losses. Based on this theory, an analytical study was done to improve the ohmic losses of the fabricated textile cables. For this analysis,

the effective conductivity was constant and the surface area of each cable was varied. Table 2.9 shows the increase in the outer conductor diameter. To minimize DC resistive loss this is suggested as the PTFE cables offer the best performance in terms of minimal RF loss. Given the new dimensions mentioned in table 2.9 for the outer conductor, we estimate the DC resistive loss for PTFE samples 1 and 2 to be 66.10 and 66.40 mΩ/m, respectively. These values are very close to the measured DC resistive loss for the outer conductor of the commercial cable that is 66 mΩ/m.

Table 2.9: Improved DC Losses: Outer Conductor

Cables	Diameter original [mm]	Measured Ohmic Loss [Ω]	New Estimated Diameter [mm]	New Estimated Ohmic Loss [Ω]
Polyester Sample 1	2.70	0.11	3.24	0.06
Polyester Sample 2	2.35	0.09	2.47	0.06
Polyester Sample 3	2.16	0.07	No Change	No Change
PTFE Sample 1	2.41	0.07	2.51	0.06
PTFE Sample 2	2.78	0.07	2.90	0.06

2.6 Summary

Due to the limitations presented by commercial cables in modern communication systems for wearable applications, a simple and efficient alternative has been presented in this chapter. This new textile coaxial cable is manufactured from textile material such as polyester and PTFE yarns. Five prototypes were presented in this chapter out of which three are made from polyester material and two are made from PTFE material. The compact and low profile textile coaxial cables posses low reflection coefficient in the UHF and ISM band frequencies. In particular, PTFE

sample 2 has a low reflection coefficient and return loss from DC to 6 GHz. Also, the return loss of the rest of the cable prototypes is low up to 3 GHz.

Since the cables are designed for the wearable application, the robustness tests such as bending and wet test were performed. In bending, PTFE sample 2 yielded best performance for 90°, 180° and loop-like condition for both S_{11} and S_{21}. Whereas, polyester sample 1 and PTFE sample 1 show similar performance. But polyester sample 2 and sample 3 were worst although they work fine up to 2 GHz. For the wet test, the cables were measured for two conditions (1) very wet and (2) 24 hours after being wet. For case 1, the performance of the cables starts declining as soon as it comes in contact with water. But for case 2, the cables regains the performance and works efficiently as soon as it is dried. A study was done to improve the performance of the cables when it is wet and this new estimate result shows that the cables can work efficiently as desired.

In addition, the shielding effectiveness of the prototype is measured using an electromagnetic compatibility test. This test was done by using three different antennas operating at three different frequency bands. EMC test showed that the cable has good shielding effectiveness that is below -40 dB. Moreover, the DC analysis was performed on the fabricated prototypes and ohmic losses of the cables were measured. The ohmic losses of inner and outer conductors were measured and compared with commercial cables. The losses in PTFE cables were higher as compared to the polyester cables. To improve the losses in PTFE cable an analytical study was done and results were presented in this chapter. More importantly, the proposed textile cables are a new innovative approach for wearable antenna applications where connection to the antenna is an important criterion.

References

[1] H. Meng, S. Chen, Y. L. Guan, C. L. Law, P. L. So, E. Gunawan, and T. T. Lie, "A transmission line model for high-frequency power line communication channel," in *Proceedings. International Conference on Power System Technology*, vol. 2, Oct 2002, pp. 1290–1295 vol.2.

[2] D. M. Pozar, *Microwave engineering.* John Wiley & Sons, 2009.

[3] C. R. Paul, *Introduction to electromagnetic compatibility.* John Wiley & Sons, 2006, vol. 184.

[4] C. Hertleer, A. V. Laere, H. Rogier, and L. V. Langenhove, "Influence of relative humidity on textile antenna performance," *Textile Research Journal*, vol. 80, no. 2, pp. 177–183, 2010. [Online]. Available: https://doi.org/10.1177/0040517509105696

[5] C. Nguyen, *Transmission Lines.* Singapore: Springer Singapore, 2016, pp. 3191–3272. [Online]. Available: https://doi.org/10.1007/978-981-4560-44-3_129

[6] Z. Xu, T. Kaufmann, and C. Fumeaux, "Wearable textile shielded stripline for broadband operation," *IEEE Microwave and Wireless Components Letters*, vol. 24, no. 8, pp. 566–568, Aug 2014.

[7] R. C. Johnson and H. Jasik, "Antenna engineering handbook," *New York, McGraw-Hill Book Company, 1984, 1356 p. No individual items are abstracted in this volume.*, 1984.

[8] I. Poupyrev, N.-W. Gong, S. Fukuhara, M. E. Karagozler, C. Schwesig, and K. E. Robinson, "Project jacquard: interactive digital textiles at scale," in

Proceedings of the 2016 CHI Conference on Human Factors in Computing Systems, 2016, pp. 4216–4227.

[9] X. Tao, *Smart fibres, fabrics and clothing: fundamentals and applications.* Elsevier, 2001.

[10] J.-S. Roh, "Textile touch sensors for wearable and ubiquitous interfaces," *Textile Research Journal*, vol. 84, no. 7, pp. 739–750, 2014.

[11] D. Shuaib, L. Ukkonen, J. Virkki, and S. Merilampi, "The possibilities of embroidered passive uhf rfid textile tags as wearable moisture sensors," in *2017 IEEE 5th International Conference on Serious Games and Applications for Health (SeGAH)*, April 2017, pp. 1–5.

[12] T. F. Kennedy, P. W. Fink, A. W. Chu, N. J. Champagne, G. Y. Lin, and M. A. Khayat, "Body-worn e-textile antennas: The good, the low-mass, and the conformal," *IEEE Transactions on Antennas and Propagation*, vol. 57, no. 4, pp. 910–918, April 2009.

[13] P. G. Elliot, E. N. Rosario, B. Rama Rao, R. J. Davis, and N. M. Marcus, "E-textile microstrip patch antennas for gps," in *Proceedings of the 2012 IEEE/ION Position, Location and Navigation Symposium*, April 2012, pp. 66–73.

[14] D. Cottet, J. Grzyb, T. Kirstein, and G. Troster, "Electrical characterization of textile transmission lines," *IEEE Transactions on Advanced Packaging*, vol. 26, no. 2, pp. 182–190, May 2003.

[15] A. Ali, V. Baheti, M. Z. Khan, M. Ashraf, and J. Militky, "Development of electrically conductive composites based on recycled resources," *The Journal of The Textile Institute*, vol. 111, no. 1, pp. 16–25, 2020.

[16] H. M. Dietel and B. Deitel, *An introduction to information processing.* Academic Press, 2014.

[17] V. Zhurbenko, *Passive microwave components and antennas.* BoD–Books on Demand, 2010.

[18] Q. Shi, U. Trltzsch, and O. Kanoun, "Analysis of the parameters of a lossy coaxial cable for cable fault location," in *Eighth International Multi-Conference*

on Systems, Signals Devices, March 2011, pp. 1–6.

[19] N. Marcuvitz, *Waveguide handbook*.   Iet, 1951, no. 21.

[20] N. Nahman, "A discussion on the transient analysis of coaxial cables considering high-frequency losses," *IRE Transactions on Circuit Theory*, vol. 9, no. 2, pp. 144–152, June 1962.

[21] I. Locher and G. Troster, "Fundamental building blocks for circuits on textiles," *IEEE Transactions on Advanced Packaging*, vol. 30, no. 3, pp. 541–550, Aug 2007.

[22] J.-H. Byun, "The analytical characterization of 2-d braided textile composites," *Composites Science and Technology*, vol. 60, no. 5, pp. 705–716, 2000.

[23] P. Potluri and S. Nawaz, "Developments in braided fabrics," *Specialist Yarn and Fabric Structures. Cambridge: Woodhead Publishing Limited*, pp. 333–353, 2011.

[24] C. Hertleer, A. Tronquo, H. Rogier, and L. Van Langenhove, "The use of textile materials to design wearable microstrip patch antennas," *Textile Research Journal*, vol. 78, no. 8, pp. 651–658, 2008.

[25] Z. Wang, L. Zhang, Y. Bayram, and J. L. Volakis, "Embroidered conductive fibers on polymer composite for conformal antennas," *IEEE Transactions on Antennas and Propagation*, vol. 60, no. 9, pp. 4141–4147, Sep. 2012.

[26] S. Zhang, A. Chauraya, W. Whittow, R. Seager, T. Acti, T. Dias, and Y. Vardaxoglou, "Embroidered wearable antennas using conductive threads with different stitch spacings," in *2012 Loughborough Antennas Propagation Conference (LAPC)*, Nov 2012, pp. 1–4.

[27] D. K. Ghodgaonkar, V. V. Varadan, and V. K. Varadan, "Free-space measurement of complex permittivity and complex permeability of magnetic materials at microwave frequencies," *IEEE Transactions on Instrumentation and Measurement*, vol. 39, no. 2, pp. 387–394, April 1990.

[28] M. J. Akhtar, L. E. Feher, and M. Thumm, "A waveguide-based two-step approach for measuring complex permittivity tensor of uniaxial composite mate-

rials," *IEEE Transactions on Microwave Theory and Techniques*, vol. 54, no. 5, pp. 2011–2022, May 2006.

[29] Heping Yue, K. L. Virga, and J. L. Prince, "Dielectric constant and loss tangent measurement using a stripline fixture," in *1998 Proceedings. 48th Electronic Components and Technology Conference (Cat. No.98CH36206)*, May 1998, pp. 1077–1082.

[30] P. Queffelec, P. Gelin, J. Gieraltowski, and J. Loaec, "A microstrip device for the broad band simultaneous measurement of complex permeability and permittivity," *IEEE Transactions on Magnetics*, vol. 30, no. 2, pp. 224–231, March 1994.

[31] J. Baker-Jarvis, M. D. Janezic, P. D. Domich, and R. G. Geyer, "Analysis of an open-ended coaxial probe with lift-off for nondestructive testing," *IEEE Transactions on Instrumentation and Measurement*, vol. 43, no. 5, pp. 711–718, Oct 1994.

[32] B. Milovanovic, S. Ivkovic, and V. Tasic, "A simple method for permittivity measurement using microwave resonant cavity," in *12th International Conference on Microwaves and Radar. MIKON-98. Conference Proceedings (IEEE Cat. No.98EX195)*, vol. 3, May 1998, pp. 705–709 vol.3.

[33] M. S. Boybay and O. M. Ramahi, "Material characterization using complementary split-ring resonators," *IEEE Transactions on Instrumentation and Measurement*, vol. 61, no. 11, pp. 3039–3046, Nov 2012.

[34] C. A. Balanis, *Antenna theory: analysis and design.* John wiley & sons, 2016.

[35] D. Systemes, "Cst studio suite," 2019.

[36] I. J. Bahl and P. Bhartia, *Microwave solid state circuit design.* John Wiley & Sons, 2003.

[37] Z. Ying-wei, "Application of making resistance measurements technology using kelvin 4-wire method," *Semiconductor Technology*, vol. 11, 2005.

[38] C. A. Balanis, *Advanced engineering electromagnetics.* John Wiley & Sons, 1999.

Chapter 3

Wearable Patch Antenna Design using Polydimethylsiloxane (PDMS)

In this chapter a compact and flexible circular polarized (CP) wearable patch antenna is proposed. Polydimethylsiloxane (PDMS) is used as a substrate for the proposed wearable antenna. The proposed antenna is designed for wearable application related to military search and rescue operations. Therefore, the antenna is robust and durable to be able to operate in extreme environmental, for example, different temperature ranges (high or low) and in wet conditions. The chapter is outlined as follows. Section 3.1, the design motivation of the proposed antenna for intended wearable application is described while also providing literature review on previous reported wearable PDMS antennas. In Section 3.2, the design, simulation and fabrication of the proposed antenna is described. Measurement results such as reflection coefficient, radiation pattern in free space and when the antenna is inside ballistics jacket, and robustess test such as bending, wet and temperature tests are described in Section 3.3. Summary of the chapter is discussed in Section 3.4.

3.1   Introduction

The advancement in wearable technology is growing at a very high rate. As a result, many multinational companies such as Nike, Google, Apple, Philips, and Levi's are

using wearable technology in their products. The vision behind wearable antennas is to make the technology part of humans day-to-day life, where the antenna is embedded in the clothing [1]. Nowadays most of the devices are operated with a wireless connection, which is an important aspect that needs to considered before the design of wearable antennas. For example, a microstrip patch antenna using textile material is designed and developed in [2]. Likewise, in [3], a textile based dual-polarized patch antenna is designed and fabricated.

Wearable antennas and electronic sensors for search and rescue operations, made from flexible materials can be extremely useful. Wearable devices for search and rescue applications is in a way an excellent example of an "Internet of Things" technology. This is because these wearable electronics are integrated within a network of devices, or "things", for wireless connectivity enabling data and location exchange without the need for any human intervention. In this section, a circular polarized (CP) wearable patch antenna using polydimethylsiloxane (PDMS) substrate is developed for military search and rescue operations. Principle characteristics of the wearable antenna are low profile, very low maintenance, small size, flexible, lightweight, reasonable gain, and easy fabrication [4, 5]. Antennas should also have minimal radiation absorption by the human body and radiates away from the body. They should also be efficient in any environment and have a robust structure.

Figure 3.1 shows a pictorial illustration of an antenna system positioned in a ballistic jacket and can be implemented for emergency services. Besides operating frequency, circular polarization is one of the most important features in the design process of the antenna because it is more resistant to signal degradation due to atmospheric conditions, shows greater immunity to multipath distortions, fading robustness with better mobility and allows free-range of motion for the users [6]. Circular polarization can be achieved in three ways: (1) by tuning the probe position, (2) by the trimming the opposite corners of the patch, and (3) by placing a diagonal slot in the patch [7]. The circular polarization was achieved by trimming opposite corners of a square patch.

It should be mentioned that several wearable antennas of different shapes and sizes operation at the ISM band were developed over the past few years. These antennas can be described as E-shaped [8], dual-band G-shape [9], small size button-shaped antenna [10] and belt buckle shaped patch antenna [11]. In [5], a review on different

types of antennas along with various substrate materials were presented. To design wearable antennas operating at the ISM band, dipole and patch antennas were studied because of their small size and low cost. Most importantly, the antenna should be robust and resilient to rough environmental conditions and be washable. Furthermore, this antenna needs to be durable and robust which means that they should not rust since the antenna can be placed inside the clothes such as ballistics jacket, life jacket, or any other garment which may become wet or moist. Also, the antenna is designed to be worn and hence should not be rigid. Because of the aforementioned conditions on environmental harshness, washing, robustness, durability, and flexibility, an adequate substrate needs to be chosen.

Figure 3.1: Illustration of a wearable antenna intergtated within the ballistics jacket [12].

3.1.1 PDMS substrate

It is known that several properties can influence antenna performance. For instance, the bandwidth and the efficiency of a microstrip antenna are mainly determined by the permittivity and thickness of the substrate. The wearable antenna should be durable and resilient to a harsh environment and especially when considering the applications of military search and rescue operations. One potential material that could meet the requirement of the wearable antenna is PDMS. In [13], the loss tnagent and dielectric constant of the PDMS material was measured and found to be 0.03 and 2.76, respectively for frequency range 0.2 GHz to 5 GHz. The variation of dielectric constant and loss tangent over frequency (0.5 GHz to 5 GHz) of the pure PDMS material has been presented in [14]. It can be concluded that the PDMS has a dielectric constant as 2.8 and loss tangent approximately 0.02 at 2.45 GHz.

Additionally, the flame resistant and hydrophobic property [15] makes it appealing for wearable applications. The hydrophobic characteristic of PDMS makes it stable across a wide range of environments by preventing changes in relative dielectric constant and loss tangent.

PDMS is a silicone-based elastomer, is chemically inert and thermally stable, offers good resistance to UV radiation, is highly permeable to gases, offers shear stability (in terms of mechanical shearing), has excellent dielectric strength[1] and exhibits isotropic homogeneous properties [15], [17]. PDMS is liquid initially that hardens when the proper polymerizer is added. The process of polymerization lasts for one day. The PDMS material is one of the best replacement to more conventional textile materials because it is waterproof, weatherproof, low cost, easy to fabricate, has a low permittivity, and is flexible. Factors that are considered while designing a flexible antenna are as follows: low dielectric constant of the substrate to maintain antenna efficiency, the thickness of the substrate, moisture content, and mechanical deformation.

3.2   Antenna Configuration

The designed and fabricated CP patch antenna can be seen in Fig. 3.2. The antenna simulation and optimization were conducted using CST Studio Suite. The antenna for data transmission at the ISM band (2.45 GHz) is a probe fed CP patch antenna fabricated with the PDMS substrate. Equations used to design this antenna can be found in [7], [18]. The total dimensions of the antenna are $0.4\lambda_o \times 0.4\lambda_o$ and the height is $0.026\lambda_o$. The patch itself has dimensions of 28×28 mm out of which 5 mm is clipped on each axis in order to achieve CP. It was observed, by varying the dimension of clipped edges, the bandwidth of the antenna can be tuned.

To provide robustness to the whole antenna structure the patch was fully encapsulated inside the PDMS substrate (see Fig. 3.2). PDMS substrate is also hydrophobic and dust resistant which is an important characteristic for wearable applications. The copper thickness within the PDMS is 0.1 mm which provides mechanical flexibility and better homogenous conductivity. The bottom layer of the antenna is a

---

[1]Dielectric strength is the voltage insulating material can withstand before breakdown occurs [16].
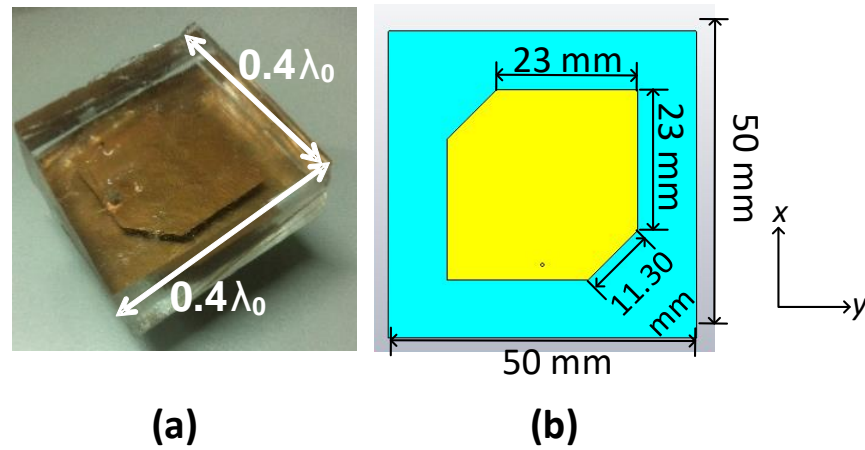
Figure 3.2: PDMS CP patch antenna design: (a) fabricated structure showing overall electrical length [12] and (b) simulated structure showing radiating element dimension.

ground plane made from copper foil. The total weight of the antenna along with the conductor is 57.8g. The thickness of the substrate helped to enhance the bandwidth of the proposed antenna.

3.3 Measurement Results

3.3.1 Reflection Coefficient and Axial Ratio

Figure 3.3 shows the simulated and measured S_{11} of the designed antenna. The S_{11} (simulation and measurement), shown here, suggests that the PDMS CP patch
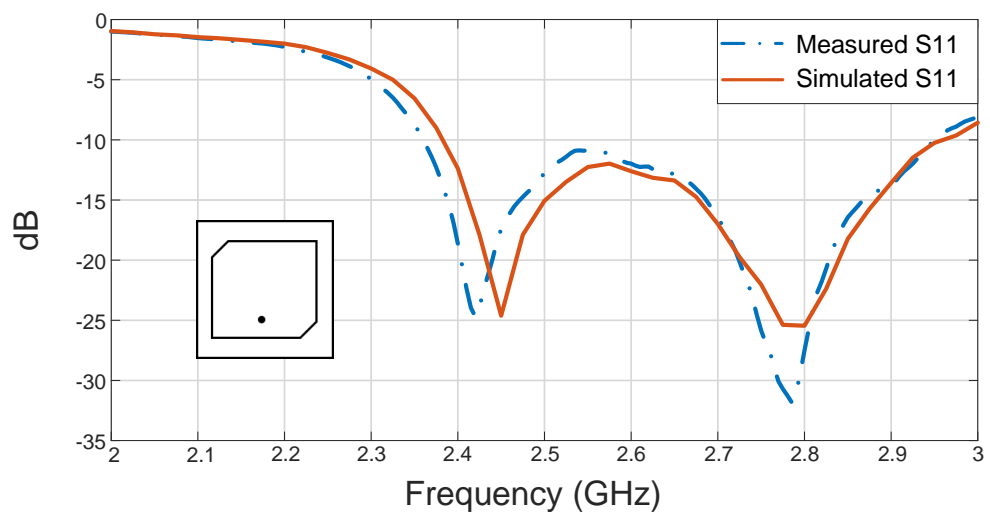
Figure 3.3: Simulated and measured reflection coefficient (S_{11}) of the fabricated CP PDMS patch antenna [12].

antenna radiates power at 2.45 GHz. The simulated and measured results show wideband performance. For example, the simulated $S_{11} \leq$ -10 dB between 2.38 GHz to 2.95 GHz, and for the measured $S_{11} \leq$ -10 dB between 2.35 GHz to 2.95 GHz. The results from S_{11} covers the ISM band frequency range that is 2.45 GHz.

Additionally, between 2.4 and 2.5 GHz, the simulated axial ratio is in good agreement with the measured one. Within this ISM band range, the axial ratio was found to be below 2 dB for both the simulations and measurements. In particular, they are equal to 1.59 dB at 2.45 GHz (simulation) versus 1.7 dB at 2.45 GHz (measurement). The axial ratio results show that the antenna is circular polarized.

3.3.2 Radiation Pattern

The xz- and yz- plane radiation patterns at 2.45 GHz are shown in Fig. 3.4(a) and (b), respectively. The simulated and measured peak cross-polarization levels are at least 19 dB from the main co-pol maximum at broadside. Realized gain of the linear polarized antenna is measured in dBi which is the number of decibel gain of an antenna referenced to the 0 dB gain of a free-space isotropic radiator [19]. Whereas dBic is the absolute gain of the antenna referenced to a circularly polarized
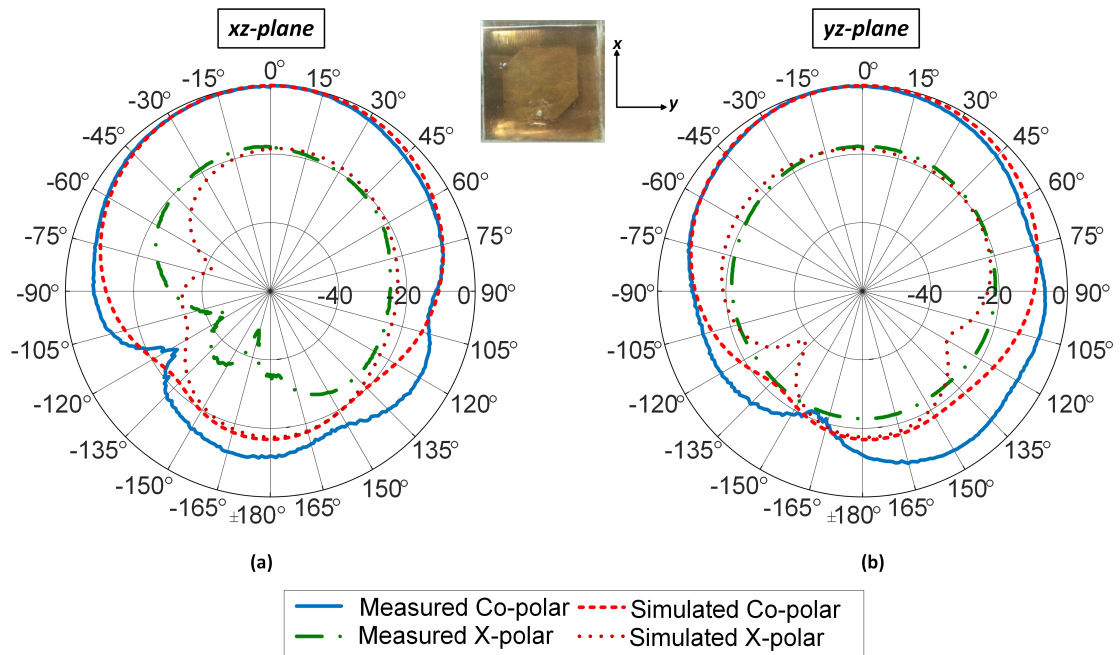
Figure 3.4: Measured and simulated normalized realized gain pattern at 2.45 GHz of the fabricated antenna. (a) Co-polar beam pattern at xz-plane and (b) at yz-plane. Cross polarization values are shown as well [12].

isotropic source [20]. There is a difference of 3-dB between dBi and dBic which is the difference in power received by a linear isotropic and circular isotropic antenna [20]. The realized gain of the proposed antenna for the simulations and measurement was noted as 5.9 dBic. The simulated and measured radiation patterns are in good agreement. The simulated radiation efficiency of the antenna was observed to be 84% at 2.45 GHz.

3.3.3 Measurement with ballistic jacket

Due to the fact that the antenna is meant to be used for search and rescue operations and is easily positioned in other garments, measurements were performed within distinct positions in the ballistics jacket. Specifically, the performance was measured within the front and side of the ballistics jacket as in Fig. 3.5.
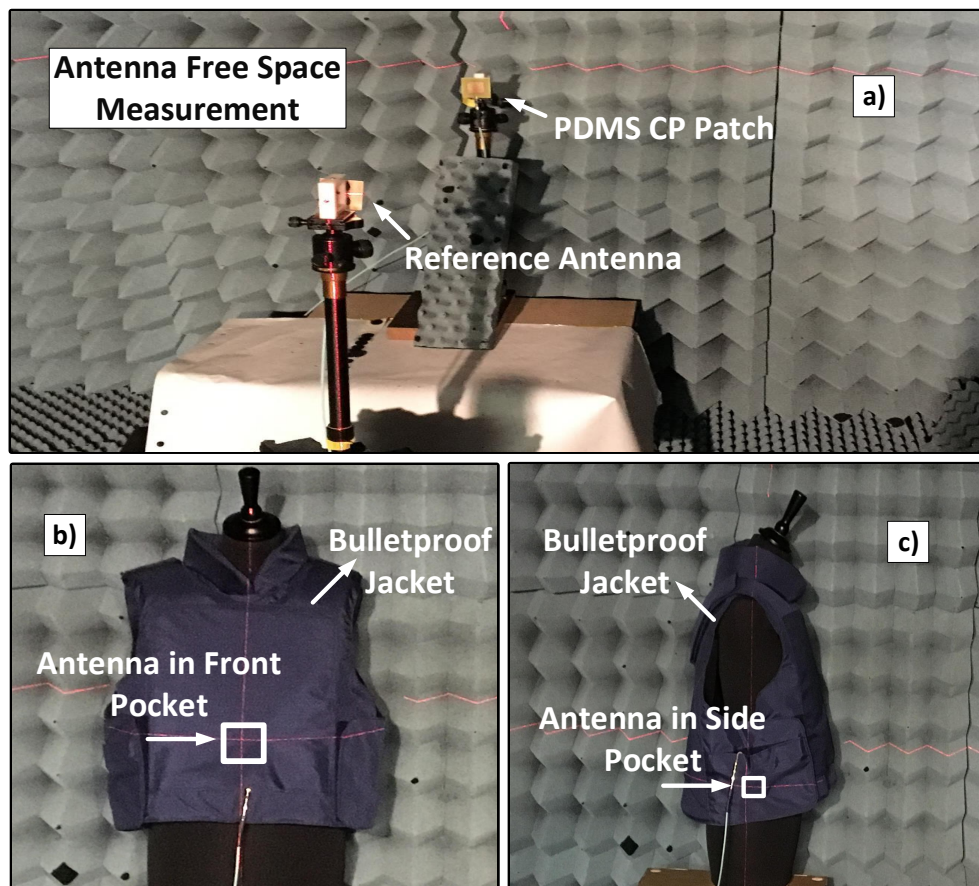
Figure 3.5: (a) Gain measurement setup when the CP patch is in free-space. (b) and (c) Antenna gain measurement setup when CP patch is inside the ballistics jacket [12].

Figure 3.6 shows the S_{11} measurement results of the patch antenna operating at
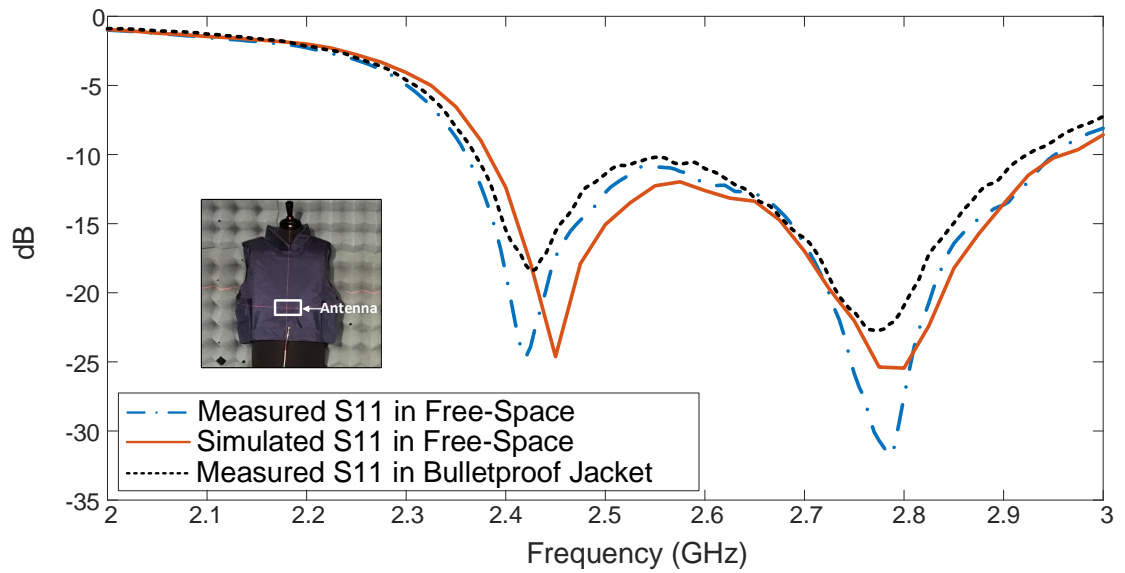
Figure 3.6: Measured S_{11} study when CP patch is within the ballistics jacket and in free-space [12].

the ISM band in free space and when the antenna is placed in the pockets of the jacket. A small shift in frequency is noted which is negligible and does not affect the axial ratio of the antenna. The realized gain of the antenna was measured when the antenna was placed inside the ballistics jacket and compared with the measurements in free-space. Figure 4.5 shows the realized gain of the antenna when placed inside the ballistics jacket. The magnitude is reduced by about 2 dB between free-space measurements and the ones when the antenna is within the ballistics jacket to 2 dB.
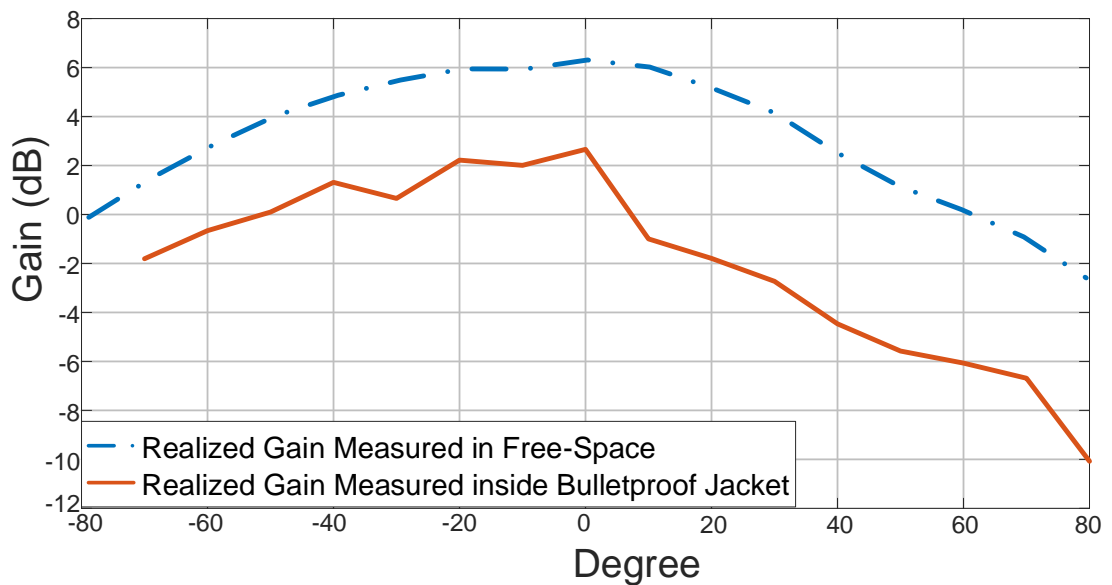
Figure 3.7: Comparison of realized gain at 2.45 GHz when the proposed antenna is in bulletproof jacket and in free space [12].

However, the antenna now shows a circularly polarized realized gain approximately 3 dBic at broadside which means that the antenna still performs well when placed within the ballistics jacket. The reduced realized gain is observed due to two reasons (a) irregular surface of the bulletproof jacket which disturbs the alignment of the antenna under test (AUT) and (b) the presence of bulletproof jacket material (kevlar with dielectric constant 1.66) in between AUT and transmitting antenna. Depending on the application and requirements the antenna can be further optimized at this stage.
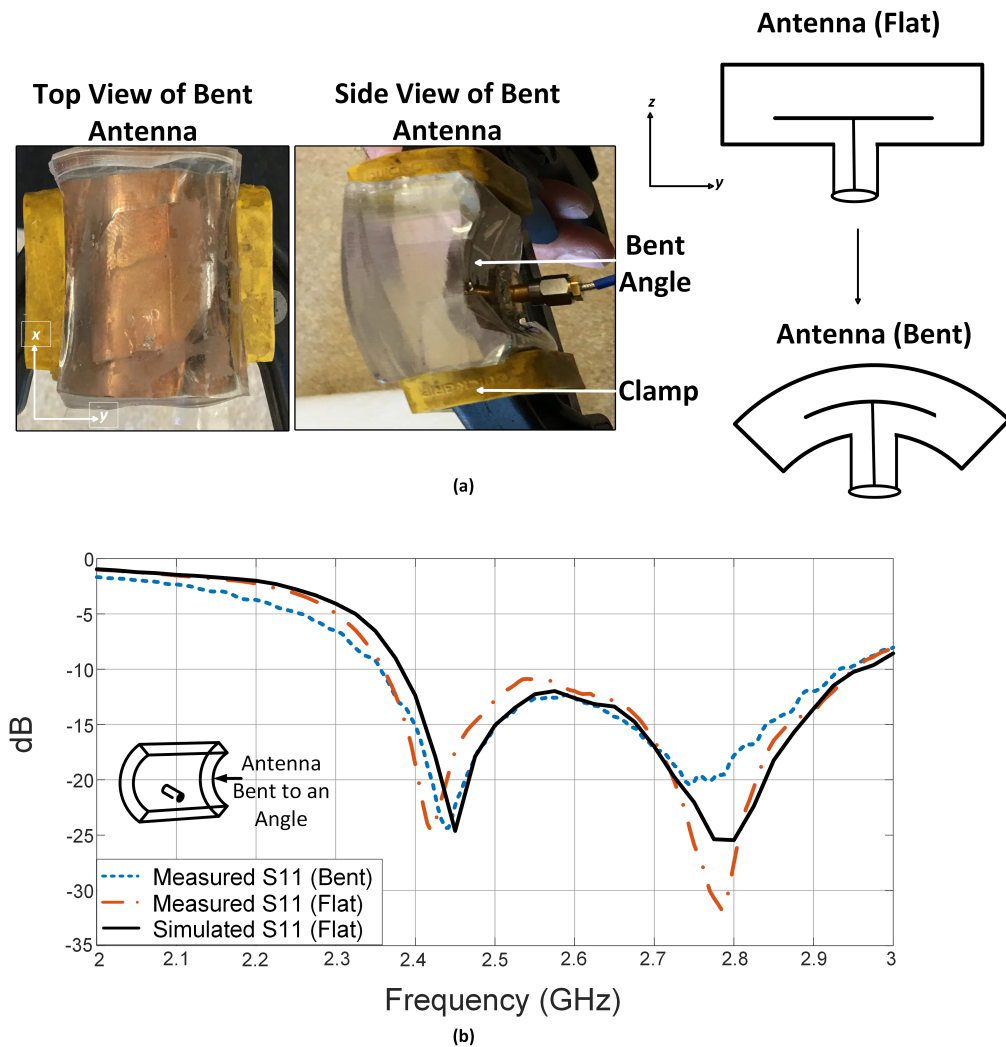
Figure 3.8: (a) Top view (left) and side view (right) of the bending test performed on the CP patch antenna. (b) Measured S_{11} when the CP patch is bent at approx 35° and comparison with measured and simulated S_{11} values for the flat antenna case as shown in Fig. 3.2 [12].

3.3.4 Robustness Tests

In addition to the gain measurements of the CP patch antenna placed inside the ballistics jacket, multiple robustness measurements were conducted such as bending, wet, and temperature tests. Basically to show the resiliency and durability of the PDMS substrate and that the antenna is still operational when wet.

3.3.4.1 Bending Test

For the bending test, the antenna was bent approximately 35° and the S_{11} was measured. Figure 3.8(a) shows the setup for the bending test. Because of the thickness of this antenna, it is not possible to bend it beyond 40°. For measurement, the antenna was placed in between the bending clamps and was bent to its maximum bending tolerance level. Once the antenna was bent the S_{11} was measured. A small shift in frequency is noted when the antenna is bent. Regardless bent or not, this antenna radiates power between 2.4 and 2.5 GHz. A minor drop in realized gain of antenna can be expected due to the bending however this will not effect the circular polarization of the antenna. The S_{11} from the measurements are reported in Fig. 3.8(b) for this experiment.
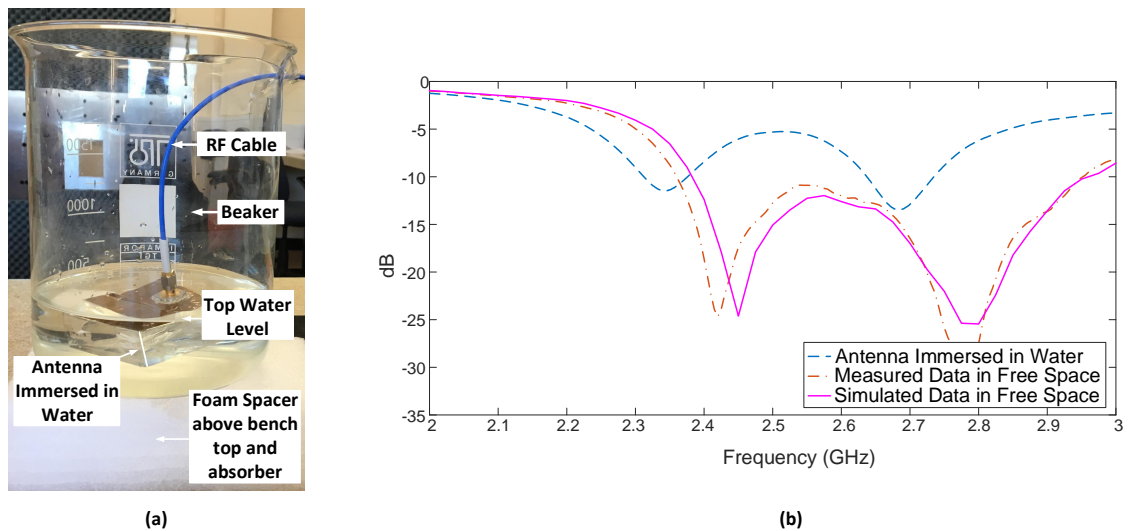
Figure 3.9: (a) Wet Test measurement setup when the CP patch is immersed in water. (b) Measured S_{11} when the CP patch is immersed in water and comparison with measured and simulated S_{11} in free-space [12].

3.3.4.2   Wet Test

For the wet test, the CP patch antenna was put inside a beaker filled with water without the antenna touching the bottom of the beaker. Figure 3.9(a) shows the measurement setup for the wet test of the antenna. It is important to note that even if the antenna does not touch the glass bottom of the beaker, the glass and water combination will have some influence on the antenna operation. This confirmed by the plot shown in Fig. 3.9(b), where a more significant frequency shift is observed for S_{11}. This frequency shift is due to the presence of water which has high dielectric constant. As a result, antenna now radiates power at 2.36 GHz and 2.7 GHz.

3.3.4.3   Temperature Tests

Figure 3.10 shows the S_{11} of the CP patch antenna at +25°C, +100°C and -20°C. The antenna has been exposed for 5, 10 and 20 minute durations respectively to these temperatures and then taken out of the environmental chamber to measure S_{11} instantly. The objective of this test was to ensure that the PDMS antenna is resilient to wide temperature variations. Furthermore, we also measured S_{11} for -10°C, 0°C, +15°C, +30°C, +45°C, +60°C and +80°C. Minor discreapancies were observed in the performance for these temperatures is due to the measurement in accuracy. PDMS material is thermally stable and does not have significant changes
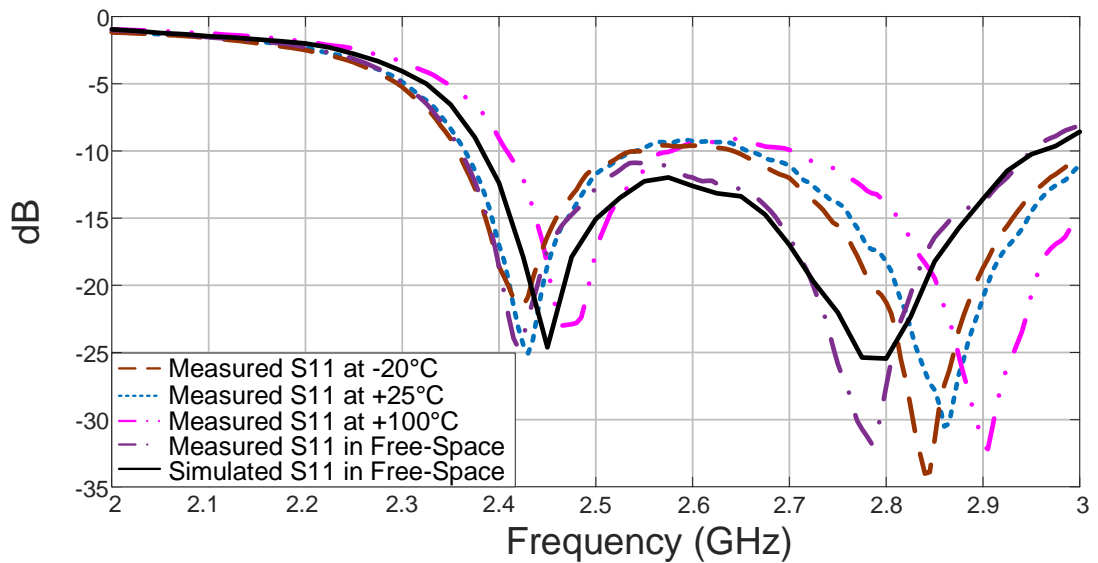
Figure 3.10: Measured S_{11} at -20°C, +25°C and +100°C and comparison with measured and simulated S_{11} in free-space [12].

Table 3.1: S_{11} of the antenna at different temperature durations considering 2.45 GHz.

T°C	5 Minutes	10 minutes	20 Minutes
-20	S_{11} = -16.3 dB	S_{11} = -13.4 dB	S_{11} = -13.1 dB
-10	S_{11} = -16.7 dB	S_{11} = -11.2 dB	S_{11} = -11.2 dB
0	S_{11} = -17.0 dB	S_{11} = -11.8 dB	S_{11} = -11.2 dB
15	S_{11} = -19.0 dB	S_{11} = -12.3 dB	S_{11} = -12.3 dB
25	S_{11} = -18.5 dB	S_{11} = -13.6 dB	S_{11} = -13.1 dB
30	S_{11} = -19.4 dB	S_{11} = -13.3 dB	S_{11} = -16.0 dB
45	S_{11} = -21.0 dB	S_{11} = -15.3 dB	S_{11} = -16.1 dB
60	S_{11} = -24.7 dB	S_{11} = -16.1 dB	S_{11} = -16.1 dB
80	S_{11} = -23.1 dB	S_{11} = -12.9 dB	S_{11} = -12.9 dB
100	S_{11} = -18.5 dB	S_{11} = -10.8 dB	S_{11} = -10.8 dB

in the temperature range from -40°C to +150°C [21]. The measured S_{11} results are summarized in Table 3.1. The S_{11} is below -10 dB which means within the temperature range of -20°C to +100°C, the antenna accepts power foe radiation from 2.4 to 2.5 GHz and is well matched.

3.4   Summary of the Chapter

This chapter describes the work on design, simulation, and measurement of the circularly polarized patch antenna. The objective of this work was to investigate the resiliency of the PDMS substrate. Measurements results provided for the antenna are in close agreement with the simulations. The simulated and measured S_{11} of the proposed antenna is below -15 dB at 2.45 GHz and are in good agreement. The realized gain of the antenna was 5.9 dBic for the simulation and measurement in free-space. The realized gain pattern has also been measured when the antenna was placed inside the ballistics jacket. The performance of the antenna was reported when the antenna was bent, wet and exposed to different temperature ranges to prove the durability of the PDMS substrate. The proposed circular polarized patch antenna demonstrated attributes that are suitable for wearable applications, such as search and rescue and emergency services particularly where the antenna size, cost, and durability is important as well as maintained operation when wet.

References

[1] I. Locher, M. Klemm, T. Kirstein, and G. Troster, "Design and characterization of purely textile patch antennas," *IEEE Transactions on Advanced Packaging*, vol. 29, no. 4, pp. 777–788, Nov 2006.

[2] A. Tronquo, H. Rogier, C. Hertleer, and L. Van Langenhove, "Robust planar textile antenna for wireless body LANs operating in 2.45 GHz ISM band," *Electronics Letters*, vol. 42, no. 3, pp. 142–143, Feb 2006.

[3] L. Vallozzi, H. Rogier, and C. Hertleer, "Dual polarized textile patch antenna for integration into protective garments," *IEEE Antennas and Wireless Propagation Letters*, vol. 7, pp. 440–443, 2008.

[4] S. Alharbi, R. M. Shubair, and A. Kiourti, "Flexible antennas for wearable applications: Recent advances and design challenges," in *12th European Conference on Antennas and Propagation (EuCAP 2018)*, April 2018, pp. 1–3.

[5] N. H. M. Rais, P. J. Soh, F. Malek, S. Ahmad, N. B. M. Hashim, and P. S. Hall, "A review of wearable antenna," in *2009 Loughborough Antennas Propagation Conference*, Nov 2009, pp. 225–228.

[6] N. Hussain, M. Jeong, A. Abbas, T. Kim, and N. Kim, "A metasurface-based low-profile wideband circularly polarized patch antenna for 5G millimeter-wave systems," *IEEE Access*, vol. 8, pp. 22 127–22 135, 2020.

[7] C. A. Balanis, *Antenna theory: analysis and design.* John Wiley & Sons, 2016.

[8] A. Y. I. Ashyap, Z. Zainal Abidin, S. H. Dahlan, H. A. Majid, A. M. A. Waddah, M. R. Kamarudin, G. A. Oguntala, R. A. Abd-Alhameed, and J. M. Noras, "Inverted E-shaped wearable textile antenna for medical applications," *IEEE Access*, vol. 6, pp. 35 214–35 222, 2018.

[9] L. K. H. Salman and L. Talbi, "Dual band G-shape wearable cuff button antenna for ISM bands applications," in *2010 IEEE Antennas and Propagation Society International Symposium*, 2010, pp. 1–4.

[10] O. G. Kwame, Y. Huang, G. Wen, J. Li, and A. E. Ampoma, "Broadband circularly polarized square slot antenna with a G-shaped feedline," in *2017 IEEE International Symposium on Antennas and Propagation USNC/URSI National Radio Science Meeting*, 2017, pp. 117–118.

[11] B. Sanz-Izquierdo and J. C. Batchelor, "A dual band belt antenna," in *2008 International Workshop on Antenna Technology: Small Antennas and Novel Metamaterials*, 2008, pp. 374–377.

[12] R. Joshi, C. Constantinides, S. K. Podilchak, M. N. Ramli, H. Lago, and P. J. Soh, "Robust and compact PDMS antennas for search and rescue operations and emergency communications," in *12th European Conference on Antennas and Propagation (EuCAP 2018)*, 2018, pp. 1–5.

[13] J. Trajkovikj, J. Zrcher, and A. K. Skrivervik, "PDMS, a robust casing for flexible w-ban antennas [EurAAP corner]," *IEEE Antennas and Propagation Magazine*, vol. 55, no. 5, pp. 287–297, 2013.

[14] R. B. V. B. Simorangkir, Y. Yang, R. M. Hashmi, T. Bjrninen, K. P. Esselle, and L. Ukkonen, "Polydimethylsiloxane-embedded conductive fabric: Characterization and application for realization of robust passive and active flexible wearable antennas," *IEEE Access*, vol. 6, pp. 48 102–48 112, 2018.

[15] A. C. Kuo, "Polymer data handbook," *Polymer Data Handbook*, 1999.

[16] S. James, "Monomers, polymers, and plastics." Elsevier, 2011, pp. 1–1.

[17] A. Mata, A. J. Fleischman, and S. Roy, "Characterization of polydimethylsiloxane (PDMS) properties for biomedical micro/nanosystems," *Biomedical microdevices*, vol. 7, no. 4, pp. 281–293, 2005.

[18] R. Garg, P. Bhartia, I. J. Bahl, and A. Ittipiboon, *Microstrip antenna design handbook*. Artech House, 2001.

[19] "IEEE recommended practice for local and metropolitan area networks coexistence of fixed broadband wireless access systems," *IEEE Std 802.16.2-2004*

(Revision of IEEE Std 802.16.2-2001), pp. 1–166, 2004.

[20] B. Y. Toh, R. Cahill, and V. F. Fusco, "Understanding and measuring circular polarization," *IEEE Transactions on Education*, vol. 46, no. 3, pp. 313–318, 2003.

[21] B. K. Gale, M. A. Eddings, S. O. Sundberg, A. Hatch, J. Kim, T. Ho, and S. Karazi, "Low-cost MEMS technologies," 2016.

Chapter 4

Wearable Dual-Band Textile Patch Antenna Using Artificial Magnetic Conductor (AMC) Substrate

In this chapter a novel dual-band and dual sense wearable patch antenna using a textile-based substrate is presented. The proposed antenna is flexible, compact and light weight, and is designed for GPS and WLAN applications. The patch is combined with trucated corners opposite to each other and has four rectangular slits on each corners. For better performance and reduced specific absorption rate (SAR) a 3×3 AMC plane is integrated within the design. It is worth mentioning that the proposed antenna is circularly polarized (CP) at 1.575 GHz and is linear polarized at 2.45 GHz. This chapter is organized as follows. In Section 4.1, the design motivation of the proposed antenna is described with literature review on previously reported dual-band antennas. In Section 4.2, the design evolution and assembly of the antenna is described along with AMC plane. Reflection coefficient in free-space and on-body both in flat and bent conditions are described in Section 4.3. In addition, the radiation of the proposed antenna when bent on-body presented in Section 4.3 while a summary of the chapter is discussed in Section 4.4.

4.1 Introduction

Textiles has been the preferred material due to their comfort, lightweight, high flexibility, and ease of integration with clothing [1]. Such implementation is especially useful in location tracking especially in search and rescue, and also, long-term patient monitoring [2]. Due to these advantages, researchers have envisioned the use of the two widely available methods suitable in both indoor and outdoor for wireless localization: using WLAN for the former, and using the Global Positioning System (GPS) for the latter, using a single antenna. This technology merging using a single wearable device based on textile technology is highly cost-effective, besides improving the comfort for the user [1]. However, the use of such radiators in the vicinity of users typically results in coupling to the human tissues and electromagnetic absorption into parts of the body, especially in the lower microwave frequencies with longer signal wavelengths. Concerns on health may arise if the level of this absorption does not meet its regulatory requirements, defined in terms of Specific Absorption Rate (SAR) [3]. One of the effective methods in reducing the SAR level is by shielding the radiator of the antenna from the body using conventional metallic planes or metasurfaces such as AMC planes.

The concept of integrating dual and multi-frequency antennas is popular in multi-functional wireless products, as it effectively reduces the required number of components and effectively of the hardware. For instance, the dual-frequency antennas in [4], [5] are capable of providing operation in different operating bands with unique radiation features to suit their applications. Meanwhile, the use of circularly-polarized (CP) antennas is advantageous in wireless communications as they allow signal reception irrespective of the orientation of the receiving antenna with respect to the transmitting antenna. This consequently results in the suppression of multipath interference. On the contrary, there needs to be a proper polarization alignment for linearly-polarized antennas when in operation to ensure efficient signal transmission and reception. Meanwhile, it is much less complex to design dual or multiband linearly polarized antennas in comparison to CP antennas operating in multiple bands, making the former the preferred choice for localization in an indoor environment.

In [6], analysis on three different types of CP patch antennas were reported using

a Greens function approach and the desegmentation method. It was found that circular polarization for conventional patch antennas has largest axial ratio bandwidth and can be achieved using a square patch with a diagonal slit, whereas the corner-truncated patch can be used to achieve the best axial ratio levels. In [7], four asymmetric slits were introduced in the diagonal directions to achieve circular polarization. In addition to that work, a patch antenna was designed with truncated corners and four slits with good matching and axial ratio at the operational frequency [8]. Most importantly, the adoption of such a technique effectively miniaturized the size of the antenna by about 36%.

In comparison, the implementation of metasurfaces within antenna designs has increased rapidly in recent years, mainly due to their capability in widening the axial ratio bandwidth and enhancing realized gain. A review on different antenna designs integrated with AMC surfaces was reported in [9]. A dual mode antenna operational at 1.38 GHz and 1.57 GHz was presented in [10]. Furthermore, a dual-band wearable triangular monopole antenna using 4×4 AMC plane was presented in [11]. Besides that, a circular cross slit AMC design was also proposed to improve radiation and enhance bandwidth for UWB antennas. Wide bandwidths are also significant for 5G applications. For example, the bandwidth of a CP patch antenna with a metasurface was reported to be 34.7% in [12] (that is approximately 26.0% better than the antennas which are not integrated with metasurfaces). Similarly, a partially reflected surface (PRS) was used to broaden the bandwidth of a CP Fabry-Perot antenna in [13].

Considering the aforementioned factors, this work aims to design, for the first time and to the best knowledge of authors, a dual-band and dual-sense (linear and circular polarization) textile antenna backed using an artificial magnetic conductor (AMC) plane. This configuration provides further antenna miniaturization and suppression of backward radiation, besides improving gain and bandwidth [14–17], which are extremely attractive features for wearable devices. A preliminary investigation in free space and under bent conditions was presented in [18]. Ultimately, the proposed antenna is capable of a dual-band and dual-sense operation: 1) for indoor wireless localization using WLAN/WBAN standards, operating with linear polarization; as well as; 2) for outdoor location tracking using the GPS standard, operating with circular polarization. Both operations require radiation with their respective linear

and circular polarizations, with the proposed body worn antenna radiating outwards from the body.

4.2   AMC Surface and Antenna Design

The unit cell of the AMC plane is designed based on a square patch, as illustrated in Fig. 4.1. This patch is then integrated with a square ring centered on this patch. This is followed by the addition of four square slits centered at each of its sides. The AMC unit cell is integerated in between two substrates, as illustrated in Fig. 1(b). The bottom-most layer is the ground plane. A layer of felt substrate is placed on top of it, followed by the AMC unit cell. Another subsequent felt substrate layer is placed on top of this AMC unit cell layer, prior to the placement of the radiator on top of this felt substrate layer. The AMC cells and ground plane are built using a
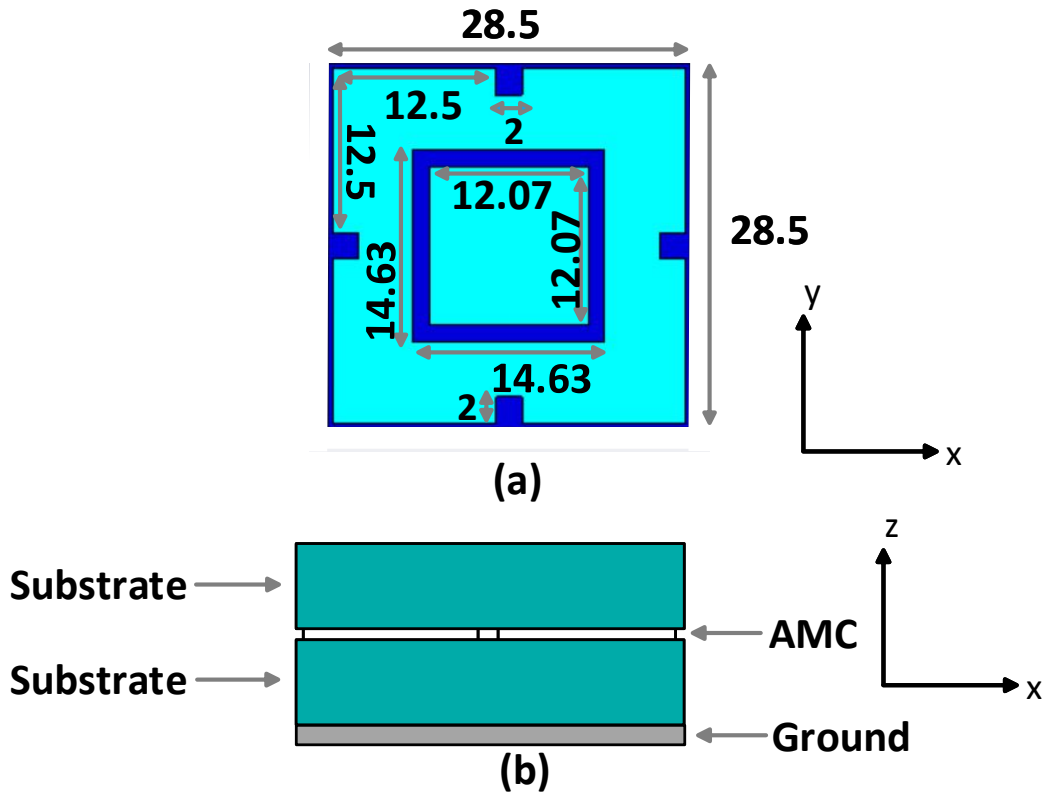
Figure 4.1: AMC unit cell (a) Dimensions of the AMC unit cell (in mm) and (b) AMC unit cell cross section with a substrate thickness of 2.64 mm per layer and conductor (AMC and ground) thickness of 0.17 mm per layer [21].

conductive textile, ShieldIt Super, which is 0.17 mm thick and is highly conductive (with 1.18×10^5 S/m). The substrate, on the other hand, is made using Kevlar, which has a relative permittivity (ϵ_r), of 1.66, a loss tangent ($\tan \delta$) of 0.07 measured at 2.45 GHz, and has 2.64 mm in thickness. To form the AMC plane, this unit cell is then arranged into a 3×3 array. It should be mentioned that the dimensions of the rectangular AMC unit cell can be calculated using the equations mentioned in [19]. The operating frequency can also be changed by tuning the relative dielectric constant of the substrate [20].
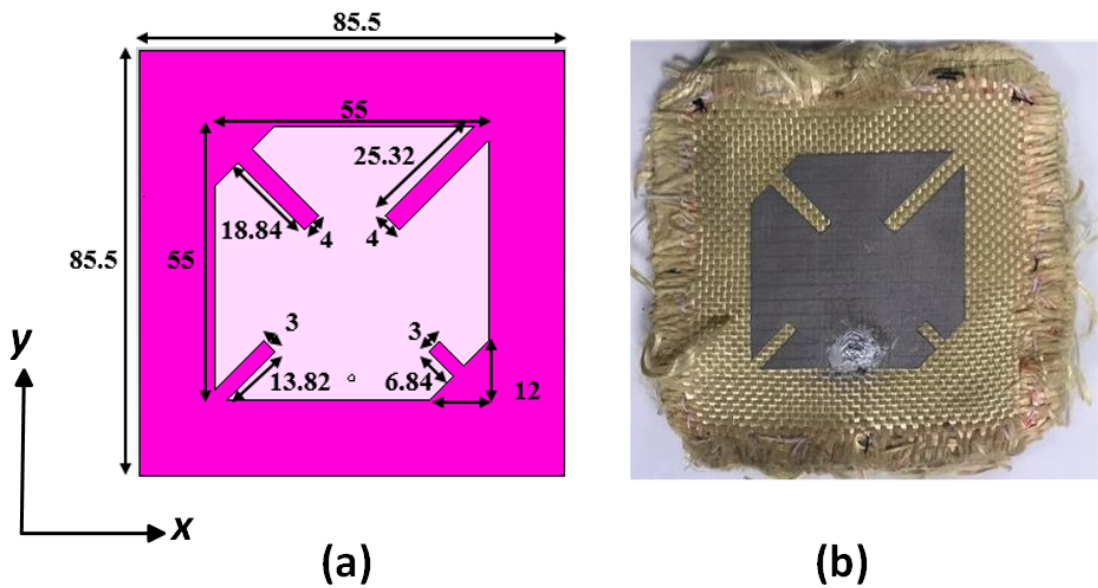
Figure 4.2: Antenna design (a) topology of the dual-polarized planar textile antenna (simulated prototype) (all dimensions in mm) [21] and (b) fabricated prototype.

Next, the radiator (patch) of the antenna was designed. This radiator is intended for dual band operation in the 1.575 GHz and 2.45 GHz bands, as illustrated in Fig. 4.2. To enable a single-fed circularly polarized antenna structure, the square patch radiator is combined with a pair of truncated corners opposite to each other. The lengths of the truncated corners are optimized to be the same at 12 mm. Next, a rectangular slit is integrated onto each side of four corners of the patch to enable dual-band operation.

To further describe the design procedure for the proposed dual-band and dual-sense antenna, it starts from a simple linearly polarized square patch. Typically the antenna is fed from the bottom by a probe and the inner pin of the connector is extended to the patch. Three common ways to achieve circular polarization are: (1) by using a single, dual or more feeds [22], (2) trimming the opposite corners of the
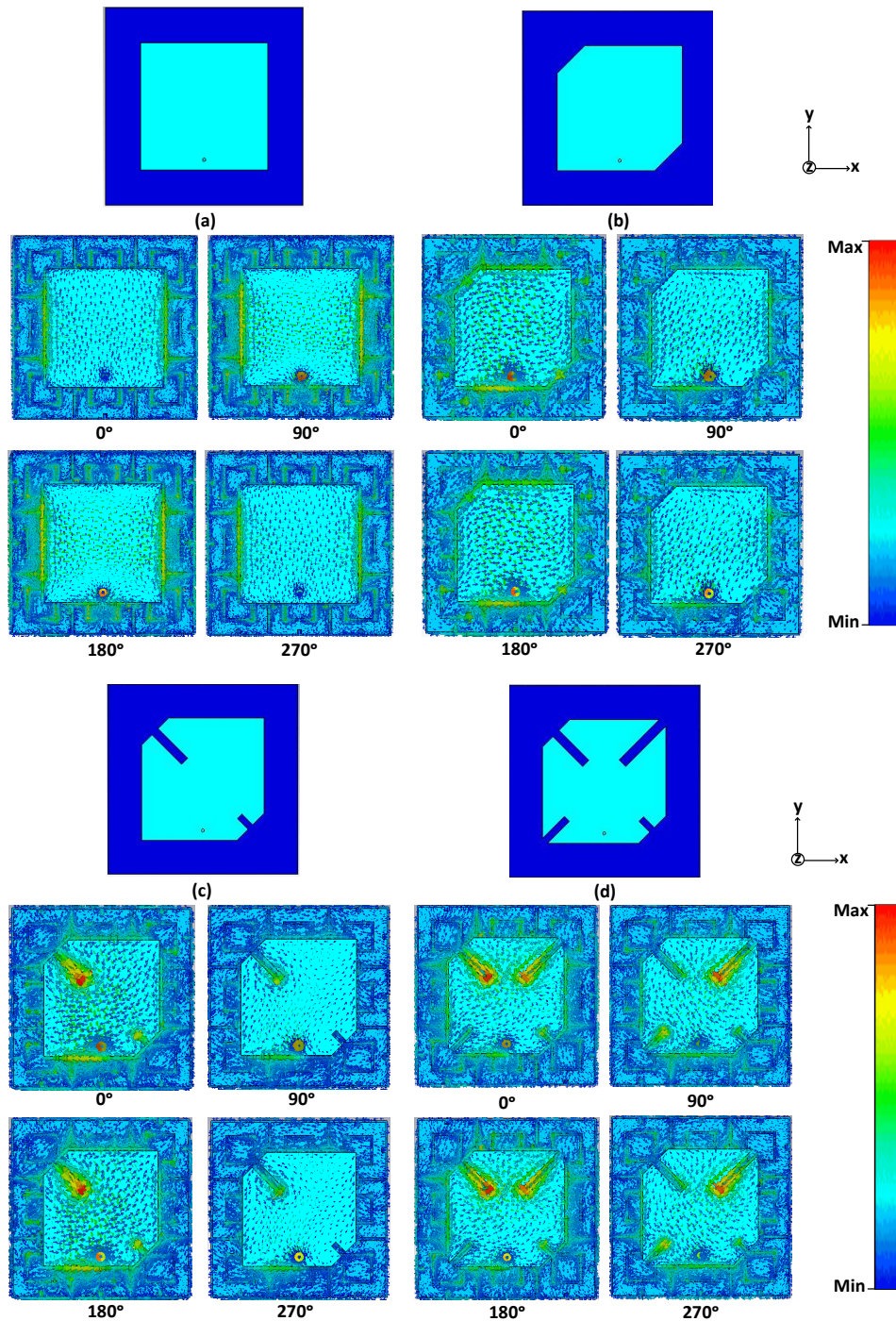
Figure 4.3: Step-by-step illustration of the proposed antenna design evolution. (a) Linear polarized patch antenna at 1.575 GHz. (b) Circular polarized patch antenna operational at 1.575 GHz. (c) Patch antenna with diagonal slits operational at 2.45 GHz. The integration of slits at the truncated corner introduced an upper band frequency resonance. (d) The proposed circular polarized patch antenna with four slits operational at 1.575 GHz and 2.45 GHz. The surface current distribution in A/m at 1.575 GHz are shown for different phase values (at 0°, 90°, 180° and 270°) in each design to illustrate circularly polarized radiation [21].

patch, and (3) introducing thin slits [23]. In the proposed design, a truncated corner technique was used to achieve circular polarization and four slits were inserted at

each corner of the patch to enhance the bandwidth. The resulting surface current distribution at each design stage is illustrated in Fig. 4.3(a-d). The surface current distribution in the lower band for different phase (0°, 90°, 180° and 270°) shows the changes in the current direction illustrating the CP characteristics of the proposed antenna.

It was initially observed that the position of the probe resulted in a dual-band polarization of the proposed antenna. But after further optimization, it was noticed that the slits were contributing towards resonance at the upper band frequency. This provided insight that the upper corners of the patch enabled resonance at 1.575 GHz, whereas the lower corners allowed operation at 2.45 GHz. The antenna can also be tuned to a single frequency operation by adjusting the two truncated corners in the structure. For example, by changing the size of top truncated corner length, one can tune the resonance in the lower frequency band (currently centered at 1.575 GHz). Likewise, tuning the 2.45 GHz frequency band can be performed by adjusting the slits in the lower corners of the antenna.

The overall dimension of the antenna with AMC substrate is $85.50 \times 85.50 \times 5.62$ mm^3. The elctrical length of the proposed antenna is $0.4\lambda_o \times 0.4\lambda_o \times 0.02\lambda_o$ at 1.575 GHz and $0.68\lambda_o \times 0.68\lambda_o \times 0.04\lambda_o$ at 2.45 GHz. It should also be mentioned that the antenna structures of similar function have also been presented previously in the literature [17] but were slightly larger ($110 \times 110 \times 10.2$ mm^3), with capacitive slot-feeding, and employed a hybrid coupler chip to achieve CP operation at 1.575 GHz and, which can increase design complexity. Our proposed antenna, instead, is a simple dual-band and dual-polarized antenna that is probe fed and is realized by patterning of the various metallic layers (see Figs. 4.1 and 4.2).

An analysis was conducted to check the performance of the proposed antenna by changing the size of AMC array and thickness of the substrate between the patch and AMC plane (see Table 4.1) considering off body radiation from a human phantom. Note that the size of AMC array changes the overall size of the antenna structure by at least 35%. For example, a 2×2 AMC array is dimensioned at 61.5×61.5 mm^2 whereas the dimension of a 4×4 AMC array is 115.5×115.5 mm^2. The thickness of the proposed antenna was changed by 1 mm by substrate thickness between the AMC plane and the patch, which is currently at 2.62 mm for the 3×3 array. Table 4.1 summarizes the performance of the proposed antenna with varying AMC array

Table 4.1: AMC array size variation and thickness between the patch and the AMC plane (simulations) when placed on the body

1.575 GHz			
AMC plane size	Structure dimension (mm²)	Thickness between AMC plane and patch (mm)	Radiation Efficiency (%)
		1.62	35.9
2×2	61.5 × 61.5	2.62	59.0
		3.62	63.5
		1.62	63.3
3×3	85.5 × 85.5	2.62	73.6
		3.62	79.2
		1.62	60.6
4×4	115.5 × 115.5	2.62	69.6
		3.62	75.5
2.45 GHz			
		1.62	59.1
2×2	61.5 × 61.5	2.62	75.1
		3.62	77.5
		1.62	76.5
3×3	85.5 × 85.5	2.62	83.0
		3.62	86.1
		1.62	77.9
4×4	115.5 × 115.5	2.62	78.7
		3.62	84.7

sizes and the substrate thickness in terms of radiation efficiency. It is observed that the radiation efficiency improves as the thickness of the antenna is increased in both frequency bands. It is valid that the thickness of the substrate increases the radiation efficiency but also the surface wave increases which is undesirable [24]. Moreover, the improvements in terms of radiation efficiency (of less than 10%) is not of major significance considering the 35% increase in size when using 4×4 array instead of the 3×3 array.

4.3 Results and Discussion

4.3.1 Performance in free space (Planar and Bent condition)

The proposed antenna performance is first studied in free space in terms of its reflection coefficient, bandwidth, and radiation patterns. However, the wearable antenna operation in a planar, free space condition is not the actual intended application, and thus will be studied briefly to obtain an approximate idea of its performance in ideal conditions. The results presented in Fig. 4.4(a) indicated that the proposed antenna operated with a simulated -10 dB impedance bandwidth of 120 MHz at 1.575 GHz. This translates into an equivalent fractional bandwidth of 7.6%. Meanwhile at 2.45 GHz, results indicated a simulated bandwidth of 136 MHz, which is about 5.5% of equivalent fractional bandwidth.

During measurements, the proposed structure is validated to operate with 185 MHz of bandwidth at 2.45 GHz and 440 MHz of bandwidth at 1.575 GHz. Their equivalent fractional bandwidth is 27% and 7.5% at 2.45 GHz and 1.575 GHz, respectively. In free space, dual-polarization is already evident from both the simulations and measurements by observing its axial ratio in the 1.575 GHz band. Results in Fig. 3.3(b) showed that the proposed antenna features a 10.3% of circular polarization axial ratio bandwidth when simulated, and 9% when measured in this band. Besides that, simulation and measurement results also indicated a linear polarization behavior in the 2.45 GHz band. Moreover, the movement of surface current in a circular direction in the proposed antenna (at 1.575 GHz) can be observed in Fig. 4.3(d). Also, the operation of the AMC plane at 2.45 GHz resulted in a realized gain of about 2 dBic at 1.575 GHz and 1.9 dBi at 2.45 GHz. Figure 4.5(a) and (b) reports the measured and simulated realized gain across the lower and upper frequency ranges and results are in good agreement with the simulations. The simulated radiation efficiency of the proposed antenna with the AMC plane at 1.575 GHz and 2.45 GHz are 73.6% and 83%, respectively. The simulated radiation efficiency of the proposed design without the AMC plane at 1.575 GHz and 2.45 GHz are 48% and 45%, respectively. Adding an AMC plane enhances the overall performance of the antenna.

It is foreseen that the antenna will suffer physical deformation during operation due
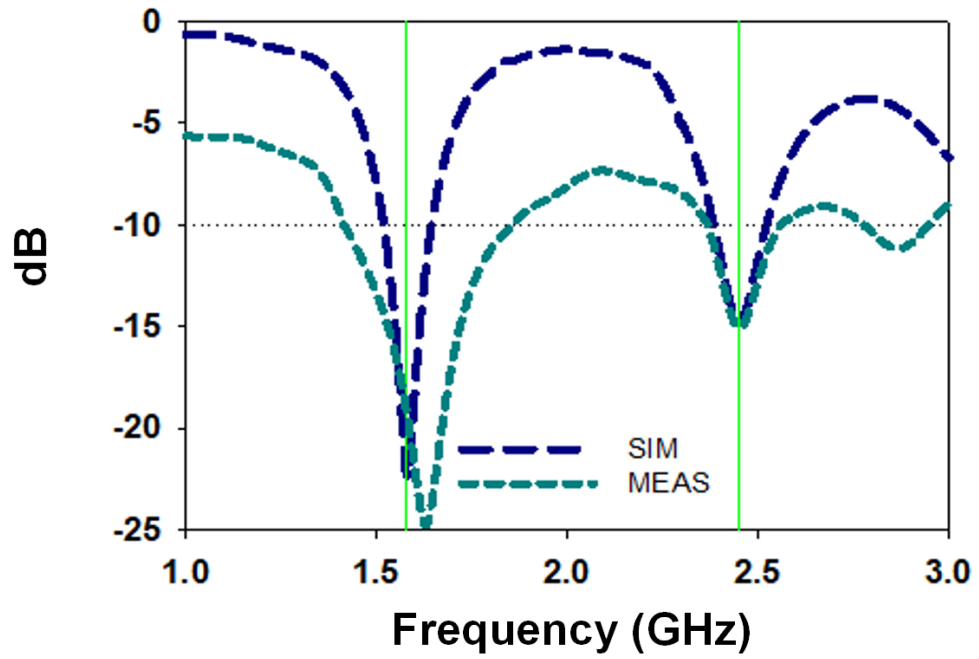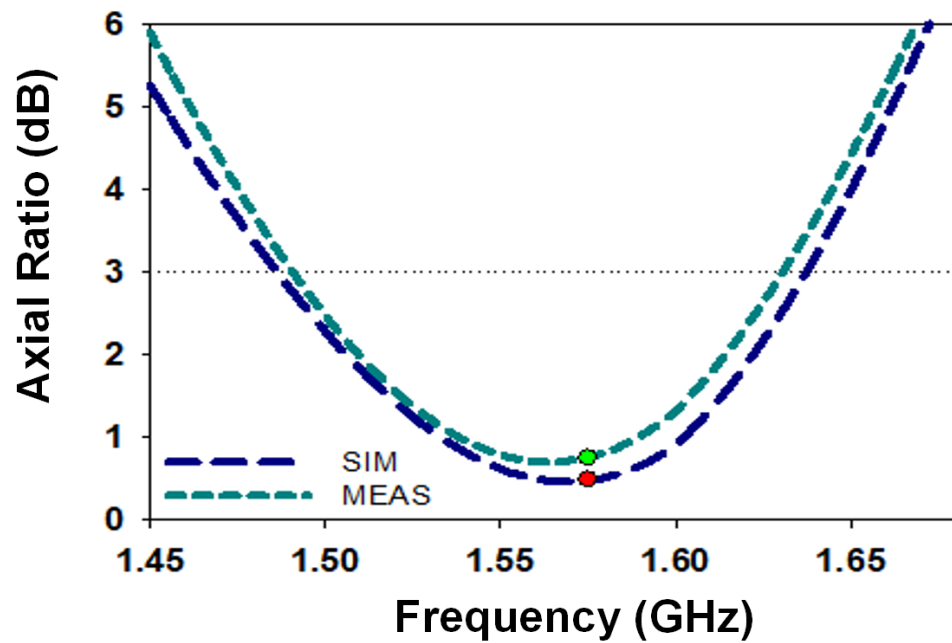
Figure 4.4: Simulated and measured results of the antenna performance: (a) reflection coefficient; and (b) axial ratio [21].

to the presence flexible textile materials. Thus, this section is dedicated to study the effects of the antenna independently when bent in free space using simulations
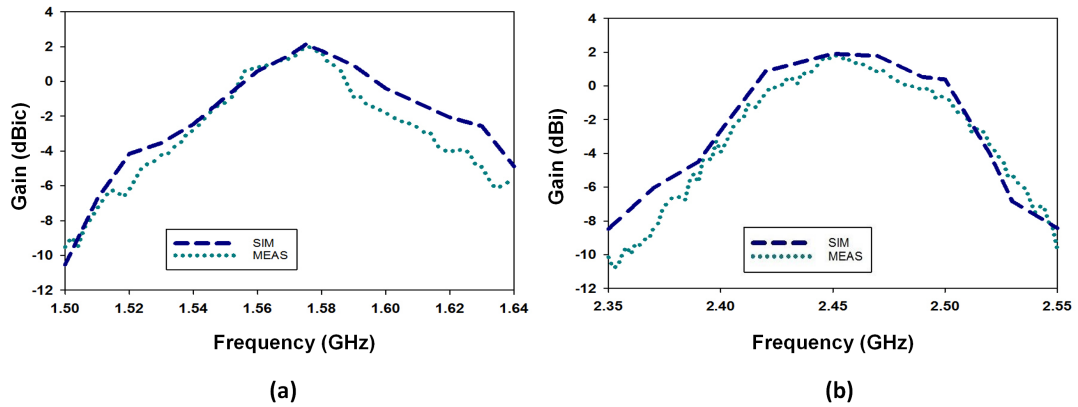
Figure 4.5: Simulated and measured realized gain across two frequency ranges when the antenna is in free space (a) lower band frequency (1.575 GHz) and (b) upper band frequency (2.45 GHz) [21].

and measurements. this is followed by the investigation of its performance in the following section when bent and placed over a detailed human voxel model.

The first investigation is performed by conformally bending the proposed antenna around a cylinder (air) with a radius of r = 60 mm at the x- and y-axes, as illustrated in Fig. 4.6. This is done to simulate its placement when worn on the upper arm. The simulated and measured reflection coefficients of the proposed antenna when evaluated under bending in free space are presented in Fig. 4.7. Simulations indicated that the antenna bending at the x-axis slightly increased its bandwidth from 120 MHz to 160 MHz when compared to its planar form in the 1.575 GHz band. Meanwhile, bandwidth in the 2.45 GHz band is also increased from 136 MHz to 190 MHz when compared to its planar representation. The axial ratio of the antenna is
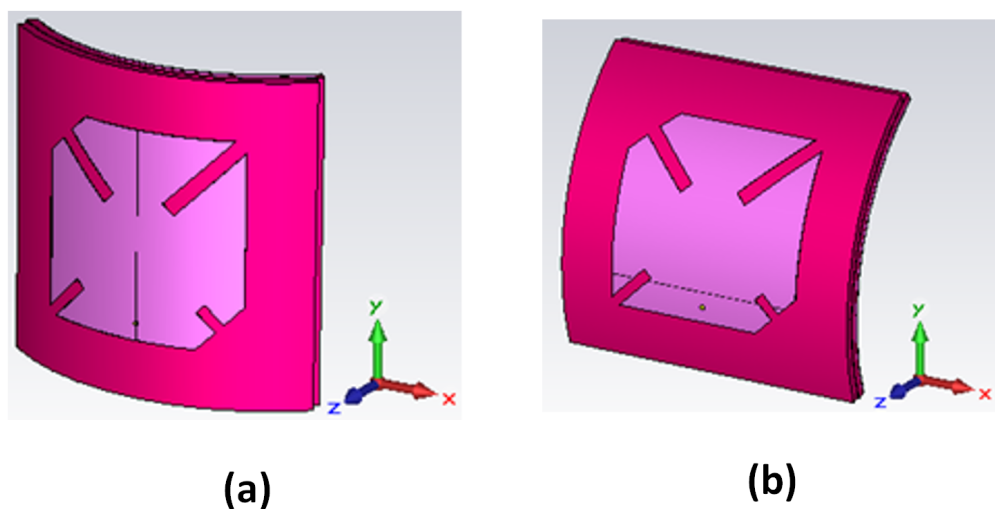
Figure 4.6: The antenna when bent at the (a) y-axis and (b) x-axis [21].

found to be 2.2 dB when the antenna is bent to 45°. The axial ratio in this bent condition is approximately 1.2 dB higher than in its planar form (see Fig. 3.3(b)). Nonetheless, the AR is still below 3 dB and the antenna maintains CP operation at 1.575 GHz.

(a)

(b)
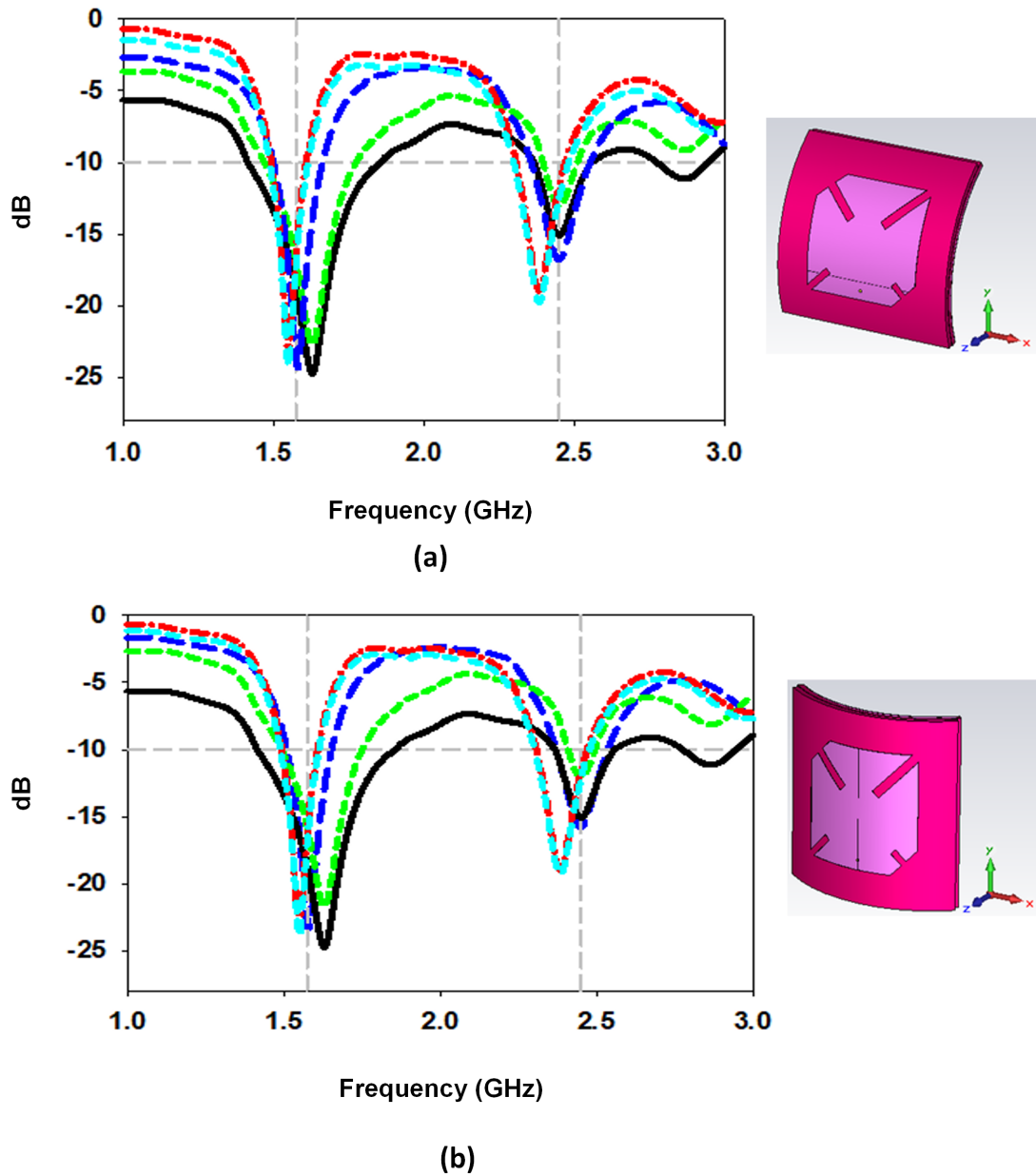
Figure 4.7: Antenna reflection coefficients when bent at the (a) x-axis and (b) y-axis. Legend: measured planar antenna (solid black line); bent with r = 60 mm (simulated) (long dashed blue line); bent with r = 60 mm (measured) (short dashed green line); bent on shoulder (dashed-dot red line); bent on upper arm (short-short cyan line) [21].

On the contrary, the antenna bent at the y-axis increased the bandwidth in the 1.575 GHz band to 140 MHz in simulations, and to 164 MHz in the 2.45 GHz
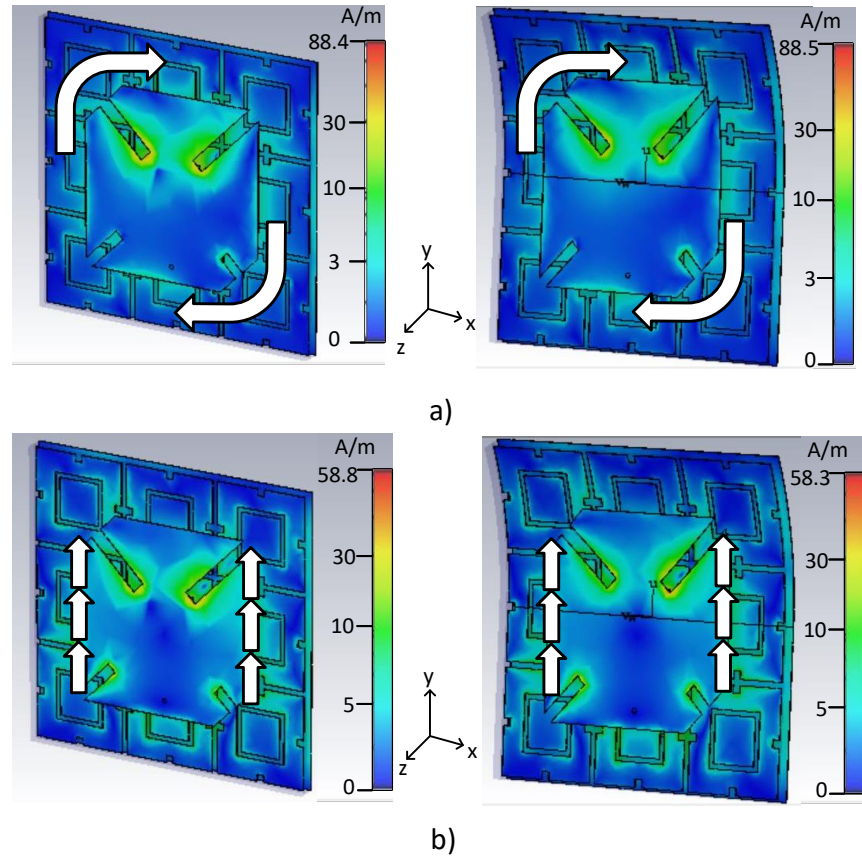
Figure 4.8: Amplitude of surface current distribution for planar and bent form at (a) 1.575 GHz and (b) 2.45 GHz [21]. The arrow in white shows the direction of the currents.

band. Meanwhile, when the antenna structure is bent at the x-axis, its bandwidth is decreased to 300 MHz in the 1.575 GHz band. In comparison, measurements in planar form resulted in a bandwidth of 440 MHz. In the WLAN/WBAN band, the bandwidth is reduced from 185 MHz (in planar form) to 110 MHz when the antenna is bent at the x-axis. On the other hand, bending of the proposed antenna at the y-axis indicated a bandwidth reduction in both 1.575 GHz band (to 255 MHz) and 2.45 GHz band (to 85 MHz).

Generally, the antenna performance considering all bent configurations are almost identical to its performance in planar form, with slight fluctuations in reflection coefficient and bandwidth compared (see Fig. 4.7). This is in agreement with the findings from [25], where the smaller bending radius resulted in a shorter resonant length in comparison with its planar form. When the antenna is bent at the y-axis, a relatively larger bandwidth reduction is exhibited in comparison to the x-axis bending. This observation is aligned with the findings in [25], where the existence of the AMC plane alleviated the effects of the bending. The results observed after

bending is similar to the findings in [25], where the EBG was used as a substrate and due to the presence of this EBG plane, the bending has a minimal effect on the antenna performance. Also, an EBG and AMC do not offer the same physical response in support of the antenna operation for the intended textile application, but yet can also be made using grounded dielectrics, and textile materials as in this work, and for multiband operation as in [26].

To analyze further the performance of the antenna in its bent form (approx. 30°), the surface current distribution was studied. Figure 4.8 illustrates the surface current distribution of the antenna in planar and its bent form at the two resonant frequencies. The amplitude of the surface current in planar and bent form at 1.575 GHz are 88.4 A/m and 88.5 A/m, respectively. Likewise, at 2.45 GHz they are 58.7 A/m and 58.3 A/m, respectively. This shows that the antenna still maintian circular polarization and have no effect on the movement of surface current even when bent.

Regardless of these minor changes in the surface current distributions and observed maximums (see Fig. 4.8), satisfactory performance of the antenna is observed under both bent conditions and when operating in free-space. To quantify the impact of the AMC plane in decreasing backwards radiation for these scenarios, the front-to-back ratios (FBRs) are assessed both in terms of simulations and measurements at 1.575 GHz and 2.45 GHz (see Table 4.2). The simulated FBR of the antenna in planar form is initially 19.6 dB (at 1.575 GHz) and 17.4 dB (at 2.45 GHz). The antenna FBR is then reduced to 15.9 dB at 1.575 GHz and to 10 dB at 2.45 GHz when bent at the x-axis. Meanwhile, the antennas simulated FBR also decreased to 11.6 dB at 1.575 GHz and 10.9 dB at 2.45 GHz when bent at the y-axis.

Measurements when the antenna is bent at the x-axis produced FBR levels of 12.89 dB at 1.575 GHz, and 15.51 dB at 2.45 GHz. In contrast, the measured FBR of the planar antenna in free space is 9.64 dB. Meanwhile, the measured FBR when bent at the y-axis are less affected, with FBR degradations to 14.83 dB (at 1.575 GHz) and 9.48 dB (at 2.45 GHz). On the other hand, the simulated and measured radiation patterns of the antenna when bent at the two directions are illustrated in Fig. 4.9. The meaurement setup and related background theory for circular polarized antennas was reported in [27, 28]. As intended, the antenna radiated towards the broadside with low backlobes, minimizing radiation towards the human user. The simulated FBR of the antenna in planar form at both frequencies are summarized in

Table 4.2: Simulations and measurement of the antenna and the front-back-ratio with and without the AMC Plane

Frequency (GHz)	Condition	FBR (dB) (Sims)	FBR (dB) (Meas)
1.575 GHz	Planar with AMC	19.6	16.7
	Bent with AMC	10.2	11.0
	Planar without AMC	13.4	-
	Bent without AMC	9.1	-
2.45 GHz	Planar with AMC	17.4	12.0
	Bent with AMC	10.0	9.88
	Planar without AMC	11.3	-
	Bent without AMC	11.0	-

Table 4.2 when antenna is with and without the AMC plane. It can be observed that the FBR is lower for the antenna structure without the AMC plane as compared to the proposed antenna structure in planar and bent form. These results suggest that the AMC plane does indeed reduce backward radiation.

4.3.2   Performance On-Body (Bent)

Next, the on-body performance of the bent antenna in proximity of the body is further validated using a voxel model. Simulations are performed using the bent antenna placed at a 10 mm distance over the truncated shoulder and upper arm of a Hugo voxel model (using $1 \times 1 \times 1$ mm^3 mesh resolution) to reduce computational resources. The 10 mm distance is determined based on an average clothes-to-body spacing which varies with time and users movements, assuming that the clothes worn is with average tightness. For on-body measurement a commercial mannequin was used which was made from polystyrene material of dielectric constant 2.4. For simulations and measurements, the antenna was placed at the upper arm (UH) and shoulder (SH) of the human body. In these studies, the shoulder has a radial geometry and was chosen to achieve bending of the antenna along the x-axis acting as if the antenna is placed on a cylindrical object. Also, the bending in the y-axis was achieved by placing the antenna at the upper arm of the human body.

Simulations are performed using the bent antenna placed at a 10 mm distance over
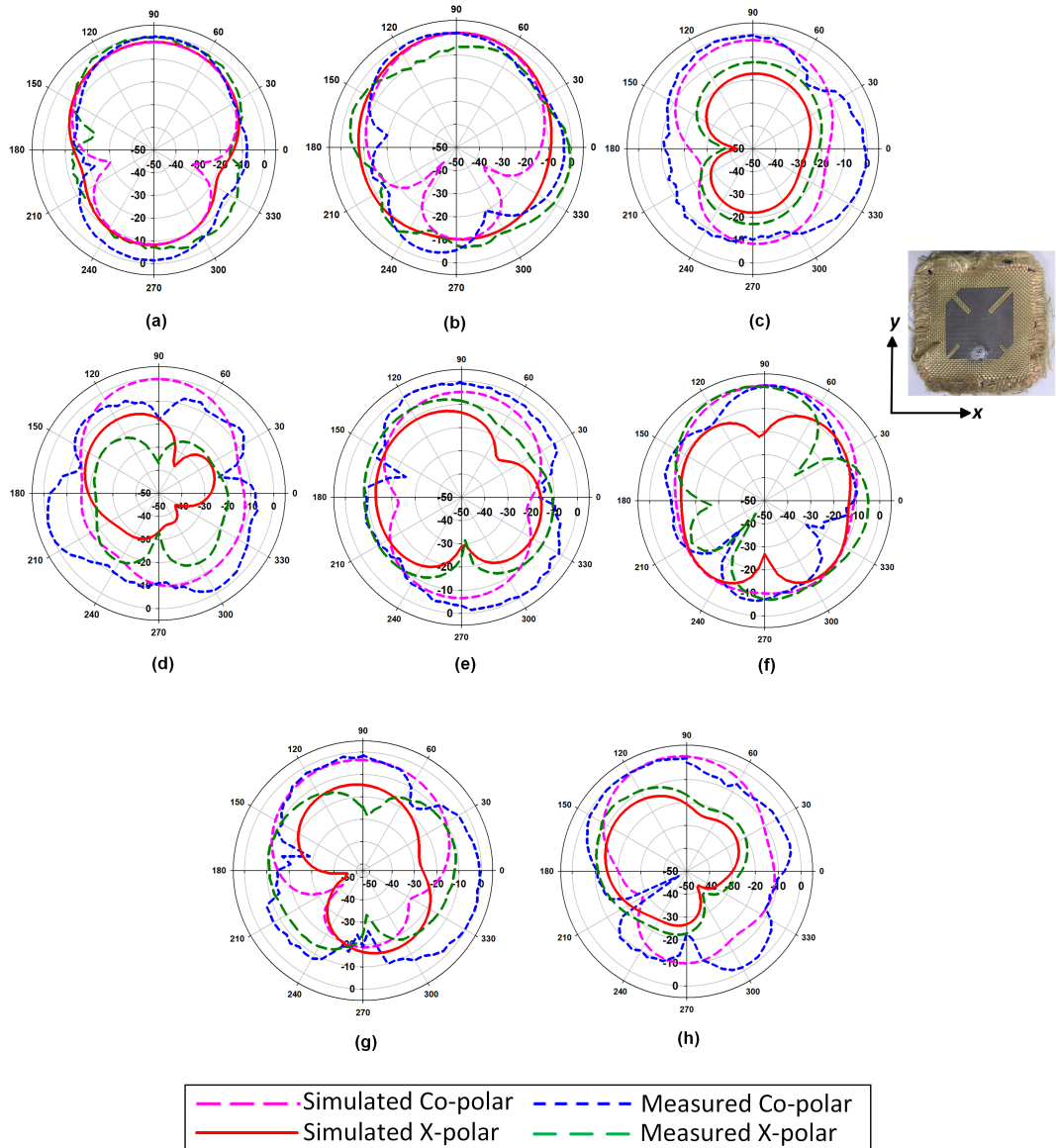
Figure 4.9: Simulated and measured radiation patterns of the proposed antenna when bent at the (a) x-axis (xz-plane) at 1.575 GHz, (b) x-axis (xz-plane at 2.45 GHz), (c) x-axis (yz-plane) at 1.575 GHz, (d) x-axis (yz-plane) at 2.45 GHz, (e) the y-axis (xz-plane) at 1.575 GHz, (f) the y-axis (xz-plane) at 2.45 GHz, (g) y-axis (yz-plane) at 1.575 GHz and (h) y-axis (yz-plane) at 2.45 GHz [21].

the truncated shoulder and upper arm of a Hugo voxel model (using $1 \times 1 \times 1$ mm^3 mesh resolution) to reduce computational resources. The 10 mm distance is determined based on an average clothes-to-body spacing which varies with time and users movements, assuming that the clothes worn is with average tightness [29]. Evaluation when the antenna is bent at the x-axis over the upper arm altered the bandwidth to 120 MHz in the 1.575 GHz band and 172 MHz in the 2.45 GHz band. Conversely, bending at the y-axis produced a bandwidth of 120 MHz in the 1.575
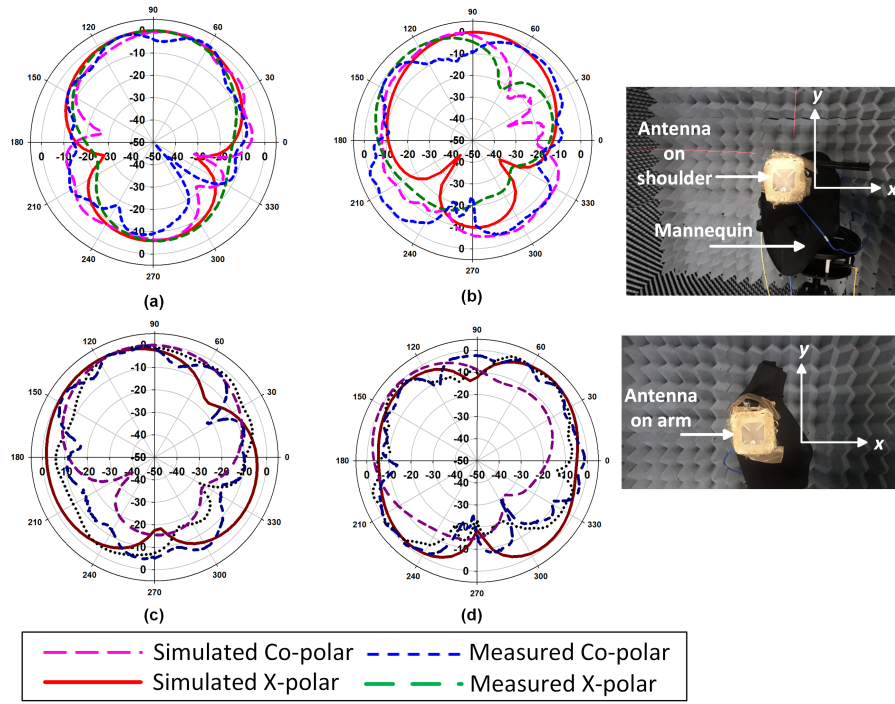
Figure 4.10: Simulated and measured radiation patterns at the yz-plane when the antenna is placed on the upper arm and shoulder at (a) 1.575 GHz bent at the x-axis, (b) 2.45 GHz bent at the x-axis, (c) 1.575 GHz bent at the y-axis and (d) 2.45 GHz bent at the y-axis [21].

GHz band and 172 MHz in the 2.45 GHz band. When simulated over the shoulder and bent at the x-axis, the bandwidth in the 1.575 GHz band decreased to 112 MHz and to 156 MHz in the 2.45 GHz band. On the contrary, y-axis bending of the antenna did not affect the bandwidths, as a similar 112 MHz of bandwidth is shown in the 1.575 GHz band, and 156 MHz is produced in the 2.45 GHz band. It is also concluded that the antenna can be operated when bent on body at the y-axis, as this increased bandwidths in both the 1.575 GHz and 2.45 GHz bands. These results are illustrated in Fig. 4.7.

On the other hand, simulations for FBR indicated levels of 16.03 dB when the antenna is bent at the x-axis on the upper arm at 1.575 GHz, whereas this is reduced to 10.3 dB at 2.45 GHz. Evaluation of the antenna bent at the y-axis when placed on the upper arm showed FBR values of 15.3 dB (at 1.575 GHz) and 11.2 dB (at 2.45 GHz). When bent on the shoulder at the x-axis, the simulated FBR for the antenna is 11.6 dB and 23.3 dB at 1.575 GHz and 2.45 GHz, respectively. When bent over the shoulder at the y-axis, an increased FBR at both frequencies can be observed, which is 15.4 dB (at 1.575 GHz) and 26.1 dB (at 2.45 GHz).

In general, the antenna operated on the body when bent at both the x- and y-axes

and resulted in an increment of FBR compared to the antenna in free space, as illustrated in Fig. 4.10. There are some minor discrepancies in Figs. 4.10(b) and (d) between the simulated and measured results. This is due to the probe and SMA feed used for the antenna, making it rather difficult for uniform bending on the mannequin. Regardless, the antenna still maintains its performance and front back ratio is in close agreement with the simulations.

Notice also that while the antenna impedance bandwidths when bent at both axes and evaluated near both locations (upper arm and shoulder) are similar, significant improvements in FBR are observed when the antenna is operating at 2.45 GHz. This is expected from the shielding provided by the AMC plane backing which operated most efficiently in this particular band.

The final assessment for the proposed antenna is performed in terms of safety. It is based on the standards set by the International Commission on Non-Ionizing Radiation Protection (ICNIRP) [3], and is regulated at a maximum of 2 W/kg averaged over 10 g of tissue. Assessments were performed using CST with a 0.5 W_{rms} input power fed into the antennas located at the same distance over the same voxel models of the upper arm (UA) and shoulder (SH). When bent at the x-axis and placed on the upper arm, the antenna configuration produced SAR values of 0.111 W/kg at 1.575 GHz and 0.111 W/kg at 2.45 GHz. Meanwhile, when bent at the y-axis on placed in proximity of the upper arm, this setup resulted in 0.086 W/kg and 0.0877 W/kg of SAR at 1.575 GHz and 2.45 GHz, respectively.

When bent at the x-axis and placed on the shoulder, the resulting SAR value of the antenna is 0.0983 W/kg at 1.575 GHz and 0.0747 W/kg at 2.45 GHz. The antenna bent at the y-axis and located near the shoulder resulted in 0.0449 W/kg and 0.0573 W/kg of SAR at 1.575 GHz and 2.45 GHz, respectively. These values indicate safe operation in the vicinity of the body as they are well below the regulated SAR limits which were simulated to be 0.134 W/kg at 1.575 GHz and 0.160 W/kg at 2.45 GHz. Also, these results suggest that SAR values without the AMC plane, at both frequencies, are higher than the values observed for the antenna with the AMC plane. It can also be observed that the antenna when bent at both axes and assessed near the shoulder produced slightly lower values compared to the SAR values produced when placed in proximity of the upper arm. This can be due to the composition of the shoulder area which consists of more skin and bone in comparison

to the upper arm which contain more absorptive muscle and fat tissues.

Table 4.3: Summary of Bent On-Body Evaluations

Freq. (GHz)	Conditions (Sims.)	SAR (W/kg) UA	SAR (W/kg) SH	FBR (dB) UA	FBR (dB) SH	Bandwidth (MHz) UA	Bandwidth (MHz) SH
Lower band	x-axis	0.111	0.098	16.0	11.6	120	112
frequency	y-axis	0.086	0.045	15.3	15.4	120	112
Upper band	x-axis	0.098	0.075	10.3	23.3	172	156
frequency	y-axis	0.088	0.057	11.2	26.1	172	156

A summary of the on-body bandwidth, FBR and SAR at both frequencies is provided in Table 4.3. The simulated and measured radiation patterns of the bent antennas at 1.575 GHz and 2.45 GHz when located on-body are shown in Fig. 4.10(a-d). It can be observed that the antenna radiated towards the forward direction with low backlobes. A minor discrepancy can be observed between simulation and measurements Fig. 4.10(b) due to measurement complexities, for example, while doing on-body measurements, the probe was found to be not entirely bent as compared simulations and has led to the measurement inaccuracies. However, the proposed antenna still maintained radiation in forwards direction with low back lobes. Also, measured cross-polarization levels are below -20 dB in each case.

4.4   Summary

A wearable textile antenna with dual-band and dual-sense characteristics is designed, simulated and fabricated for location tracking purposes, using GPS in the outdoor and WLAN in indoor environments. The dual-band originated from a square patch before being integrated with slits and truncated corners to operate in the 1.575 GHz band (with circular polarization) and in the 2.45 GHz band (with linear polarization). To alleviate body coupling in wearable antennas, an AMC plane with a 3 × 3 array of unit cells is integrated behind the antenna. The AMC unit cells are designed based on a square patch with rectangular slits on each side, and a square

ring for operation at 2.45 GHz.

The generated fractional impedance bandwidth in these two bands is 27% and 7.5%, respectively, with a 9% 3 dB axial ratio bandwidth in the 1.575 GHz band. Meanwhile, the measured realized gain at 1.575 GHz is 1.98 dBic, and is 1.94 dBi at 2.45 GHz. Further investigation of the antenna under bending indicated its better suitability for operation when bent at the y-axis on the body. The antenna integrated with the AMC plane provided SAR values which are below 0.12 W/kg for placement on the upper arm and shoulder of a human body. The performance of the antenna makes it suitable for wearbale applications.

References

[1] S. M. Salleh, M. Jusoh, A. H. Ismail, M. R. Kamarudin, P. Nobles, M. K. A. Rahim, T. Sabapathy, M. N. Osman, M. I. Jais, and P. J. Soh, "Textile antenna with simultaneous frequency and polarization reconfiguration for WBAN," *IEEE Access*, vol. 6, pp. 7350–7358, 2018.

[2] N. F. M. Aun, P. J. Soh, A. A. Al-Hadi, M. F. Jamlos, G. A. E. Vandenbosch, and D. Schreurs, "Revolutionizing wearables for 5G: 5G technologies: Recent developments and future perspectives for wearable devices and antennas," *IEEE Microwave Magazine*, vol. 18, no. 3, pp. 108–124, 2017.

[3] I. E. Commission *et al.*, "Human exposure to radio frequency fields from hand-held and body-mounted wireless communication devices: human models, instrumentation, and procedures to determine the specific absorption rate (SAR) for hand-held devices used in the close proximity to the ear (frequency range of 300 MHz to 3 GHz). Geneva: IEC," *International Standard*, vol. 62209, 2005.

[4] G. Z. Rafi, M. Mohajer, A. Malarky, P. Mousavi, and S. Safavi-Naeini, "Low-profile integrated microstrip antenna for GPS-DSRC application," *IEEE Antennas and Wireless Propagation Letters*, vol. 8, pp. 44–48, 2009.

[5] S. Ma and J. Row, "Design of single-feed dual-frequency patch antenna for GPS and WLAN applications," *IEEE Transactions on Antennas and Propagation*, vol. 59, no. 9, pp. 3433–3436, 2011.

[6] P. Sharma and K. Gupta, "Analysis and optimized design of single feed circularly polarized microstrip antennas," *IEEE Transactions on Antennas and Propagation*, vol. 31, no. 6, pp. 949–955, 1983.

[7] Nasimuddin, X. Qing, and Z. N. Chen, "Compact asymmetric-slit microstrip antennas for circular polarization," *IEEE Transactions on Antennas and Prop-*

agation, vol. 59, no. 1, pp. 285–288, 2011.

[8] Wen-Shyang Chen, Chun-Kun Wu, and Kin-Lu Wong, "Novel compact circularly polarized square microstrip antenna," *IEEE Transactions on Antennas and Propagation*, vol. 49, no. 3, pp. 340–342, 2001.

[9] R. P. Dwivedi, M. Z. Khan, and U. K. Kommuri, "UWB circular cross slot amc design for radiation improvement of UWB antenna," *AEU-International Journal of Electronics and Communications*, vol. 117, p. 153092, 2020.

[10] J. Lin, Z. Qian, W. Cao, S. Shi, Q. Wang, and W. Zhong, "A low-profile dual-band dual-mode and dual-polarized antenna based on amc," *IEEE Antennas and Wireless Propagation Letters*, vol. 16, pp. 2473–2476, 2017.

[11] M. El Atrash, M. A. Abdalla, and H. M. Elhennawy, "A wearable dual-band low profile high gain low sar antenna amc-backed for wban applications," *IEEE Transactions on Antennas and Propagation*, vol. 67, no. 10, pp. 6378–6388, 2019.

[12] N. Hussain, M. Jeong, A. Abbas, T. Kim, and N. Kim, "A metasurface-based low-profile wideband circularly polarized patch antenna for 5g millimeter-wave systems," *IEEE Access*, vol. 8, pp. 22 127–22 135, 2020.

[13] N. Hussain, M. Jeong, J. Park, and N. Kim, "A broadband circularly polarized fabry-perot resonant antenna using a single-layered prs for 5g mimo applications," *IEEE Access*, vol. 7, pp. 42 897–42 907, 2019.

[14] W. Cao, B. Zhang, A. Liu, T. Yu, D. Guo, and Y. Wei, "Gain enhancement for broadband periodic endfire antenna by using split-ring resonator structures," *IEEE Transactions on Antennas and Propagation*, vol. 60, no. 7, pp. 3513–3516, 2012.

[15] T. Yue, Z. H. Jiang, and D. H. Werner, "A compact metasurface-enabled dual-band dual-circularly polarized antenna loaded with complementary split ring resonators," *IEEE Transactions on Antennas and Propagation*, vol. 67, no. 2, pp. 794–803, 2019.

[16] K. Agarwal, Nasimuddin, and A. Alphones, "Wideband circularly polarized AMC reflector backed aperture antenna," *IEEE Transactions on Antennas and Propagation*, vol. 61, no. 3, pp. 1456–1461, 2013.

[17] J. Chen, K. Tong, A. Al-Armaghany, and J. Wang, "A dual-band dual-polarization slot patch antenna for GPS and Wi-Fi applications," *IEEE Antennas and Wireless Propagation Letters*, vol. 15, pp. 406–409, 2016.

[18] M. E. de Cos, F. L. Heras, and M. Franco, "Design of planar artificial magnetic conductor ground plane using frequency-selective surfaces for frequencies below 1 GHz," *IEEE Antennas and Wireless Propagation Letters*, vol. 8, pp. 951–954, 2009.

[19] R. Dewan, M. Rahim, M. Hamid, M. Yusoff, N. Samsuri, N. Murad, and K. Kamardin, "Artificial magnetic conductor for various antenna applications: An overview," *International Journal of RF and Microwave Computer-Aided Engineering*, vol. 27, no. 6, p. e21105, 2017.

[20] E. F. N. M. Hussin, P. J. Soh, A. A. Al-Hadi, M. F. Jamlos, M. N. Ramli, H. Lago, N. Kuster, and S. K. Podilchak, "Dual-band dual-polarized textile antenna for location tracking in AAL," in *12th European Conference on Antennas and Propagation (EuCAP 2018)*, 2018, pp. 1–4.

[21] R. Joshi, E. F. N. M. Hussin, P. J. Soh, M. F. Jamlos, H. Lago, A. A. Al-Hadi, and S. K. Podilchak, "Dual-band, dual-sense textile antenna with amc backing for localization using GPS and WBAN/WLAN," *IEEE Access*, vol. 8, pp. 89 468–89 478, 2020.

[22] S. Maci and G. B. Gentili, "Dual-frequency patch antennas," *IEEE Antennas and Propagation Magazine*, vol. 39, no. 6, pp. 13–20, 1997.

[23] C. A. Balanis, *Antenna theory: analysis and design.* John wiley & sons, 2016.

[24] R. Garg, P. Bhartia, I. J. Bahl, and A. Ittipiboon, *Microstrip antenna design handbook.* Artech house, 2001.

[25] P. Salonen and Y. Rahimat-Samii, "Textile antennas: effects of antenna bending on input matching and impedance bandwidth," *IEEE Aerospace and Electronic Systems Magazine*, vol. 22, no. 3, pp. 10–14, 2007.

[26] G. Goussetis, A. P. Feresidis, and J. C. Vardaxoglou, "Tailoring the AMC and EBG characteristics of periodic metallic arrays printed on grounded dielectric substrate," *IEEE Transactions on Antennas and Propagation*, vol. 54, no. 1, pp. 82–89, 2006.

[27] W. L. Stutzman, *Polarization in electromagnetic systems*. Artech House, 2018.

[28] B. Y. Toh, R. Cahill, and V. F. Fusco, "Understanding and measuring circular polarization," *IEEE Transactions on Education*, vol. 46, no. 3, pp. 313–318, 2003.

[29] K. Ito, C. Lin, H. Lin, Z. Chen, D. Liu, H. Nakano, X. Qing, and T. Zwick, "Evaluation of wearable and implantable antennas with human phantoms," *Handbook of antenna technologies. Springer, Singapore*, pp. 1–24, 2015.

Chapter 5

Cavity Model Analysis of the Conventional Patch and Folded-Shorted Patch (FSP) Antenna

In this chapter a cavity model analysis on multilayer folded-shorted patch (FSP) antenna for the TM_{010} [1] and TM_{001} [1] operating modes have been presented. Through this analysis, for the FSP, the electric field configuration of the dominant mode (TM_{010}) will be analyzed and then will be extended for higher order mode (TM_{001}). The results of FSP are compared with conventional patch antenna. It is worth mentioning that in this chapter, a detailed study on the theory of cavity model analysis for the conventional patch antenna is presented [1] and then extend for FSP antenna. To best of authors knowledge, the cavity model analysis is not avalaiable in the literature for multilayer FSP structures. This chapter is organized as follows. In Section 5.1, background theory on rectangular patch antenna (RPA) and different methods that are used for analysis of patches are described. In Section 5.2, cavity model analysis of conventional patch antenna is presented. In Section 5.3, cavity model analysis of the FSP antenna is described. A comparison on the fields radiated by both antennas are described in Section 5.4 while a summary of the chapter is dicussed in Section 5.5.

5.1   Background Theory

The study focus on the rectangular patch antenna (RPA) and similar types of structures. Generally, the RPA consists of the metallic patch and electrically thin or thick grounded dielectric block [2]. RPA′s are one of the most popular antennas due to lightweight, low profile, low cost, mechanically sturdy, and are versatile with respect to polarization, frequency, beam patterns, and impedances. Nonetheless, RPA comes with some disadvatages such as narrow bandwidth, low power, and unwanted spurious feed radiation. Over the last decade, many methods were introduced to enhance the bandwidth of the antenna such as the introduction of a slot in the patch, using metasurfaces and parasitic elements to name a few [3–5]. RPA is fed either by a microstrip[1] or by coaxial probe[2].

In literature, there are many methods mentioned to analyze the RPA and the most popular methods are transmission line model analysis, cavity model analysis, and full-wave analysis using simulations. The transmission line model of analysis is one of the simple ways to scrutinize the behavior of RPA and it provides a good physical insight for the antenna [1,2]. Nonetheless, the transmission line model lacks in terms of accuracy and model coupling as compared to other model analysis [1]. In comparison, the cavity model analysis of an antenna produces a more accurate solution [6]. The complex solution in the cavity model analysis can be simplified by using mathematical tools such as MATLAB (R2017b) or Mathematica. The full-wave simulation model provides more accurate analysis when modeled properly as compared to the transmission line model and cavity model analysis. These models can be used for a single element, finite and infinite arrays for coupling analysis and for stacked elements. Nowadays, the most common software that uses full-wave simulation models are CST Studio Suite and Ansys HFSS.

The cavity model analysis allows the antenna engineer to estimate the operational frequency, beam pattern shape, and directivity prior to simulation and fabrication. This will further reduce the overall optimization time. The mathematical tool will be developed to analyze the radiation characteristics of a rectangular patch antenna.

---

[1]A microstrip line is a conducting strip with a smaller width than a patch and is attached to the radiating patch.

[2]Coaxial feedline is the method of feeding where the inner conductor is attached to the radiationg patch and outer conductor is attached to the ground plane.

The concept will be demonstrated by examples and illustrations. Due to mathematical complexities, the observations will be restricted to the far-field configuration and directivity of the antenna. The emphasis will be placed on the techniques that use fields on or in the vicinity of the antenna structure, and one such technique is commonly known as Field Equivalence Principle [1].

5.1.0.1   Radiation Equation of the Antenna

In [1], it is mentioned that there are two ways to compute the radiated electric ($\mathbf{E}$) and magnetic ($\mathbf{H}$) fields. The procedures are as follows: (1) to derive the radiated fields directly by integrating source current densities that are electric ($\mathbf{J}$) and magnetic ($\mathbf{M}$) current densities, and (2) to integrate $\mathbf{J}$ and $\mathbf{M}$ to derive vector potentials $\mathbf{A}$ and $\mathbf{F}$ and then apply derivation to the vector potentials to get $\mathbf{E}$ and $\mathbf{H}$ fields. To summarize, the equations which are developed earlier in the literature are used to find the $\mathbf{E}$ and $\mathbf{H}$ fields generated by the current source densities. The inhomogeneous solution of $\mathbf{A}$ and $\mathbf{F}$ depends on $\mathbf{J}$ and $\mathbf{M}$, respectively are shown in equations (5.1.1) and (5.1.2) (From [1], Chapter 3, Equations (3.27)-(3.28)).

$$\mathbf{A} = \frac{\mu}{4\pi} \iiint_v \frac{\mathbf{J}e^{-jkR}}{R} dv' \tag{5.1.1}$$

$$\mathbf{F} = \frac{\epsilon}{4\pi} \iiint_v \frac{\mathbf{M}e^{-jkr}}{R} dv' \tag{5.1.2}$$

Equations (5.1.1) and (5.1.2), $\mathbf{R}$ is the distance from any point in the source to the observation point and $k = \omega\sqrt{\mu\epsilon}$ [1]. In [7], these radiation equations are simiplified for the transverse electric (TE) and transverse magnetic (TM) modes for rectangular cordinate system. Also, equations were derived for the transverse electromagnetic (TEM) mode for rectangular and cylindrical coordinates.

Equations (5.1.1) and (5.1.2) can be further simplified by using R. For example, $\mathbf{R} \approx r - r'\cos\psi$ [7] and $R \approx r$ [7] for phase variations and amplitude variations, respectively where ψ is the angle between $\mathbf{r}$ and $\mathbf{r}'$ [7]. Equations (5.1.3), (5.1.4), (5.1.5) and (5.1.6) shows the simplified values of $\mathbf{A}$, $\mathbf{N}$, $\mathbf{F}$ and $\mathbf{L}$, respectively after substituting value of $\mathbf{R}$ (From [1], Chapter 12, Equations (12-6) - (12.7a)).

$$\mathbf{A} = \frac{\mu}{4\pi} \iint_s \frac{\mathbf{J_s} e^{-jkR}}{R} ds' \approx \frac{\mu e^{-jkr}}{4\pi R} \mathbf{N} \tag{5.1.3}$$

$$\mathbf{N} = \iint_s \mathbf{J_s} e^{-jkr' \cos \psi} ds' \tag{5.1.4}$$

$$\mathbf{F} = \frac{\epsilon}{4\pi} \iint_s \frac{\mathbf{M_s} e^{-jkR}}{R} ds' \approx \frac{\epsilon e^{-jkr}}{4\pi R} \mathbf{L} \tag{5.1.5}$$

$$\mathbf{L} = \iint_s \mathbf{M_s} e^{jkr' \cos \psi} ds' \tag{5.1.6}$$

5.1.0.2 Far-Field Radiation

Spherical coordinate system is used for the far-field radiation of the antenna. We know that, sperical coordinate system have three components that is r, θ and ϕ. Vector potential A can be expressed in terms of spherical coordinate and can be further simplified to a general form as shown in (5.1.7) [7]. $\hat{\mathbf{a}}_\mathbf{r}$, $\hat{\mathbf{a}}_\theta$ and $\hat{\mathbf{a}}_\phi$ are vectors associated with each coordinates.

$$\mathbf{A} = \hat{\mathbf{a}}_\mathbf{r} A_r(r, \theta, \phi) + \hat{\mathbf{a}}_\theta A_\theta(r, \theta, \phi) + \hat{\mathbf{a}}_\phi A_\phi(r, \theta, \phi) \tag{5.1.7}$$

In [7], it is derived that $\mathbf{E}$ and $\mathbf{H}$ fields have θ and ϕ components. Equations (5.1.8) and (5.1.9) shows the value of electric and magnetic fields for θ and ϕ components (From [7], Chapter 6, Equations (6-101a) - (6.101b)).

$$E_r \approx 0$$

$$E_\theta \approx -j\omega A_\theta \tag{5.1.8}$$

$$E_\phi \approx -j\omega A_\phi$$

$$H_r \approx 0$$

$$H_\theta \approx +j\frac{\omega}{\eta}A_\phi \tag{5.1.9}$$

$$H_\phi \approx -j\frac{\omega}{\eta}A_\theta$$

Now, θ and ϕ component of $\mathbf{E}$ and $\mathbf{H}$ field can be written as follows (From [7], Chapter 6, Equations (6-117a) - (6.117d)):

$$(E_A)_\theta \approx -j\omega A_\theta$$

$$\tag{5.1.10}$$

$$(E_A)_\phi \approx -j\omega A_\phi$$

$$(H_F)_\theta \approx -j\omega F_\theta$$

$$\tag{5.1.11}$$

$$(H_F)_\phi \approx -j\omega F_\phi$$

In (5.1.10) and (5.1.11) subscripts A and F are fields generated from vector potentials $\mathbf{A}$ and $\mathbf{F}$. These equations can be further simplified as (5.1.12) and (5.1.13) (From [7], Chapter 6, Equations (6-119a) - (6.119d)).

$$(E_F)_\theta \approx -j\omega\eta(H_F)_\phi$$

$$\tag{5.1.12}$$

$$(E_F)_\phi \approx +j\omega\eta F_\theta$$

$$(H_A)_\theta \approx +j\omega\frac{A_\phi}{\eta}$$

$$\tag{5.1.13}$$

$$(H_A)_\phi \approx -j\omega\frac{A_\theta}{\eta}$$

By combining (5.1.10) - (5.1.11) and (5.1.12) - (5.1.13), the equations (5.1.8) and (5.1.9) are modified in terms of N and L (see (5.1.14) and (5.1.15)) and these are total $\mathbf{E}$ and $\mathbf{H}$ fields of the antenna, respectively (From [7], Chapter 6, Equations (6-122a) - (6.122f)).

$$E_r \approx 0$$

$$E_\theta \approx -\frac{jke^{-jkr}}{4\pi r}(L_\theta + \eta N_\theta) \tag{5.1.14}$$

$$E_\phi \approx +\frac{jke^{-jkr}}{4\pi r}(L_\theta + \eta N_\phi) \tag{5.1.15}$$

$$H_r \approx 0$$

$$H_\theta \approx \frac{jke^{-jkr}}{4\pi r}(N_\theta - \frac{L_\theta}{\eta}) \tag{5.1.15}$$

$$H_\phi \approx -\frac{jke^{jkr}}{4\pi r}(N_\theta + \frac{L_\theta}{\eta})$$

$\mathbf{N}$ and $\mathbf{L}$ can be retwritten in rectangular component as (5.1.16) and (5.1.17), respectively (From [7], Chapter 6, Equations (6-123a) - (6-123b)).

$$\mathbf{N} = \iint_s (\hat{\mathbf{a}}_\mathbf{x}\mathbf{J}_\mathbf{x} + \hat{\mathbf{a}}_\mathbf{y}\mathbf{J}_\mathbf{y} + \hat{\mathbf{a}}_\mathbf{z}\mathbf{J}_\mathbf{z})e^{jkr'\cos\psi}ds' \tag{5.1.16}$$

$$\mathbf{L} = \iint_s (\hat{\mathbf{a}}_\mathbf{x}\mathbf{M}_\mathbf{x} + \hat{\mathbf{a}}_\mathbf{y}\mathbf{M}_\mathbf{y} + \hat{\mathbf{a}}_\mathbf{z}\mathbf{M}_\mathbf{z})e^{+jkr'\cos\psi}ds' \tag{5.1.17}$$

The rectangular component of $\mathbf{N}$ and $\mathbf{L}$ can be reduced to a form shown in (5.1.18) - (5.1.20), by using rectangular-to-spherical component transformation (From [7], Chapter 6, Equations (6-125a) - (6.125d)) .

$$N_\theta = \iint_s [J_x \cos\theta \cos\phi + J_y \cos\theta \sin\phi - J_z \sin\theta]e^{+jkr'\cos\psi}ds' \tag{5.1.18}$$

$$N_\phi = \iint_s [-J_x \sin\phi + J_y \cos\phi]e^{+jkr'\cos\psi}ds' \tag{5.1.19}$$

$$L_\theta = \iint_s [M_x \cos\theta \cos\phi + M_y \cos\theta \sin\phi - M_z \sin\theta]e^{+jkr'\cos\psi}ds' \tag{5.1.20}$$

$$L_\phi = \iint_s [-M_x \sin\phi + M_y \cos\phi]e^{+jkr'\cos\psi}ds' \tag{5.1.21}$$

Most practical antenna radiators are rectangular therefore, the analysis is also applied to the rectangular radiators. In [1,7], a representation of a rectangular radiator with three different coordinate planes has been discussed. The non-zero components of $\mathbf{J_s}$ and $\mathbf{M_s}$, the differential path, and the differential area can be determined using the different rectangular coordinate system. To summarize the results, in order to find the far-field $\mathbf{E}$ and $\mathbf{H}$ field components of the antenna following the step-by-step procedure are outlined:

- Select a closed surface (S) over which the total $\mathbf{E}$ and $\mathbf{H}$ fields are known. For example, a rectangular patch antenna cavity which has a dielectric slab beneath the radiator.

- Form the equivalent current densities ($\mathbf{J_s}$ and $\mathbf{M_s}$) over the surface.

- Determine N_θ, N_ϕ, L_θ and L_ϕ using (5.1.18)-(5.1.21).

- Determine the radiated $\mathbf{E}$ and $\mathbf{H}$ fields using (5.1.14)-(5.1.15).

5.2 Cavity Model Analysis of Rectangular Patch Antenna (RPA)

RPA consist of the dielectric block between the radiating patch and ground plane, therefore the area where the dielectric is located can be considered as a cavity. The cavity is bounded by an electric wall which is at the top (patch) and bottom (ground plane), and magnetic walls which are at the four sides of the dielectric as shown in Fig. 5.1. This means the top and bottom part of the cavity has perfectly electric walls and four sides of cavity has perfectly conducting magnetic walls. In the past, many successful studies have been reported which compares the results from cavity model analysis with the measurements [1, 6, 8–11] and hence considered as one of the conventional approaches to analyze an antenna.

To understand the physical operation of the cavity model a simple RPA was considered. Now, when the RPA is excited, the positive and negative charge flows at the top and bottom of the patch, and also at the ground plane as shown in [1]. The
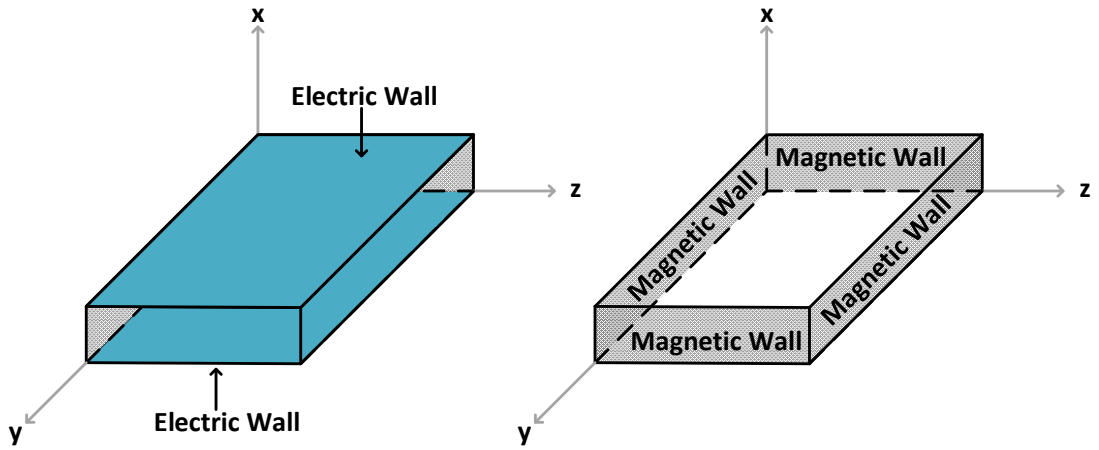
Figure 5.1: Illustration electric (top and bottom side highlighted in blue) and magnetic walls (four side walls highlighted in grey) of the cavity model of the patch antenna.

charge distribution is controlled by attractive[3] and repulsive[4] mechanisms and these movements of charges generates current densities at the top and bottom surface of a patch known at $\mathbf{J_t}$ and $\mathbf{J_b}$, respectively.

As discussed in section (5.1), the RPA can be fed either by the microstrip transmission line or the coaxial probe. For instance, consider the case where the RPA is fed by microstrip, the height to width ratio is directly proportional to the current flow. For example, the height to width ratio of the microstrip RPA decreases that means the current flow will decrease. As a result, the tangential magnetic field along the edges of the patch will be small which makes $\mathbf{J_s}$ very small or negligible [1]. This makes four sidewalls of the dielectric block perfect magnetic conductor surface and hence the electric ($\mathbf{E}$) and magnetic ($\mathbf{H}$) fields will be intact and undisturbed beneath the patch [1]. It is worth mentioning, in practice the tangential magnetic field is not zero, but still cavity model analysis provides good approximation [1].

The RPA is treated only as a cavity, then one cannot represent the radiation patterns because an ideal loss-free cavity does not radiate and its input impedance is purely reactive. An input impedance (Z) which is consist of real resistance (R) and complex reactance (X) and can be found using $Z = R + jX$. In [1], a loss mecha-

---

[3]The attractive mechanism is between the corresponding opposite charges on the bottom side of the patch and the ground plane, which tends to maintain the charge concentration at the bottom of the patch [1]

[4]A repulsive mechanism is between like charges on the bottom surface of the patch, which tends to push some charges from the bottom of the patch, around its edges to its top surface [1].

nism is introduced at the real resistance by using radiation resistance (R_R) and loss resistance (R_L). To account for the radiation, a loss mechanism is introduced by an effective loss tangent, δ_{eff}. The δ_{eff} is reciprocal of antenna quality factor (Q).

In this work, the TM^x field configuration is considered. In cavity model analysis, the height of the substrate is very small. For example, height (H) is much smaller than the wavelength (λ) within the dielectric [1]. This allows fringing fields at the edge of the antenna to be very small due to which the electric field is normal to the surface of the patch. The dominant mode in the microstrip patch antenna is generally TM_{010} [1] mode unless specifically designed for other higher order modes. The studies related to the dominant TM_{010} [1] mode is presented in [1, 11]. The cavity model analysis is used to electric field configuration and directivity of the patch antenna.

Inspired from earlier work on cavity model analysis for the microstrip patch antenna which is present in literature, in this these a cavity model analysis is presented for folded-shorted patch (FSP) antenna. The patch antenna designed for the analysis is probe fed. The objective is to investigate dominant TM_{010} [1] mode and also a higher order TM_{001} [1] mode. The analysis will be focused on higher order mode electric field configuration to derive a general equation which can be used to plot the beam pattern of the antenna. Additionally, the directivity of the antenna at the TM_{001} [1] mode is also evaluated and derived. The results from cavity model analysis are then compared with the full-wave simulations by designing antenna in CST.

5.2.1 Electric Field Configuation at the TM_{010} and TM_{001} modes

Figure 5.2 shows the cavity model of the conventional patch antenna. For this study, the dielectric material which used as a cavity was the air with a dielectric constant (ϵ_r) 1.00057. The width (W) and length (L) of the dielectric substrate (i.e. the cavity within the patch) has same as the size of the patch and is not extended beyond the size of the patch. Equation (5.2.1) [1] shows the singular scalar function A_x which is x component of the magnetic vector potential. In homogenous source-free medium, A_x satisfies the wave equation (see (5.2.2) [1]). The general form of
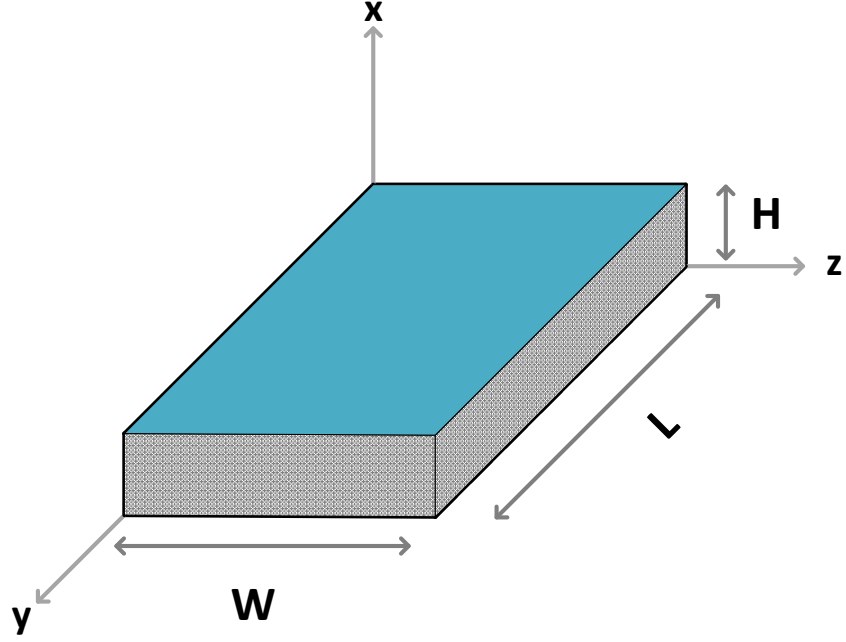
Figure 5.2: Geometry of conventional patch antenna cavity model. Top layer (Blue) is the radiating element of length (L) and width (W). The slab with height (H) is the dielectric substrate and also called cavity.

the vector potential (A_x) wave equation can be further derived by using the steps shown in (5.2.3) [1].

$$\mathbf{A} = A_x \hat{\mathbf{x}} \tag{5.2.1}$$

$$\nabla^2 A_x + k^2 A_x = 0 \tag{5.2.2}$$

$$\frac{\partial^2 A_x}{\partial x^2} + \frac{\partial^2 A_x}{\partial y^2} + \frac{\partial^2 A_x}{\partial z^2} + k^2 A_x = 0$$

where, $A_x = X(x)Y(y)Z(z)$

$$YZ\frac{\partial^2 X}{\partial x^2} + XZ\frac{\partial^2 Y}{\partial y^2} + XY\frac{\partial^2 Z}{\partial z^2} = -k^2 XYZ \tag{5.2.3}$$

$$\frac{d^2 X}{dx^2} + k_x^2 X = 0, \frac{d^2 Y}{dy^2} + k_y^2 Y = 0, \frac{d^2 Z}{dz^2} + k_z^2 Z = 0$$

Equation (5.2.3), k_x, k_y and k_z are the wavenumber along x, y and z direction,

respectively. From wavenumber an eigenvalue equation is derived (see (5.2.4)). In [7], eigen value euqation is also named as constraint equation. k^2 is used to determine the boundary conditions.

$$k_x^2 + k_y^2 + k_z^2 = k^2$$

(5.2.4)

$$k^2 = \omega^2 \mu\epsilon$$

The solution from (5.2.3) can be further simplified and written in even more general form as shown in (5.2.5) [7].

$$A_x = [A_1 cos(k_x x) + B_1 sin(k_x x)][A_2 cos(k_y y) + B_2 sin(k_y y)][A_3 cos(k_z z) + B_3 sin(k_z z)]$$

(5.2.5)

Now the value of A_x is known, it can be substituted to the (5.2.6) and (5.2.7) which are **E** and **H** field components, respectively [7].

$$\mathbf{E} = \hat{a}_x \left[-j\omega A_x - j\frac{1}{\omega\mu\epsilon} \left(\frac{\partial^2 A_x}{\partial x^2} + \frac{\partial^2 A_y}{\partial x \partial y} + \frac{\partial^2 A_z}{\partial x \partial z} \right) - \frac{1}{\epsilon} \left(\frac{\partial F_z}{\partial y} - \frac{\partial F_y}{\partial z} \right) \right]$$

$$+ \hat{a}_y \left[-j\omega A_y - j\frac{1}{\omega\mu\epsilon} \left(\frac{\partial^2 A_x}{\partial x \partial y} + \frac{\partial^2 A_y}{\partial y^2} + \frac{\partial^2 A_z}{\partial y \partial z} \right) - \frac{1}{\epsilon} \left(\frac{\partial F_x}{\partial z} - \frac{\partial F_z}{\partial x} \right) \right]$$

(5.2.6)

$$+ \hat{a}_z \left[-j\omega A_z - j\frac{1}{\omega\mu\epsilon} \left(\frac{\partial^2 A_x}{\partial x \partial y} + \frac{\partial^2 A_y}{\partial y \partial z} + \frac{\partial^2 A_z}{\partial z^2} \right) - \frac{1}{\epsilon} \left(\frac{\partial F_y}{\partial x} - \frac{\partial F_x}{\partial y} \right) \right]$$

$$\mathbf{H} = \hat{a}_x \left[-j\omega F_x - j\frac{1}{\omega\mu\epsilon} \left(\frac{\partial^2 F_x}{\partial x^2} + \frac{\partial^2 F_y}{\partial y \partial z} + \frac{\partial^2 F_z}{\partial x \partial z} \right) - \frac{1}{\mu} \left(\frac{\partial A_z}{\partial y} - \frac{\partial A_y}{\partial z} \right) \right]$$

$$+ \hat{a}_y \left[-j\omega F_y - j\frac{1}{\omega\mu\epsilon} \left(\frac{\partial^2 F_x}{\partial x \partial y} + \frac{\partial^2 F_y}{\partial y^2} + \frac{\partial^2 F_z}{\partial y \partial z} \right) - \frac{1}{\mu} \left(\frac{\partial A_x}{\partial z} - \frac{\partial A_z}{\partial x} \right) \right]$$

(5.2.7)

$$+ \hat{a}_z \left[-j\omega F_z - j\frac{1}{\omega\mu\epsilon} \left(\frac{\partial^2 A_x}{\partial x \partial y} + \frac{\partial^2 A_y}{\partial y \partial z} + \frac{\partial^2 F_z}{\partial z^2} \right) - \frac{1}{\mu} \left(\frac{\partial A_y}{\partial x} - \frac{\partial A_x}{\partial y} \right) \right]$$

The **E** and **H** components are shown in (5.2.8) [7] and (5.2.9) [7]. Since we are deriving fields in TM^x, all the other components of **A** and **F** will be zero apart from A_x.

$$E_x = -j\frac{1}{\omega\mu\epsilon}\left(\frac{\partial^2}{\partial x^2} + k^2\right)A_x$$

$$E_y = -j\frac{1}{\omega\mu\epsilon}\left(\frac{\partial^2 A_x}{\partial x \partial y}\right) \tag{5.2.8}$$

$$E_z = -j\frac{1}{\omega\mu\epsilon}\left(\frac{\partial^2 A_x}{\partial x \partial y}\right)$$

$$H_x = 0$$

$$H_y = \frac{1}{\mu}\frac{\partial A_x}{\partial z} \tag{5.2.9}$$

$$H_z = -\frac{1}{\mu}\frac{\partial A_x}{\partial y}$$

H_x is equal to zero as it is in the direction of wave propagation. A_1, B_1, A_2, B_2, A_3 and B_3 are the unknown constants and can be evaluated in (5.2.8) and (5.2.9). By applying correct boundary conditions, the value of $k_x = \frac{m\pi}{h}$, $k_y = \frac{p\pi}{W}$ and $k_z = \frac{n\pi}{L}$ are found where $m, p, n = 0, 1, 2.., n$ and are half-cycle field variations along x,y and z direction [1]. Therefore, k^2 can be written as (5.2.10) [1] which helps to drive the equation to find resonant frequency (f_{mnp})(see (5.2.11) [1]). The final form of $A_x = A_{mnp}(cos(k_x x')cos(k_y y')cos(k_z z'))$ and it can be substituted to (5.2.8) and (5.2.9) to find the fields within the cavity [1].

$$k^2 = \omega^2\mu\epsilon = \sqrt{\frac{m\pi}{H} + \frac{p\pi}{W} + \frac{n\pi}{L}} \tag{5.2.10}$$

$$f_{mnp} = \frac{1}{2\pi\sqrt{\mu\epsilon}}\sqrt{\frac{m\pi}{H}^2 + \frac{n\pi}{L}^2 + \frac{p\pi}{W}^2} \tag{5.2.11}$$

5.2.2 TM_{010} and TM_{001} Mode Comparison of the Conventional Patch

5.2.2.1 Electric Field Distribution

The electric field configurations for the conventional patch cavity model is demonstrated in Fig. 5.3(a). It shows the electric field structure within the substrate

and the radiating element and the ground plane. For the TM_{010} [1] mode the fields undergo a phase reversal along the length (L) of the patch but they are uniform along the width (W). This uniform pattern along W contributes significantly to the radiation. The phase reversal along L is important for the antenna to generate a broadside radiation pattern in the far-field [1]. For the higher order TM_{001} [1] mode, the electric field pattern is uniform along L of the patch, and the fields are in phase reversal along W as shown in Fig. 5.3(b).
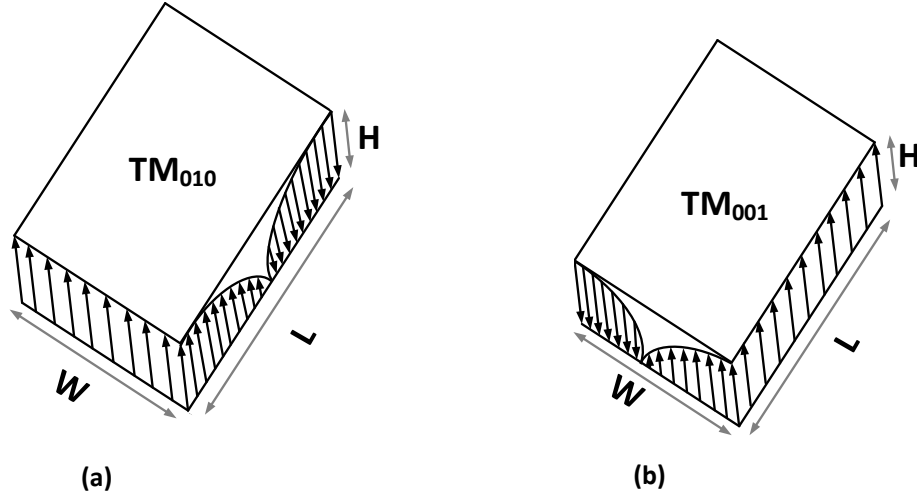
Figure 5.3: Illustration of electric field for the conventional patch antenna at the (a) TM_{010} mode [1] and (b) TM_{001} mode [1].

The electrical length of the patch antenna is $\dfrac{\lambda}{2}$. Therefore, to characterize the TM_{010} and TM_{001} modes in the conventional patch antenna, the resonant frequency $f_{010} = \dfrac{1}{2L\sqrt{\mu\epsilon}}$ and $f_{001} = \dfrac{1}{2W\sqrt{\mu\epsilon}}$ [1] where, L is the length of the patch, W is the width of the patch, μ and ϵ are the permeability and permittivity of the substrate, respectively.

As discussed in section (5.2), the patch cavity has electric current density at the top surface $\mathbf{J_t}$ and four sidewalls consist of electric current desities $\mathbf{J_s}$ and magnetic current density $\mathbf{M_s}$ (see Fig. 5.1). Both $\mathbf{J_s}$ and $\mathbf{M_s}$ are represented in terms of electric ($\mathbf{E_a}$) and magnetic ($\mathbf{H_a}$) fields as shown in (5.2.12) [7], [1]. The edges of the four sidewalls also represents the radiating and non-radiating slots.

$$\mathbf{J_s} = \hat{\mathbf{n}} \times \mathbf{H_a}$$

$$(5.2.12)$$

$$\mathbf{M_s} = -\hat{\mathbf{n}} \times \mathbf{E_a}$$

$\mathbf{J_t}$ and $\mathbf{J_b}$ are negligible because small height to width ratio. Also, the tangential magnetic components are zero at the edge of the patch therefore, $\mathbf{J_s}$ will be zero. Presence of the ground plane will double the magnetic current density $\mathbf{M_s}$ due to image theory. The new value of $\mathbf{M_s}$ is shown in (5.2.13) [1, 7].

$$\mathbf{M_s} = -2\hat{\mathbf{n}} \times \mathbf{E_a} \qquad (5.2.13)$$

5.2.2.2 Fields Radiated by the TM_{010} mode

From the equivalence principle, it is known that each slot radiates the same field and can be modeled as a magnetic dipole with current density $\mathbf{M_s}$ (see (5.2.13)) where $\hat{\mathbf{n}}$ and $\mathbf{E_a}$ are the unit normal vector and electric field at the slots, respectively. The equivalent magnetic current densities along with the two slots, each of width W and height H, are both of the same magnitude and same phase [1]. Therefore, these two slots form a two-element array. Fields generated by these two sources will constructively interfere in a direction normal to the patch and ground plane, forming a broadside pattern in the far-field.

Initially fields over opening is assumed to be [1]:

$$\mathbf{E_a} = \hat{\mathbf{a}}_{\mathbf{x}} E_o \qquad (5.2.14)$$

The magnetic current density is given by (5.2.13), where $\hat{\mathbf{n}}$ is normal in the y direction. Hence, the new value of $\mathbf{M_s}$ is shown in (5.2.15) [1].

$$\mathbf{M_s} = -2\hat{\mathbf{n}}_{\mathbf{y}} \mathbf{E_a}$$

$$\mathbf{M_s} = 2\hat{\mathbf{a}}_{\mathbf{x}} \times \hat{\mathbf{a}}_{\mathbf{y}} E_o$$

$$(5.2.15)$$

$$\mathbf{M_s} = \hat{\mathbf{a}}_{\mathbf{z}} 2E_o$$

$$\mathbf{J_s} = 0$$

From (5.1.18) - (5.1.21), the N_θ, N_ϕ is equal to zero as $\mathbf{J_s} = 0$. L_ϕ is also equal to zero as there is no z component present.

$$L_\theta = \int_{-b/2}^{b/2} \int_{-a/2}^{a/2} [M_z \sin\theta] e^{(jk(x' \sin\theta \cos\phi + z' \cos\theta))} ds' \tag{5.2.16}$$

$$L_\theta = \sin\theta \left[\int_{-b/2}^{b/2} \int_{-a/2}^{a/2} M_z e^{(jk(x' \sin\theta \cos\phi + z' \cos\theta))} ds' \right] \tag{5.2.17}$$

Equation (5.2.17) [1], the integral within the brackets represent the space factor for two dimenstional distribution. For the L_θ component of the vector potential $\mathbf{F}$, the element facor is equal to the product of the factor outside the brackets in (5.2.17) and the factor outside brackets in (5.1.14). The total field is the product of element and space factors. L_θ can be simplified by using the property of intergral that is $\int_{-c/2}^{c/2} e^{j\alpha z} dz = c \left[\dfrac{\sin(\frac{\alpha}{2}c)}{\frac{\alpha}{2}c} \right]$ and (5.2.17) reduces to (5.2.18) [1].

$$L_\theta = 2ab E_o \left[\sin\theta \left(\frac{\sin X}{X} \right) \left(\frac{\sin Z}{Z} \right) \right]$$

Where,

(5.2.18)

$$X = \frac{ka}{2} \sin\theta \cos\phi$$

$$Z = \frac{kb}{2} \cos\theta$$

$$E_\phi = j \frac{abk E_o e^{-jkr}}{2\pi r} \left[\sin\theta \frac{\sin X}{X} \frac{\sin Z}{Z} \right] \tag{5.2.19}$$

Equation (5.2.19) represents the general form of the three-dimentional distribution of the far-field radiation by the aperture [1]. Equation (5.2.20), shows the far field radiation at the TM_{010} mode, where H and W are a and b, respectively, from (5.2.19). Conventional patch antenna has two radiating slots therefore, an array factor needs to be considered. In (5.2.20), AF represent array factor [1].

$$E_\phi = j\frac{HWkE_oe^{-jkr}}{2\pi r}\left[\sin\theta\frac{\sin X}{X}\frac{\sin Z}{Z}\right] \times AF$$

Where,

$$X = \frac{kH}{2}\sin\theta\cos\phi \qquad\qquad (5.2.20)$$

$$Z = \frac{kW}{2}\cos\theta$$

$$AF = 2\cos\left(\frac{kL_e}{2}\sin\theta\sin\phi\right)$$

5.2.2.3 Fields Radiated by the TM_{001} mode

Similar to the dominant mode, the far field radiation equation is derived for the TM_{001} [1] mode for the conventional patch antenna. For the TM_{001} [1] mode, the magnetic current densities have the same magnitude and the same phase along the two slots (L and H from Fig. 5.3) of the patch. Therefore, these two slots form the two-element array with the sources of the same magnitude and phase separated by W. Due to the change in the radiating aperture from W (TM_{010} [1] mode) to L (TM_{001} [1] mode), a change in polarization can be observed.

The electric field radiated by the slots for the higher order TM_{001} [1] mode follows the procedure outlined above for the dominant TM_{010} [1] mode. The total electric field for the coventional patch can be derived as follow:

$$E_a = \hat{a}_x E_o, \text{ Initial field at the open edge}$$

$$M_s = \hat{a}_y 2E_o \text{ Magnetic field}$$

$$N_\theta = N_\phi = 0 \text{ From (5.1.18)-(5.1.19)}$$

$$L_\theta = \int_{-c/2}^{c/2} \int_{-a/2}^{a/2} [M_y \cos\theta \sin\phi] e^{jkr' \cos\psi} ds'$$

$$L_\theta = \int_{-c/2}^{c/2} \int_{-a/2}^{a/2} [M_y \cos\theta \sin\phi] e^{jk(x' \sin\theta \cos\phi + y' \sin\theta \cos\phi)} ds'$$

$$L_\theta = \cos\theta \sin\phi [M_y e^{jk(x' \sin\theta \cos\phi + y' \sin\theta \sin\phi)}] dx' dy'$$

$$L_\theta = 2hLE_o [\cos\theta \sin\phi \frac{\sin X}{X} \frac{\sin Y}{Y}]$$

$$X = \frac{kH}{2} \sin\theta \sin\phi, \quad Y = \frac{kL}{2} \sin\theta \sin\phi \tag{5.2.21}$$

Similarly for,

$$L_\phi = \int_{-c/2}^{c/2} \int_{-a/2}^{a/2} [M_y cos\phi] e^{jk(x' \sin\theta \cos\phi + y' \sin\theta \sin\phi)} dx' dy'$$

$$L_\phi = 2HLE_o \left[\cos\phi \frac{\sin X}{X} \frac{\sin Y}{Y} \right]$$

$$X = \frac{kH}{2} \sin\theta \cos\phi, \quad Y = \frac{kL}{2} \sin\theta \sin\phi$$

$$E_\theta = \frac{jkhLE_o e^{-jkr}}{2\pi r} \left[\cos\theta \sin\phi \frac{\sin X}{X} \right] \times AF$$

$$E_\phi = \frac{jkhLE_o e^{-jkr}}{2\pi r} \left[\cos\phi \frac{\sin X}{X} \frac{\sin Y}{Y} \right] \times AF$$

$$AF = 2\cos(\frac{kW}{2} \cos\theta)$$

5.2.2.4 Directivity of the Conventional Patch Antenna at the TM_{010} mode

Once the far-field radiation equations are derived, the next step is to derive the directivity of the patch antenna at the TM_{010} mode. For every antenna the directivity D is the figure of merit and is defined by $D_o = \dfrac{U_{max}}{U_o}$, where U_{max} is the maximum radiation intensity and U_o is the radiation intensity of the isotropic source [1]. The D_o can be further simplified as $D_o = \dfrac{4\pi U_{max}}{P_{rad}}$ where P_{rad} is the radiated power. The directivity of an isotropic source is unity since its power radiated equally in all directions. But in non-ideal case for all other sources, the maximum directivity will be higher than unity and since it is a relative figure of merit which means it gives an assurance about the directional properties of the antenna [1]. The value of directivity is equal to or greater than zero and should be equal to or less than maximum directivity.

The general equation of the D_o can further be written in terms of θ and ϕ components using the radiation equations derived in previous sections. The directivity can be written as $D_o = D_\theta + D_\phi$ [1]. Following the definition the radiation pattern of the antenna can written as ([1], Chapter 2, (2-19)):

$$U = B_o F(\theta, \phi) \approx \frac{1}{2\eta}[|E_\theta^o(\theta, \phi)|^2 + |E_\phi^o(\theta, \phi)|]$$

$$\text{Where, } B_o = \text{constant} \tag{5.2.22}$$

$$E_\theta^o = E_\phi^o = \text{Antenna far field electric field components}$$

Likewise the maximum radiation intensity (U_{max}) and power radiated (P_{rad}) can be written as ([1], Chapter 2, (2-20)):

$$U = B_o F_{max}(\theta, \phi)$$

$$\tag{5.2.23}$$

$$P_{rad} = B_o \int_0^{2\pi} \int_0^\pi F(\theta, \phi) \sin\theta d\theta d\phi$$

The general equation for directivity can derived by subsituting (5.2.22) and (5.2.23) in D_o (see 5.2.24, [1], Chapter 2, (2-21)).

$$D(\theta, \phi) = 4\pi \frac{F(\theta, \phi)}{\int_0^{2\pi} \int_0^{\pi} F(\theta, \phi) \sin\theta d\theta d\phi} \tag{5.2.24}$$

Using (5.2.24), the directivity equation for the TM_{010} mode for the patch antenna can be derived. The directivity for the TM_{010} mode is represented as D_{010} and is shown in equation (5.2.25) [1].

$$D_{010} = 4\pi \frac{U_{max}}{P_{rad}}$$

F(θ, ϕ) can be wirtten as

$$F(\theta, \phi) = \int_0^{\pi} \int_0^{\pi} \left[\frac{\sin\left(\frac{kW}{2}\right)\cos\theta}{\cos\theta} \right]^2 \sin^2\theta \times AF \tag{5.2.25}$$

Therefore,

$$D_{010} = \frac{4\pi}{\int_0^{\pi} \int_0^{\pi} \left[\frac{\sin\left(\frac{kW}{2}\right)\cos\theta}{\cos\theta} \right]^2 \sin^2\theta \times AF}$$

5.2.2.5 Directivity of the Patch Antenna at the TM_{001} mode

Similar to the TM_{010} mode the directivity of TM_{001} mode can derived [1]. The directivity at the TM_{001} mode can repressented as D_{001} and is derived in (5.2.26).

$$D_{010} = 4\pi \frac{U_{max}}{P_{rad}}$$

F(θ, ϕ) can be wirtten as

$$F(\theta, \phi) = \int_0^\pi \int_0^\pi [\sqrt{1 - \sin^2 \phi \sin^2 \theta}] \left(\frac{\sin X}{X}\right) \left(\frac{\sin Y}{Y}\right) \times AF \qquad (5.2.26)$$

Therefore,

$$D_{001} = \frac{4\pi}{\int_0^\pi \int_0^\pi [\sqrt{1 - \sin^2 \phi \sin^2 \theta}] \left(\frac{\sin X}{X}\right) \left(\frac{\sin Y}{Y}\right) \times AF}$$

5.3 Cavity Model Analysis of the folded-shorted patch (FSP) antenna

It is well known that the standard microstrip patch antenna has a resonant electrical length of about $\lambda/2$ and its electric field is zero at the centre of the patch. Therefore, a shorting plate can be introduced at the centre of the patch, as well as the folding of the ground plane, without significantly affecting the resonant frequency and matching. Based on this miniaturization technique, a N-layered FSP antenna can be designed. Electric-fields of the FSP antenna are analyzed to derive the far-field radiation equations for the TM_{010} and TM_{001} modes [1]. Also, similar to conventional patch antenna the directivity of the FSP antenna is derived. In this work, a three-layer FSP antenna was used for cavity model analysis.

To characterize the modes for the FSP, the resonant frequency equations such as $f_{010} \approx \dfrac{1}{4L\sqrt{\mu\epsilon}}$ and $f_{001} \approx \dfrac{1}{4W\sqrt{\mu\epsilon}}$ can be used as mentioned in [1], [11], for the conventional patch antenna. L and W are length and width of the FSP antenna, respectively. These equations should also satisfy the condition such as $L > W > H$ for the TM_{010} mode and $L > W > L/2$ for the TM_{001} mode [1], [11]. H is the overall thickness of the substrate of the FSP antenna. Figure 5.4 shows cavity model of the FSP antenna.

Electric field configuration for the FSP antenna at the TM_{010} and TM_{001} [1] modes
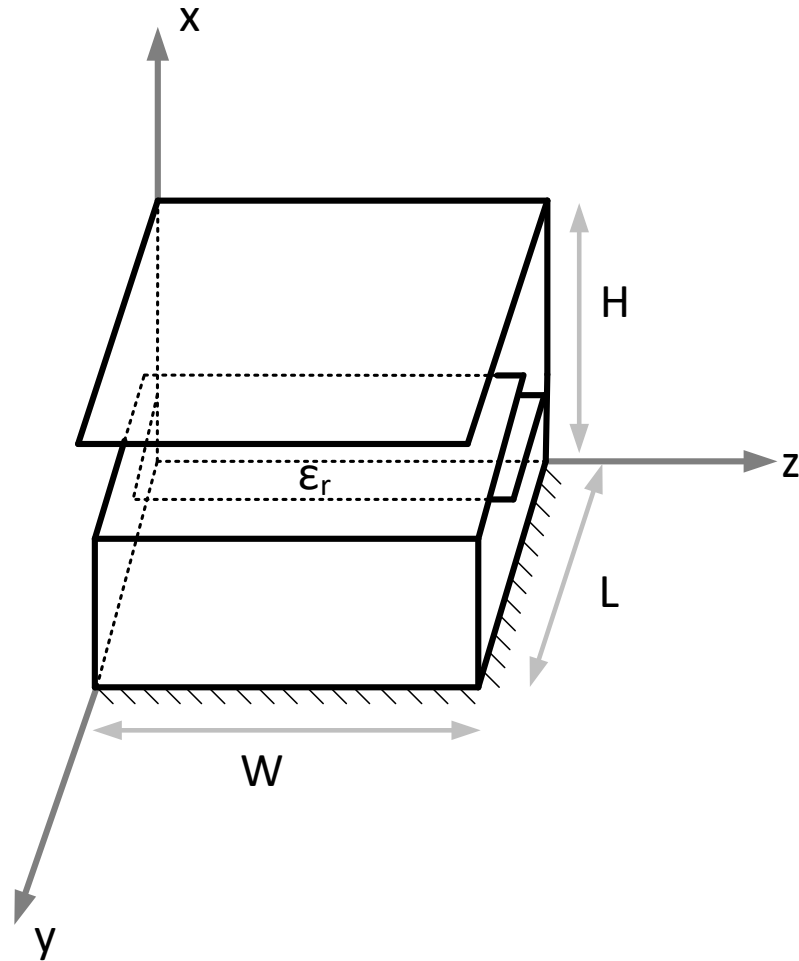
Figure 5.4: Geometry of FSP antenna cavity model. Top layer is the radiating element of length (L) and width (W). The slab with height (H) is the dielectric substrate and also called cavity.
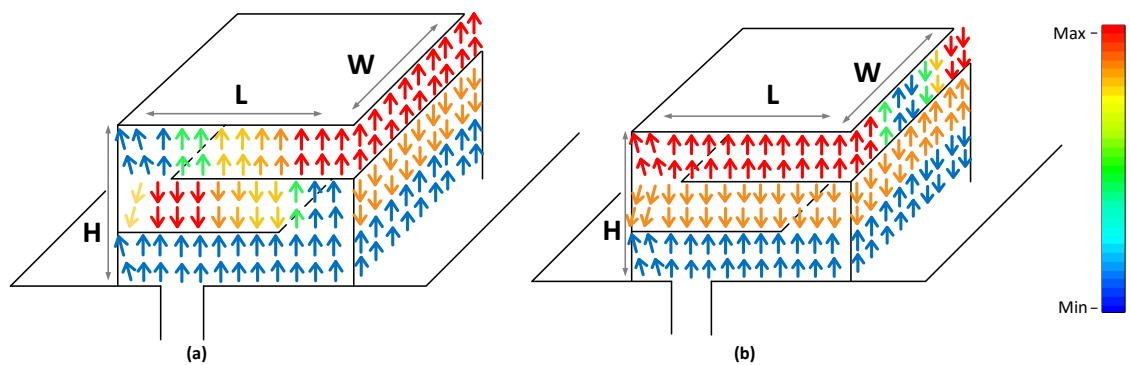
Figure 5.5: Illustration of the electric field for the FSP antenna at the (a) TM_{010} [1] mode and (b) TM_{001} [1] mode [12].

are illustrated in Fig. 5.5 (a and b). Conventional patch antenna has two radiating slots that contributes to radiation whereas FSP antenna has single radiationg slot. Due to the single radiating slot the gain of the antenna is usually lower than the

conventional patch antenna. Fringing fields which are responsible for radiation are shorted on the far end, so only field nearest the transmission line radiates.
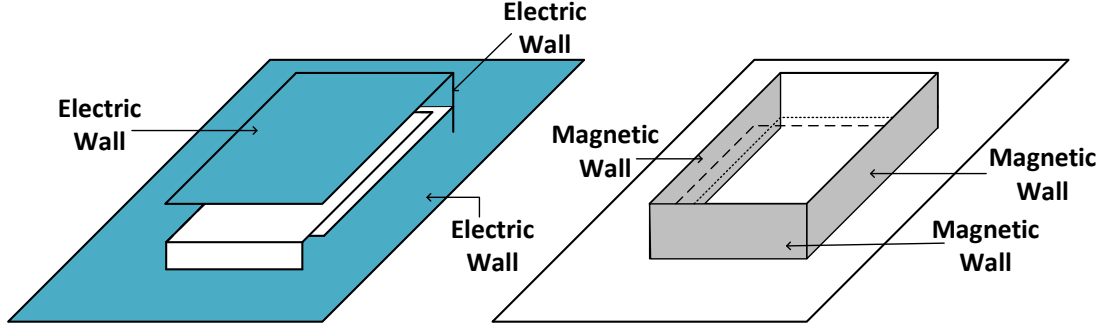
Figure 5.6: Illustration electric and magnetic walls of the cavity model of the FSP antenna.

5.3.1 Fields radiated by the TM_{010} mode

As discussed in section (5.2.1), it is known that each slot radiates the same field and can be modelled as a magnetic dipole current density $\mathbf{M_s}$ = -2$\mathbf{\hat{n}}$ × $\mathbf{E_a}$, where $\mathbf{\hat{n}}$ and $\mathbf{E_a}$ are unit normal vector and electric field at the slot, respectively. Unlike patch antenna, FSP has three electric and three magetic walls (see Fig. 5.6). Hence, field radiated by the FSP is through a single slot. In order to analyze these fields, a similar procedure is followed as mentioned above for the conventional patch antenna. The equivalent magnetic current densities are concentrated along the single slot on the top layer. Therefore, the electric fields radiated by a single slot in the far-field using an equivalent current can be shown to be:

$$E_r \approx E_\theta = 0 \quad \text{no z component, therefore } (L_\phi = 0)$$

$$E_\phi = j\frac{HWkE_o e^{-jkr}}{\pi r}\left[\sin\theta\frac{\sin X}{X}\frac{\sin Z}{Z}\right]$$

$$\text{Where,} \quad X = \frac{kH}{2}\sin\theta\cos\phi$$

$$Z = \frac{kW}{2}\cos\theta$$

(5.3.1)

5.3.2 Fields radiated by the TM_{001} mode

Similar to the dominant TM_{010} mode, the FSP antenna was also analyzed using the cavity model and CST simulation for the TM_{001} [1] mode. Considering the infinite ground plane where the dielectric material is only defined by the dimensions of the single radiating element. For the FSP, at the TM_{001} [1] mode, the magnetic current densities have the same magnitude along the two slots (L and H). Therefore, these two slots form a two-element array with the sources of the same magnitude and phase separated by W. Similar to the conventional patch antenna, due to the change in radiation aperture, a change in polarization is observed.

The electric field radiated by the slots for the higher order TM_{001} mode follows the procedure outlined in (5.2.21). The total electric field for the FSP will same as the conventional patch antenna.

5.3.3 Broadside Directivity of the FSP antenna at the TM_{010} and TM_{001} mode

Directivity equation for the FSP antenna is derived using the procedure mentioned in (5.2.25) for dominant TM_{010} [1] mode. For the FSP, at the TM_{010} [1] mode, fields are radiated from a single slot. Hence, the directivity of the FSP can be derived using the procedure outlined in ([1], Ch. 14, (14-55)-(14-56)) and (5.2.22)-(5.2.25) for the conventional patch antenna without an array factor term:

$$D_{FSP010} = 4\pi \frac{U_{max}}{P_{rad}}$$

F(θ, ϕ) can be wirtten as

$$F(\theta,\phi) = \int_0^\pi \int_0^\pi [\frac{\sin(\frac{kW}{2})\cos\theta}{\cos\theta}]^2 \sin^2\theta \tag{5.3.2}$$

Therefore, $D_{FSP010} = \dfrac{4\pi}{\int_0^\pi \int_0^\pi \left[\dfrac{\sin\left(\dfrac{kW}{2}\right)\cos\theta}{\cos\theta}\right]^2 \sin^2\theta}$

Similarly, using the aforementioned procedure to derive the directivity for the TM_{010} [1] mode, an expression for the directivity at TM_{001} [1] mode can also be obtained. Using (5.2.26) where the directivity equation for patch antenna is shown, in a similar way the directivity equation for the FSP antenna can be derived including the array factor term:

$$D_{FSP010} = 4\pi \frac{U_{max}}{P_{rad}}$$

F(θ, ϕ) can be wirtten as

$$F(\theta, \phi) = \int_0^\pi \int_0^\pi [\sqrt{1 - \sin^2 \phi \sin^2 \theta}](\frac{\sin X}{X})(\frac{\sin Y}{Y}) \times AF$$

(5.3.3)

Therefore,

$$D_{FSP001} = \frac{4\pi}{\int_0^\pi \int_0^\pi [\sqrt{1 - \sin^2 \phi \sin^2 \theta}] \left(\frac{\sin X}{X}\right) \left(\frac{\sin Y}{Y}\right) \times AF}$$

$$AF = \cos\left(\frac{kL_e}{2} \cos \theta\right)$$

5.4 Comparison of Theoretical and Simulation Results for the Cavity Model Analysis for the Conventional Patch and FSP Antenna

Equation (5.3.1) shows the field radiated by the FSP antenna at the TM_{010} [1] mode. The E- and H-plane pattern using the cavity model for the TM_{010} mode has been plotted by using (5.2.20) and (5.3.1) with MATLAB and compared to CST simulations for the patch and the FSP antenna considering an air substrate, i.e. $\epsilon_r = 1.00057$. For both antennas, $xy-$ plane ($\theta = 90°$, $0° \geq \phi \geq 90°$ and $270° \geq \phi$ 360°) is the principal $E-$plane while the $H-$plane is the $xz-$ plane ($\phi = 0°$, $0° \geq \theta \geq 180°$). Figure 5.7(a) and 5.7(b) report the beam pattern for the conventional patch and the FSP antenna at the TM_{001} [1] mode, respectively. The numerically determined results were compared with commercial software package
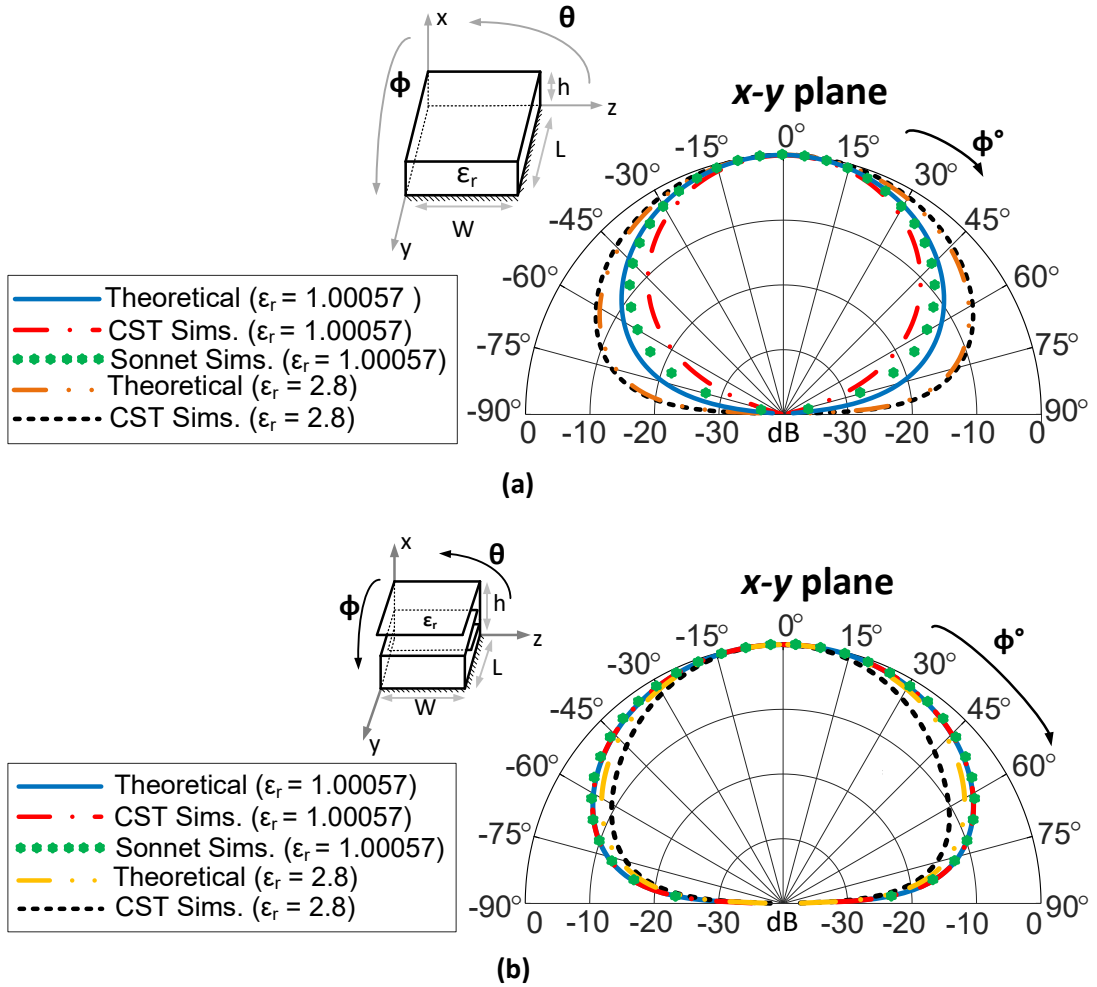
Figure 5.7: (a) Beam pattern for the conventional patch antenna in the xy- plane for the higher order mode (TM_{001}). (b) Beam pattern for the FSP antenna in the xy- plane for the TM_{001} higher order mode. The theoretical beam patterns were plotted using (5.2.21). These cavity model calculations were compared with Sonnet and CST simulations [12].

CST and Sonnet. The FSP and patch was designed using air as a substrate with an infinite ground plane. A good agreement between the theoretical and the simualted beam patterns can be observed. The theoretically determined directivity for both the conventional patch antenna and the FSP considering an air dielectric have been plotted using MATLAB and compared to full wave simulation. Figure 5.8 shows the directivity plot at the TM_{010} [1] mode for the patch and FSP antenna. It can be observed that the directivity of the FSP is reduced by up to 4 dB when compared with the conventional patch antenna.

Similarly, Fig. 5.9 shows a comparison of the directivity of the FSP and the conventional patch antenna at the TM_{001} [1] mode considering air as dielectric substrate. The results are in close agreement with the simulations.
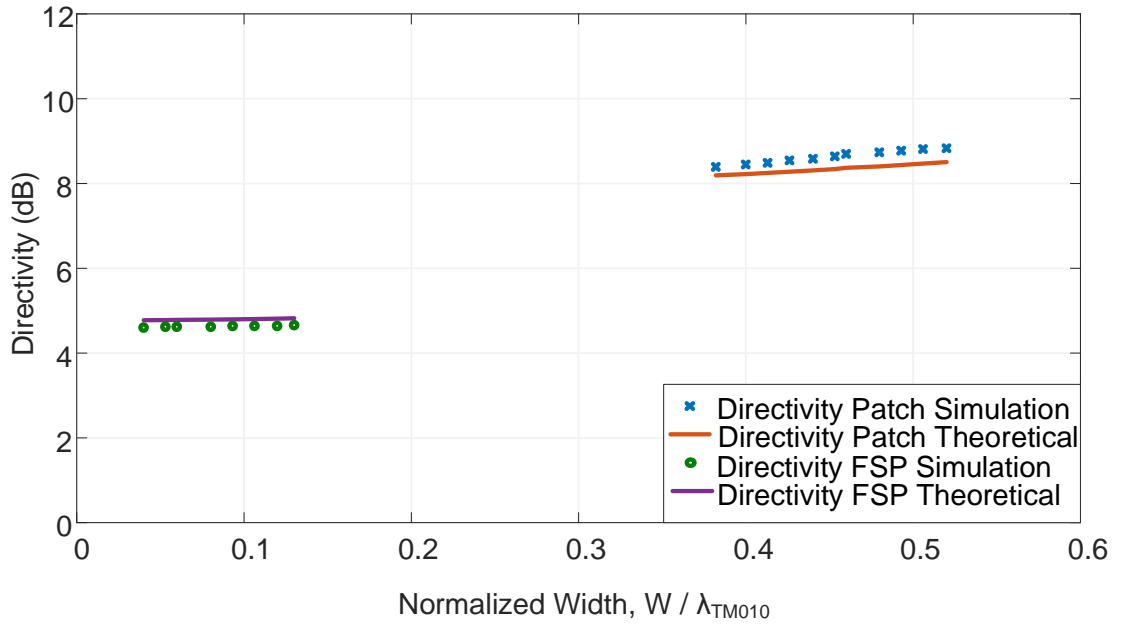
Figure 5.8: Numerically derived directivity for the conventional patch antenna and the FSP at the TM_{010} mode. Full-wave CST simulations of the conventional patch antenna and the three-layer FSP antenna are in close agreement with numerically derived directivity values. Both antennas are probe fed with air as a substrate between the metallic layers. Results are compared when the width is normalized by the wavelength considering the TM_{010} mode [12].
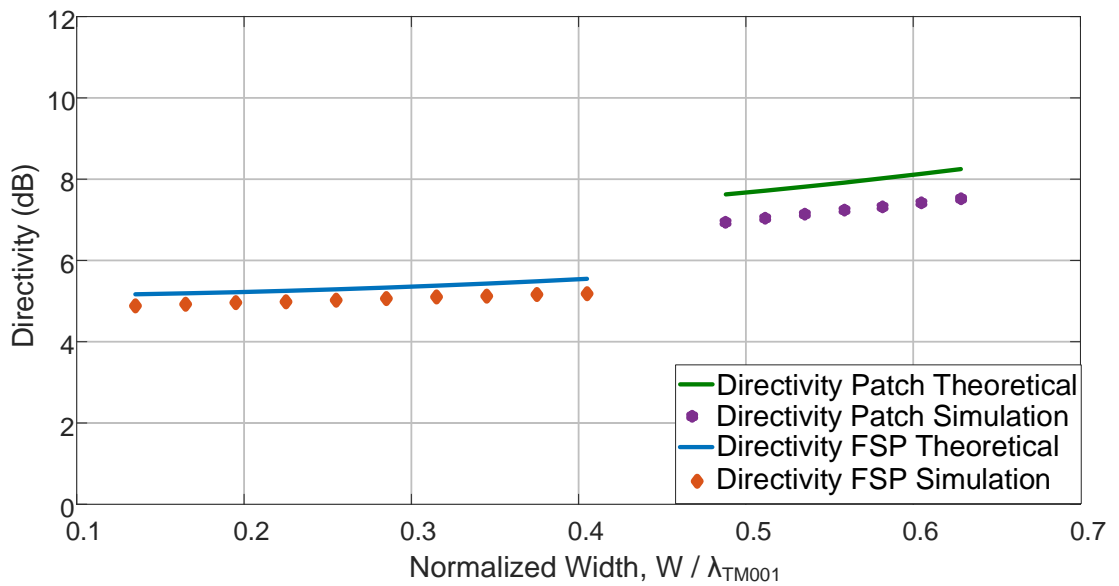
Figure 5.9: Numerically derived directivity for the conventional patch antenna and the FSP antenna at the TM_{001} higher order mode. Full-wave simulations of the conventional patch antenna and the three-layer FSP antenna are in close agreement. Both antennas are probe fed with air as a substrate between the metallic layers [12].

1. Antenna Dimensions

$L > W > H$ → $f_{010} \approx \dfrac{1}{4L\sqrt{\mu\epsilon}}$ → TM$_{010}$ Mode

$L > W > \dfrac{L}{2}$ → $f_{001} \approx \dfrac{1}{4W\sqrt{\mu\epsilon}}$ → TM$_{001}$ Mode

2. Beam Pattern Equations

$$E_\varphi = \frac{khWE_o e^{-jk_o r}}{\pi r}\left\{sin\theta \frac{si\,n(X)}{X}\frac{si\,n(Z)}{Z}\right\}$$
$$E_\theta = 0$$
TM$_{010}$ Mode

$$E_\varphi = \frac{khLE_o e^{-jk_o r}}{\pi r}\left\{cos\theta sin\varphi \frac{si\,n(X)}{X}\frac{si\,n(Y)}{Y}\right\} \times cos\left(\frac{kW}{2}cos\theta\right)$$
$$E_\theta = \frac{khLE_o e^{-jk_o r}}{\pi r}\left\{cos\varphi \frac{si\,n(X)}{X}\frac{si\,n(Y)}{Y}\right\} \times cos\left(\frac{kW}{2}cos\theta\right)$$
TM$_{001}$ Mode

3. Directivity Equations

$$D = 4\pi \times \frac{1}{\iint_0^{2\pi}\left[\dfrac{sin\left(\frac{kW}{2}cos\theta\right)}{cos\theta}\right]^2 sin^3\theta d\theta d\varphi}$$
TM$_{010}$ Mode

$$D = 4\pi \times \frac{1}{\iint_0^{2\pi}\left[\sqrt{1-sin^2\theta sin^2\varphi}\right]cos\left(\frac{kL_e}{2}cos\theta\right)\frac{sin(X)}{X}\frac{sin(Y)}{Y}sin\theta d\theta d\varphi}$$
TM$_{001}$ Mode
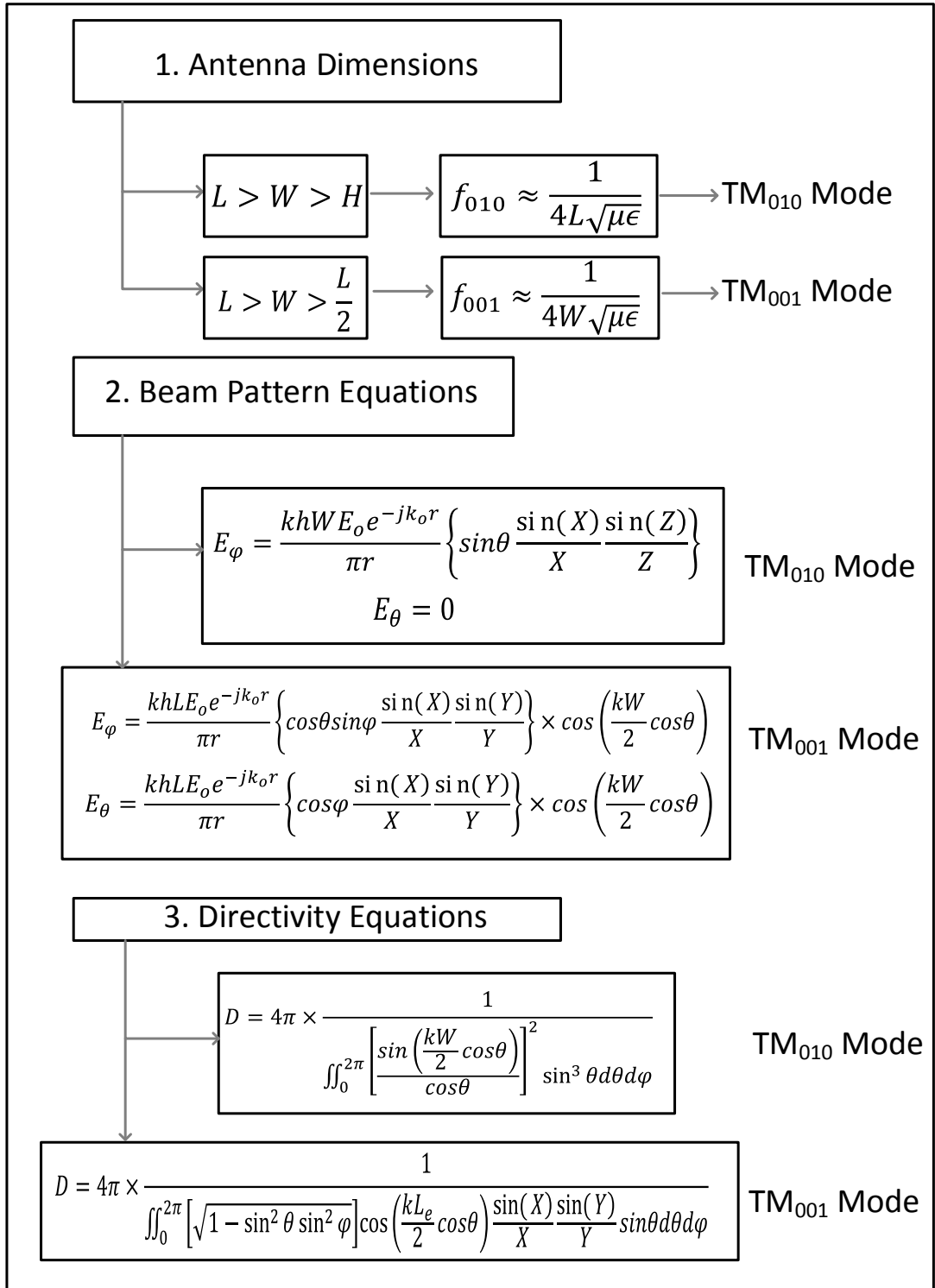
Figure 5.10: Diagram summarizing the step-by-step design procedure and modelling approach for the FSP ensuring the TM_{010} and TM_{001} modes [12].

5.4.1 Summary of the Developed Analysis and Design Approach for the FSP

A complete and newly developed analysis for the design of the FSP has been reported along with simple design equations which follow the cavity model. These findings can

allow the antenna designer to predict the beam pattern shape and peak directivity values. Figure 5.10 shows a summarized design flow diagram starting from the dimensions needed to the peak directivity of the FSP. These design equations help to ensure operation of the relevant TM modes.

Also, once the modes of the antenna have been achieved, the pattern of the antenna can be estimated using (5.2.21) and (5.3.1) to ensure an omni-directional-like beam pattern with no nulls. It should also be mentioned that the beam patterns of other operating modes (such as the TM_{020} [1] or the TM_{030} [1] mode) can also be derived using the procedure mentioned in [1]. Likewise, the peak directivity of the FSP antenna can also be calculated using (5.3.2) and (5.3.3).

5.5   Summary of the Chapter

This chapter describes the cavity model analysis on the patch antenna and FSP antenna. The objective here was to investigate the performance of the simple rectangular patch and FSP antennas for the dominant TM_{010} and TM_{001} [1] modes. The far-field radiation equation and directivity equation was derived using cavity model analysis for the dominant and higher order mode for both antennas. Radiation takes place efficiently only when the excitation is at the resonant frequency of a mode. A detailed background theory was also presented which highlighted the geometry of the patch antenna. An electric field configuration is demonstrated at the TM_{010} and TM_{001} [1] modes. This configuration helps to analyze radiating and non-radiating slots of the conventional patch antenna. The cavity model analysis was also used derive far-field and directivity equations for FSP antenna.

References

[1] C. A. Balanis, *Antenna theory: analysis and design.* John Wiley & Sons, 2016.

[2] E. Newman and P. Tulyathan, "Analysis of microstrip antennas using moment methods," *IEEE Transactions on Antennas and Propagation*, vol. 29, no. 1, pp. 47–53, January 1981.

[3] C.-J. Wang and S.-W. Chang, "A technique of bandwidth enhancement for the slot antenna," *IEEE Transactions on Antennas and Propagation*, vol. 56, no. 10, pp. 3321–3324, 2008.

[4] D. N. Elsheakh, H. A. Elsadek, E. A. Abdallah, H. Elhenawy, and M. F. Iskander, "Enhancement of microstrip monopole antenna bandwidth by using EBG structures," *IEEE Antennas and Wireless Propagation Letters*, vol. 8, pp. 959–962, 2009.

[5] P. Jin and R. W. Ziolkowski, "Broadband, efficient, electrically small metamaterial-inspired antennas facilitated by active near-field resonant parasitic elements," *IEEE Transactions on Antennas and Propagation*, vol. 58, no. 2, pp. 318–327, Feb 2010.

[6] Y. Lo, D. Solomon, and W. Richards, "Theory and experiment on microstrip antennas," *IEEE Transactions on Antennas and Propagation*, vol. 27, no. 2, pp. 137–145, March 1979.

[7] C. A. Balanis, *Advanced engineering electromagnetics.* John Wiley & Sons, 1999.

[8] G. Dubost, "Far field radiated by rectangular patch microstrip antenna," *Electronics Letters*, vol. 18, no. 23, pp. 991–993, November 1982.

[9] K. Carver and J. Mink, "Microstrip antenna technology," *IEEE Transactions on Antennas and Propagation*, vol. 29, no. 1, pp. 2–24, January 1981.

[10] W. Richards, Yuen Lo, and D. Harrison, "An improved theory for microstrip antennas and applications," *IEEE Transactions on Antennas and Propagation*, vol. 29, no. 1, pp. 38–46, January 1981.

[11] R. Garg, P. Bhartia, I. J. Bahl, and A. Ittipiboon, *Microstrip antenna design handbook.* Artech House, 2001.

[12] R. Joshi, S. K. Podilchak, D. E. Anagnostou, C. Constantinides, M. N. Ramli, H. Lago, and P. J. Soh, "Analysis and design of dual-band folded-shorted patch antennas for robust wearable applications," *IEEE Open Journal of Antennas and Propagation*, vol. 1, pp. 239–252, 2020.

Chapter 6

Design of Dual-Band Folded-Shorted Patch (FSP) Antenna for Wearable Applications

In this chapter, a dual-band FSP antenna using a PDMS substrate is presented. The proposed antenna is operational at 400 MHz and 2.4 GHz and is developed for military search and rescue operationa and emergency services. The proposed design exploits TM_{010} and TM_{001} operating modes. This chapter is outlined as follows. In Section 6.1, the design motivation of dual-band antenna for intended wearable application is described. In Section 6.2, an antenna design overview is provided and compared with the previous FSP antennas in the literature. The proposed antenna design, assembly and fabrication process is described in Section 6.3. Measurement results are described and discussed in Section 6.4 while a suggested proposed design optimization is described in Section 6.5. A summary of the chapter is discussed in Section 6.6.

6.1   Introduction

A wearable antenna for military search and rescue operations and emergency services and provides dual-band functionality. Antennas for such application requires

operation at the UHF and ISM frequency bands. Therefore, there is a need for an antenna with dual-band functionality. When considering wearable antennas operating at the UHF and the ISM band, patch-like antennas are generally preferred due to their low profile, possible miniaturization approaches, and relatively low cost implementations. Previous and more commercially available beacon signal UHF devices were hand held and bulky with classic monopole antennas of length $\lambda/4$. However, there are also several size reduction techniques for the conventional patches and monopole have been developed and are implemented. Some of these techniques use high dielectric materials [1–3], introducing slots in the design [4–6], bending and folding of the planar elements [7], and lumped element loading.

The bending and folding technique or the addition of a metallic shorting wall is one effective method. As is well known, folded antennas such as the inverted-F antenna (IFA) and the planar inverted-F antenna (PIFA) are used widely for many applications and are typically a quarter wavelength in the size when only considering the antenna itself [7, 8]. However, the size of the PIFA can be further reduced to less than $\lambda/4$ by folding the patch element further into multiple layers and forming a multilayer structure. This structure is generally two or more layers defining a folded-shorted patch (FSP) antenna.

The concept of the FSP antenna was originally introduced in [9] and developed further in [10] and [11]. Following these earlier developments a dual-band FSP was proposed for operation at about 800 MHz and 2.2 GHz [12]. Fig 6.1 shows the different FSP designs available in the literature. Preliminary results were reported in Chapter 2 and in [13] for a simple and single-layer circularly polarized (CP) patch antenna where durability and resiliency studies were completed for the adopted polydimethylsiloxane (PDMS) substrate in terms of bending, wet and temperature testing. Results suggest that such an antenna can withstand these operational conditions and without significant performance degradations in terms of variations in impedance matching and antenna gain. Following these developments some preliminary results for a three-layer FSP using PDMS were reported in [14] considering its potential for dual-band functionality. Concepts and antenna analysis is further explained in this chapter for a new and optimized, dual-band antenna unit which can operate at about 400 MHz and 2.4 GHz, and where the relevant radiating modes are fully explained and the benefits of these patch modes (see Fig. 6.2) are discussed
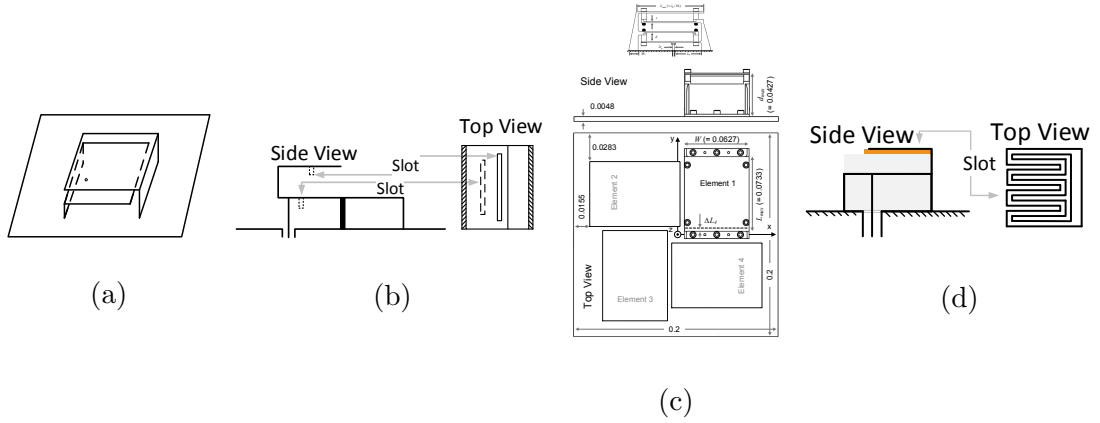
Figure 6.1: Diagram showing different design of folded-shorted patch antenna developed in past decades. (a) 2-layered FSP antenna [9], (b) 2-layered FSP with slots [12], (c) 4-layered circular polarized FSP [10] and (d) 2-layered with FSP with meandered slots [15]

when compared to previously reported antenna structures.

6.2 Antenna Design Overview

The proposed PDMS antenna in this thesis exploits the TM_{010} and the TM_{001} modes of the FSP and these modes are achieved without the introduction of slots, as in [12] and [15], where the FSP antennas operated by the TM_{010} and TM_{030} modes. This can make the antenna design simpler and easier to fabricate when considering the TM_{010} [16] and the TM_{001} [16] modes. More importantly, the TM_{030} [16] mode and other higher order modes can exhibit unwanted nulls in the beam pattern [16] (see pattern simulations in Fig. 6.2 (a) and (b) for conventional patch and FSP, respectively, where a comparison of these modes is provided) which might not be appropriate for the intended wearable application.

It should also be mentioned that for the higher order TM_{001} mode, the fields radiate from the opposite edges of the antenna when compared to the TM_{010} mode by the cavity model for the single-layer patch [16]. As a consequence, the polarization of the FSP changes but it still maintains broadside radiation and with reduced side lobe levels. Also, the proposed FSP structure is without slots, which can lead to unperturbed current paths [17] for both the TM_{010} [16] and the TM_{001} [16] modes. This supports sustained broadside radiation. Due to these important design considerations, the proposed FSP structure has two operational frequencies with orthogonal polarization. This is achieved using a single feed point as described previously in [17] for a more conventional patch.
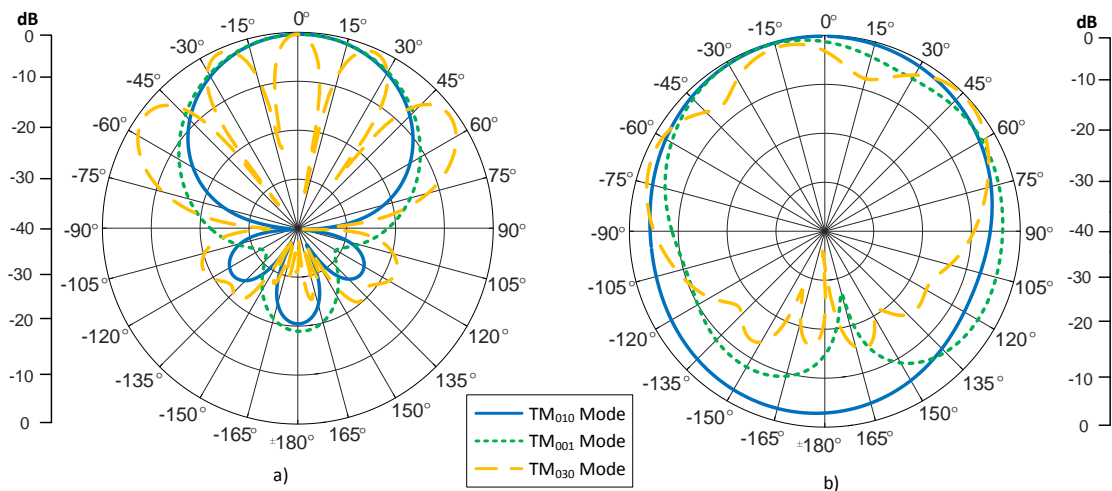
Figure 6.2: Beam pattern at the TM_{010}, TM_{001} and TM_{030} modes [16] for (a) Conventional patch antenna and (b) three-layer FSP antenna. For the FSP at the TM_{030} [16] modes has multiple side lobes whereas other two modes have a more omnidirectional-like pattern with broadside radiation.

These modes are further examined and compared to other similar works [12] and [15], mainly, the proposed antenna is analyzed and designed by employing the cavity model for the conventional patch [16, 18] and applying it to a multi-layer FSP. In the forthcoming sections closed-form equations are newly derived to calculate the beam pattern and the directivity. Results are validated by comparisons between theory, full-wave simulations, and measurements. The developed analysis approach, specifically for FSPs, easily allows the antenna engineer to estimate the operational frequency, pattern shape, polarization, and directivity prior to any simulation and fabrication activity. This can help to reduce design and optimization time.

The proposed FSP antenna is also relatively smaller in size compared to the designs reported in [9, 10, 12] and [15] when considering the first operating mode. In this work, dual frequency operation is achieved by tuning the size of the layers of the FSP antenna. Also, the top layer of the proposed FSP antenna is dependant to the TM_{010} [16] mode which means by varying the size of the top layer (layer 3, see Fig. 6.4) one can tune the frequency of the dominant (TM_{010}) mode. Also, it was found that the other two layers (layer 1 and layer 2, see Fig. 6.4) are proportional to the higher order TM_{001} [16] mode. The TM_{001} [16] mode can be tuned to a particular frequency while the TM_{010} [16] mode is maintained.

Table 6.1 summaries the advantages of the proposed FSP antenna as compared to other designs reported in the literature. For example, the impedance fractional bandwidth (FBW) of the proposed antenna both at the dominant (400 MHz) mode

(UHF band frequency range) and at the higher order (2.4 GHz) mode (ISM band frequency range) is larger than in [15]. It should also be mentioned that in [12] slots were used to enhance the bandwidth (BW) of the FSP antenna and making it a multiband antenna. This approach with slot inclusions can possibly increase the design complexity. The proposed FSP antenna has a simple geometry without any slots and yet is still able to offer a FBW of more than 7% at the higher order mode. At 400 MHz, the FBW is 3.5% (and is still larger than [15] for the fundamental mode). It is also worth mentioning here that for this TM_{010} mode the proposed FSP is compact ($0.13\ \lambda_o \times 0.13\lambda_o \times 0.02\lambda_o$) when compared to [12] and [15]. The relatively narrow impedance FBW of 3.5% at 400 MHz, means that the wearable antenna can work as a beacon antenna for telemetry applications since low data rates are required. Also, the proposed FSP antenna has a relatively smaller single element footprint and volume as compared to the designs reported in [9, 12, 15] for the TM_{010} mode (see Table 6.1).

Table 6.1: Comparison of Other FSP Structures Found in the Literature

Parameter	[9]	[10]	[12]	[15]	This Work
Frequency	2.4 GHz	400 MHz	823 MHz / 2.194 GHz	2.4 GHz / 5 GHz	400 MHz / 2.4 GHz
Single-element Size	$0.15\lambda_o \times 0.08\lambda_o \times 0.02\lambda_o$	$0.05\lambda_o \times 0.04\lambda_o \times 0.05\lambda_o$	$0.45\lambda_o \times 0.34\lambda_o \times 0.06\lambda_o$ / $1.185\lambda_o \times 0.926\lambda_o \times 0.176\lambda_o$	$0.1\lambda_o \times 0.01\lambda_o \times 0.05\lambda_o$ / $0.316\lambda_o \times 0.208\lambda_o \times 0.079\lambda_o$	$0.13\lambda_o \times 0.05\lambda_o \times 0.02\lambda_0$ / $0.816\lambda_o \times 0.32\lambda_o \times 0.16\lambda_o$
Ground-plane Dimensions	$0.12\lambda_o \times 0.12\lambda_o$	$0.2\lambda_o \times 0.2\lambda_o$	$0.25\lambda_o \times 0.36\lambda_o$ / $2.06\lambda_o \times 2.338\lambda_o$	$0.3\lambda_o \times 0.3\lambda_o$ / $0.62\lambda_o \times 0.62\lambda_o$	$0.27\lambda_o \times 0.27\lambda_o$ / $1.6\lambda_o \times 1.6\lambda_o$
Polarization	Linear	Circular	Linear	Linear	Linear
Modes	TM_{010}	TM_{010}	TM_{010} / TM_{001}	TM_{010} / TM_{030}	TM_{010} / TM_{001}
Maximum Realized Gain	3.0 (dBi)	2.5 (dBic)	5.0 / 6.0 (dBi)	2.1 / 5.3 (dBi)	1.4 / 3.1 (dBi)
Impedance FBW	3.6%	4.0%	21.0% / 32.2%	0.8% / 3.4%	3.5% / 7.3%

6.3 Antenna Synthesis and Analysis

It is well known that the standard microstrip patch antenna has a resonant electrical length of about $\lambda/2$ and its electric field is zero at the centre of the patch. Therefore, a shorting plate can be introduced at the centre of the patch, as well as the folding of the ground plane, without significantly affecting the resonant frequency and matching. Based on this miniaturization technique, a three-layer FSP antenna is designed and fabricated. Electric fields are also analyzed in detail to study the operating modes.
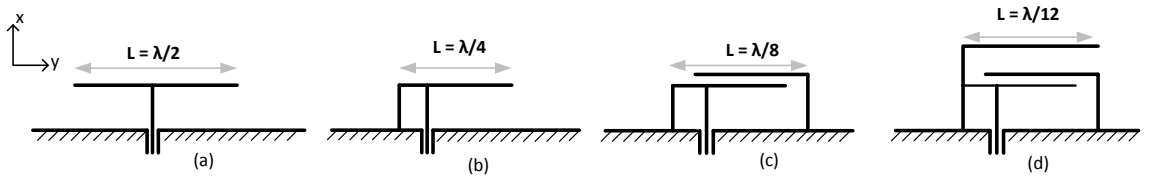
Figure 6.3: Development of the three-layer FSP starting from (a) conventional probe-fed patch antenna. (b) The patch antenna is shorted at the centre of the patch generating a PIFA. (c-d) By folding the ground plane, two and three distinct layers can be achieved.

6.3.1 Geometry of the Folded-Shorted Patch (FSP) Antenna

To design a FSP antenna, the ground plane and shorted patch can be folded twice defining a physical length of $\lambda/12$ defining the formation of the three-layered FSP as shown in Fig. 6.3. The three folded layers can have lengths: L_1, L_2 and L_3 as described in Fig. 6.4(a), and the total height of the conducting part of the antenna can be defined as $H = h_1 + h_2 + h_3$ where h_1, h_2 and h_3 are not equal. L_g characterizes the gap between the folded metallic layers and the metallic side wall, while h_3 defines the radiating slot for the dominant TM_{010} mode. d is the the distance between layer 3 and air. Fig. 6.4(b) shows W_1, W_2 and W_3 which are the widths of the horizontal layers above the ground plane. Throughout the chapter, length is denoted with L (in y direction) and width is denoted with W (in z direction). Dimensions of the designed and optimized FSP antenna are also indicated in Table 6.2.
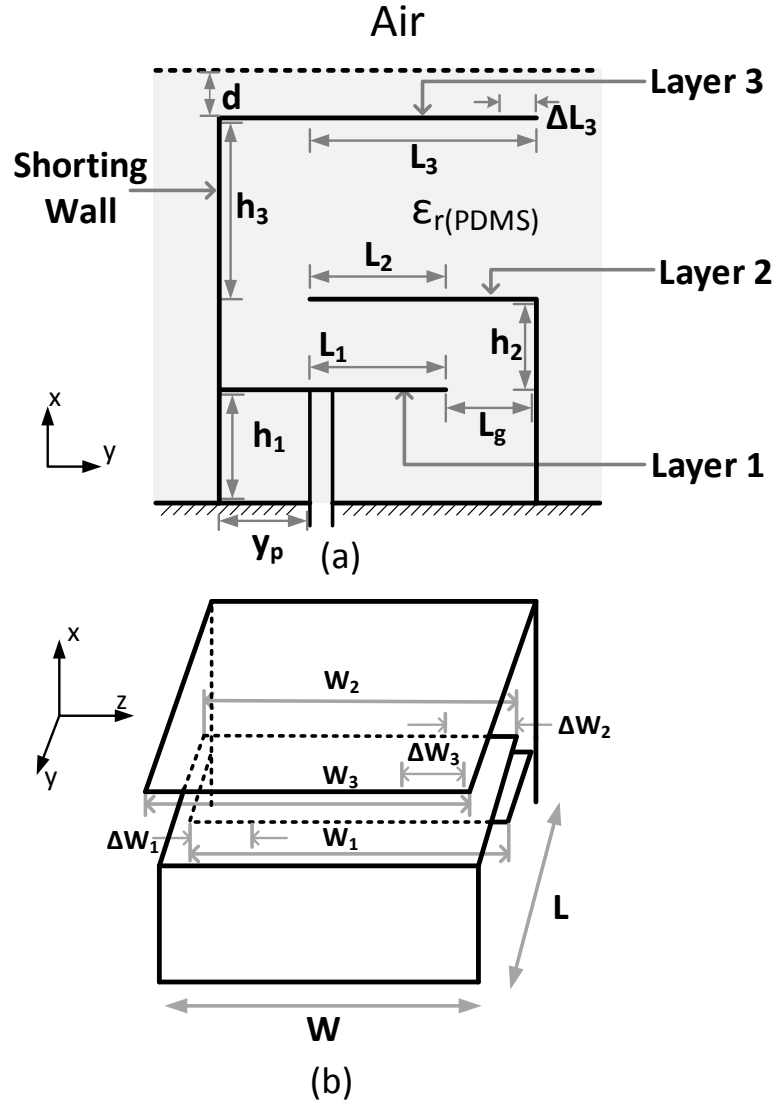
Figure 6.4: (a) A cross-sectional view of a three-layer FSP considering a PDMS substrate. y_p denotes the distance of the probe from the shorting wall in the y-direction. (b) W_1, W_2, and W_3 are the width of the three layers for the FSP. ΔW_1, ΔW_2, ΔW_3 and ΔL_3 are the parameters altered in the tuning analysis [19].

6.3.2 Fabrication of the Folded-Shorted Patch (FSP) Antenna Using Flexible Polydimethylsiloxane (PDMS)

The PDMS material used for the fabrication consists of two parts: polymer elastomer Sylgard 184 and its curing agent [20]. PDMS is initially in liquid form, and this polymer then hardens, is mixed and then cured by heating using its curing agent. Following this approach a multilayer PDMS implementation is able to deliver high robustness and flexibility for the proposed three-layer FSP.

The assembly process consists of five steps. First, the 1 mm top PDMS layer was

Table 6.2: Dimensions of the proposed dual-band three-layer FSP antenna

Parameter	Value (mm)
L_1	32
L_2	32
L_3	38
$W_1 = W_2 = W_3$	40
h_1	5.0
h_2	2.2
h_3	12.7
y_p	5.0
d	1.0
Ground Plane	200×200
Ground Plane (thickness)	0.1

produced (see Table 6.2 and Fig. 6.4). The Sylgard 184 silicone elastomer was mixed with its curing agent. Next, the gelatine PDMS layer was cured in an oven at 60°C for three hours. Once the PDMS hardened, in a second step a three-layered conducting element made of copper foil which is 0.035 mm thick was placed at the centre of the PDMS structure. This conducting element is the folded metallic layers which defines the FSP antenna as illustrated in Fig. 6.4(a). Then, in the third step, the 19 mm PDMS substrate was cured and processed again by following step 1 and then is left in an oven for hardening. At this stage the radiating element is completely embedded within PDMS. Finally, a 0.035 mm thick copper foil, which forms the ground plane was placed on the bottom of the structure. Each layer bonds to the adjacent layer in a natural way after hardening, without any glue or pre-preg.

6.3.3 FSP Antenna Prototype

The FSP antenna prototype was hand-made in a laboratory setting. The dimension of the fabricated antenna is $0.13\lambda_o \times 0.05\lambda_o \times 0.025\lambda_o$ and ground plane size is $0.27\lambda_o \times 0.27\lambda_o$ at 400 MHz. The position of the shorting plates and structure dimensions were optimized in order to improve the matching, bandwidth, and antenna gain at the operating frequencies. Furthermore, the location of the feed was
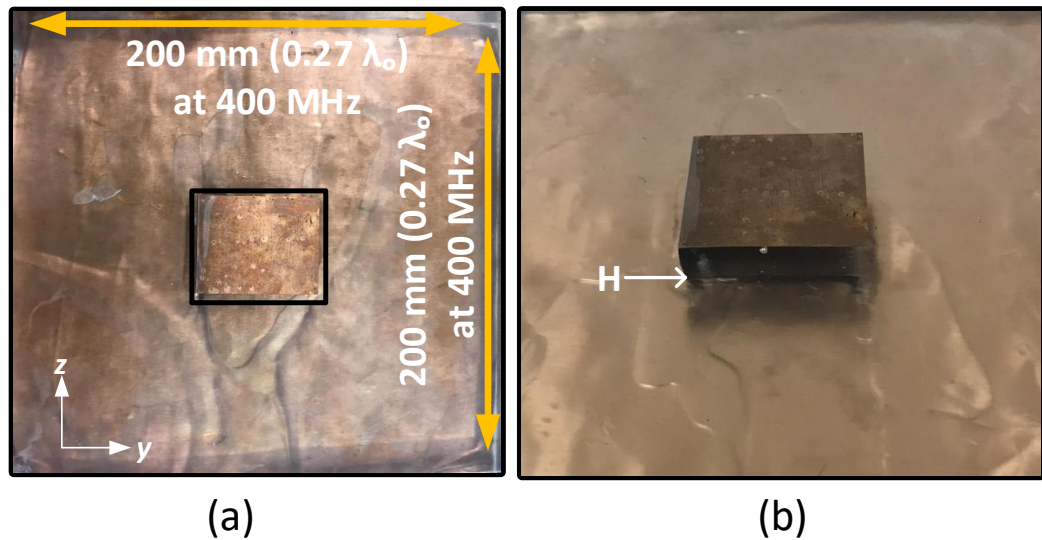
Figure 6.5: Fabricated and measured FSP antenna prototype for UHF and ISM bands communications: (a) top view where the main radiating element is highlighted and (b) perspective side view showing three layer of the FSP [19].

selected to achieve a good 50 Ω impedance matching. PDMS is used as the substrate and its cover such that the antenna is fully embedded as shown in Figs. 6.4 and 6.5. The overall thickness of the PDMS substrate is slightly larger than the FSP for two reasons: it improves impedance FBW [21] and because it is developed for the noted wearable application providing robustness and a stronger mechanical support for the antenna structure when placed on a user and when considering a potentially harsh operating environment.

The ground plane is also larger than the antenna itself because the FSP is meant to be positioned in a bulletproof jacket which has inbuilt metal. Having such a large ground plane creates a simple isolation mechanism and with low cross-polarization levels at the dominant mode. Nowadays, on average the mass of the bulletproof jacket is approximately 15 kg and the prototyped antenna mass is only about 0.9 kg. This potentially is not a major concern for military and emergency response teams since their gear can total up to 23 kg.

6.3.4 Electric Field Distribution

The field configurations for the conventional patch and the FSP cavity models are compared in Figs. 6.6 and 6.7. Based on CST simulations, it is observed that

the electric fields of the FSP antenna is concentrated near the open edges. Figure 6.6(a-d) shows the electric field distribution within the substrate and the radiating element and the ground plane. For the TM_{010} [16] mode the fields undergo a phase reversal along the length (L) of the patch and the FSP but they are uniform along the width (W). This uniform pattern along W contributes significantly to the radiation. The phase reversal along L is important for the antenna to generate a broadside radiation pattern in the far-field [16]. Also, the FSP operating at 400 MHz has a similar electric field pattern to the dominant TM_{010} mode for the conventional patch.
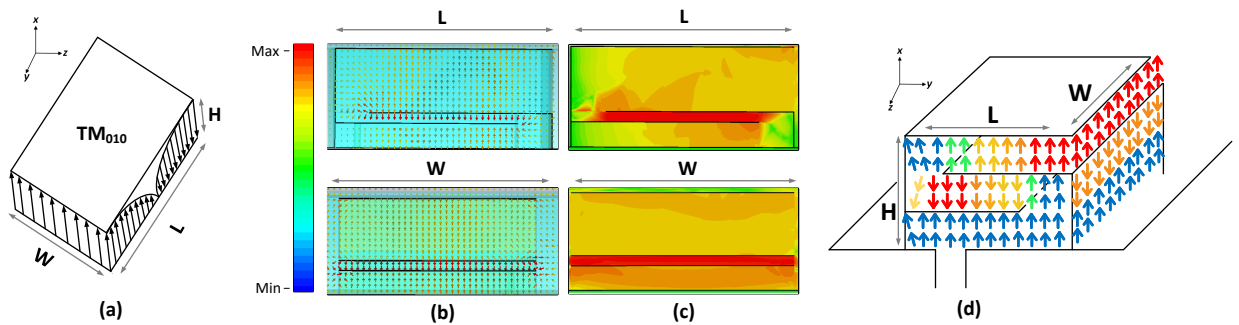
Figure 6.6: (a) Illustration of the electric field for the TM_{010} mode of the conventional patch antenna [16]. (b) The CST simulated electric field (V/m) within the three-layer FSP antenna at 400 MHz. The colour bar defines the strength of the electric field in the different layers. (c) An amplitude representation is shown for the TM_{010} dominant mode of the FSP antenna. (d) Sketched vector electric field pattern of the TM_{010} mode for the FSP antenna. The arrows indicate the phase and magnitude of the current along the length (L) and width (W) of the structure [19].
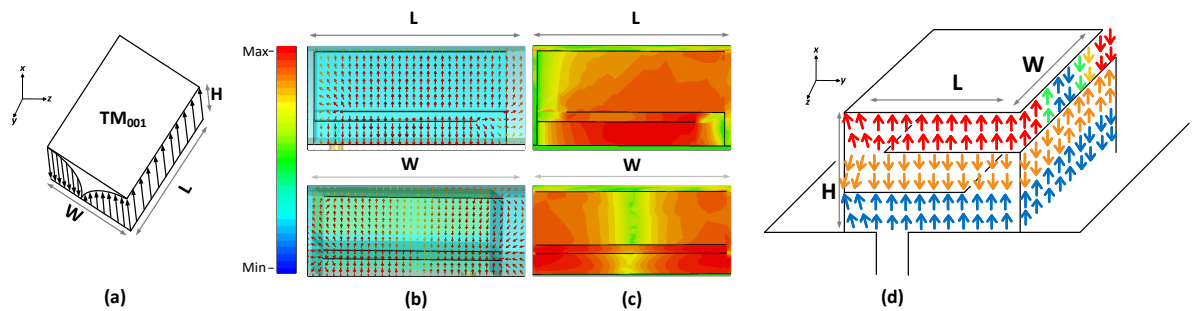
Figure 6.7: (a) Illustration of the electric field for the conventional patch antenna for the higher order TM_{001} [16] mode [16]. (b) The simulated vector electric field (V/m) within the three-layer FSP antenna at 2.4 GHz. (c) An amplitude representation is shown for the TM_{001} [16] higher order mode of the FSP antenna (d) Sketched vector electric field pattern of the TM_{001} [16] mode for the FSP antenna. The arrows indicate the phase and magnitude of the current along the length (L) and width (W) of the structure [19].

For the higher order TM_{001} [16] mode, the electric field pattern is uniform along L

of the patch and the FSP, and the fields are in phase reversal along W as shown in Fig. 6.7(a-d). For the FSP operating at 2.4 GHz, the electric field pattern is similar to the field at the TM_{001} [16] mode. The three-layer FSP operates at the TM_{010} and TM_{001} modes offering broadside radiation and without any slot loading in the top aperture as done in [12] and [15] which can potentially alter the BW and introduce a beam squint.

6.4 Antenna Measurements and Discussions

6.4.1 Reflection coefficient of the FSP Antenna Prototype

The S_{11} results in Fig. 6.8 (a) and (b) suggests that the FSP antenna operates at 400 MHz and at 2.45 GHz, respectively. Both the dominant TM_{010} [16] mode and the higher order TM_{001} [16] mode corresponds to a good matching condition ($S_{11} \leq -10$ dB) at about 400 MHz and 2.45 GHz, respectively, enabling multi-band operation. Moreover, at 400 MHz the FSP antenna is acting as a beacon and does not require a large BW; i.e. a 13 MHz of BW is observed at the dominant mode for both simulations and measurements. Also, the large ground plane of the antenna helps to improve radiation away from the body and a BW of approximately 180 MHz is observed at the higher order mode for the centre frequency at 2.45 GHz.

Due to the folding technique and compactness of the structure, the BW at 400 MHz is relatively narrow. However, by increasing the separation between metallic layers the BW can be increased while maintaining a low profile for the FSP [10]. It should also be mentioned that a minor discrepancy can be observed between the measured and simulated results mainly due to the presence of air bubbles (or air gap) in the fabricated FSP structure as well as slight disagreements between the modelled and the actual relative dielectric constant and loss tangent for the PDMS material, and probe position. Moreover, by altering the loss tangent of PDMS; i.e. by performing parametric simulations in CST, the value of the loss tangent was found to be about 0.0012 which is slightly lower than the initial estimated value. All these factors were taken into consideration during antenna design and optimization. Nonetheless, the S_{11} is still below -10 dB at 400 MHz and at 2.45 GHz.

(a)

(b)
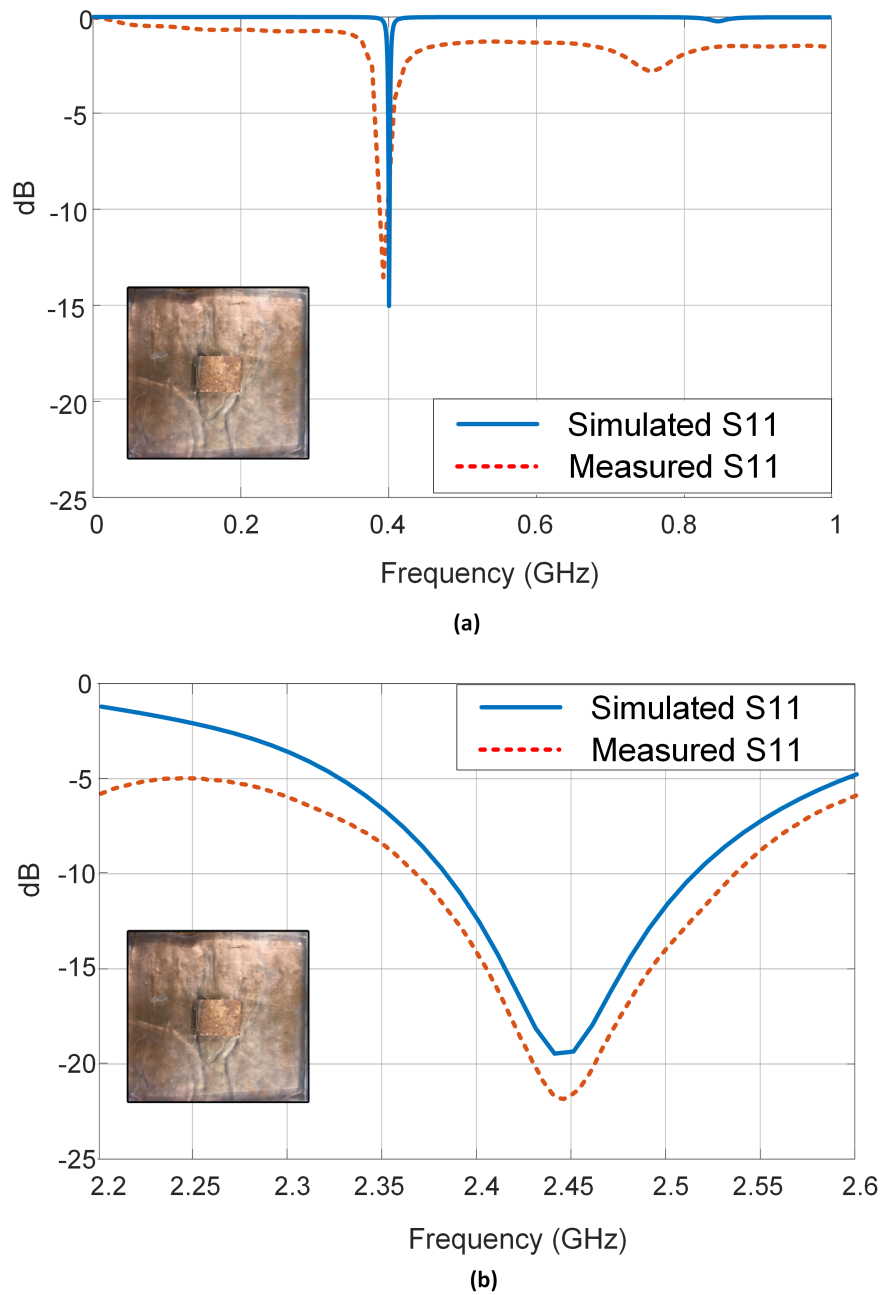
Figure 6.8: Measured and simulated S_{11} of the proposed FSP antenna prototype shown in Fig. 6.5 and compared to CST simulations. (a) 400 MHz (UHF band) and (b) at 2.45 GHz (ISM band) [19].

6.4.2   Radiation Pattern

The background theory on the far-field measurement was reported and dicussed in [16]. The radiation pattern measurements took place inside an anechoic chamber using a Keysight vector network analyzer (VNA) available at Heriot-Watt University and were based on a far-field antenna measurement. Fig. 6.9 shows the setup. Port 1 of the VNA is connected to the horn antenna defined as the transmitting or reference antenna. Port 2 of the VNA is connected to the antenna under test (AUT) as the receiver. The VNA is set to acquire S_{21} measuring the radiation pattern from Port
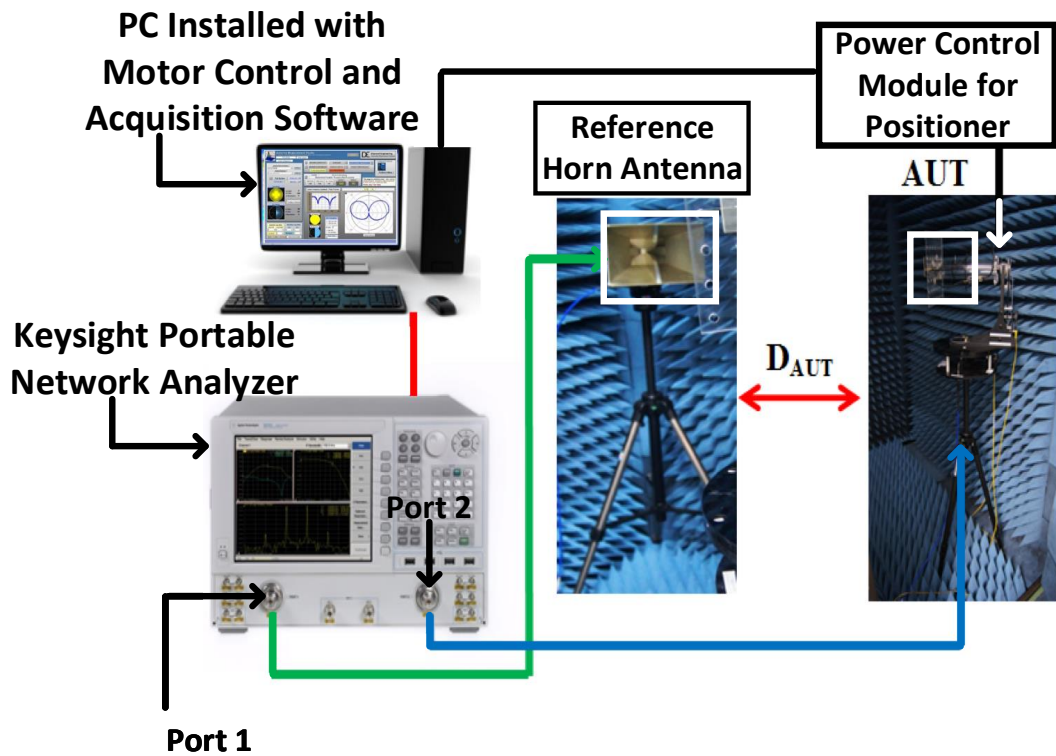
Figure 6.9: Illustration of the radiation pattern measurement system inside the anechoic chamber at Heriot-Watt University [19].

1 to Port 2, while the VNA is linked to the computer via USB cable. The AUT and horn antenna are separated with a distance of D_{AUT}. The AUT is rotated 360° in a single plane during the polar radiation pattern measurement.
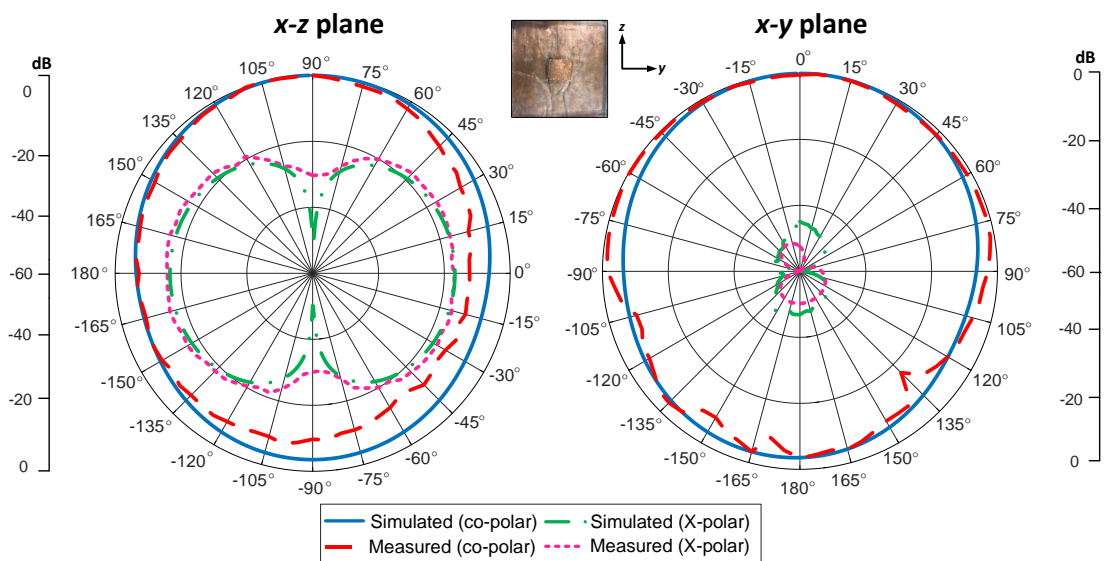
Figure 6.10: Three layer FSP antenna where beam patterns in both the xz- and yz- planes are shown at 400 MHz for the dominant TM_{010} mode. Cross polarization levels are also shown and are more than 20 dB below the main co-polarized maximum at broadside [19].
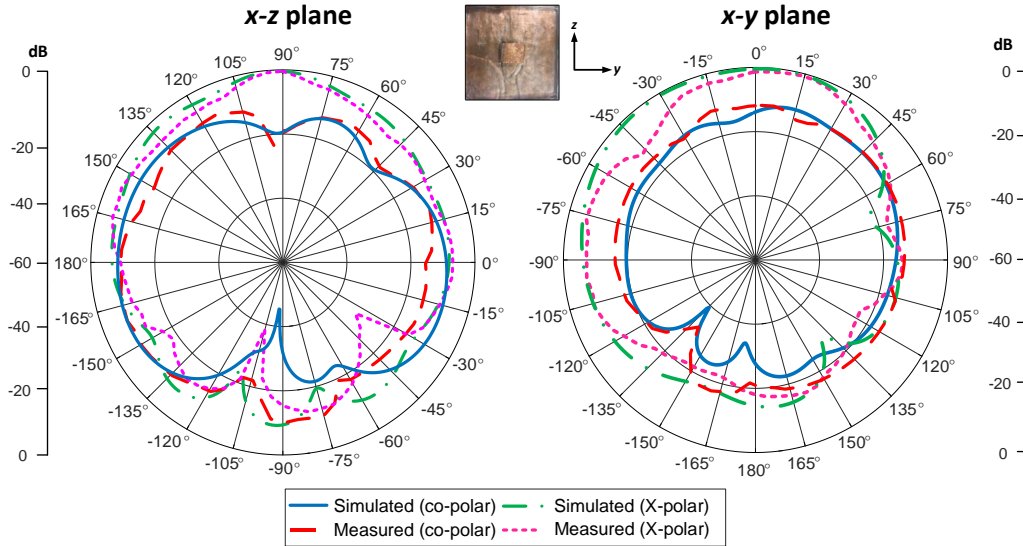
Figure 6.11: Three layer FSP antenna where beam patterns in both the xz- and yz- planes are shown at 2.4 GHz for the higher order TM_{001} mode. It should be mentioned that the co-polar and cross-polar field values are defined by the fundamental TM_{001} mode [19].

The xz- plane and the xy- plane radiation patterns at 400 MHz are shown in Fig. 6.10 for the dual-band antenna operating at the TM_{010} mode [16]. The simulated and measured peak cross-polarization levels are at least 20 dB below the main co-pol maximum at broadside. Similarly, at 2.45 GHz (TM_{001} [16] mode), the radiation patterns in the xz- and yz- planes are shown in Fig. 6.11. It is worth noting that there is a change in the polarization in comparison with the dominant TM_{010} [16] mode.

At 2.45 GHz when the FSP antenna operates in the TM_{001} [16] mode, the beam pattern is abrupt and directive. This is due to the equal substrate and ground plane size. On the other hand, the broadside pattern shown in recent FSP antennas (previously reported designs) operated by the TM_{030} [16] mode [12], [15]. This is due to the following reasons: (a) the substrate used is truncated at the edge of the radiating element or has no substrate that limits the generation of magnetic currents at the edges, resulting in low electric fields between the radiating element and ground plane, and (b) introduction of slots that minimizes the effect of grating lobes ensuring a single beam with one dominant main lobe and not like the multi-beam pattern plot in Fig. 6.2 for the TM_{030} [16] mode.

The peak realized gain of the antenna measured in free space is 1.40 dBi and 3.20 dBi at 400 MHz and 2.4 GHz, respectively. Since the FSP antenna is designed

for wearable applications, the specific absorption rate (SAR) is another important parameter to consider. For example, the values of SAR were simulated to be 0.14 W/kg and 1.06 W/kg at 400 MHz and 2.45 GHz, respectively, when considering a human phantom. Also, these SAR values are much lower than the maximum limit set by the Council of the European Union (2.0 W/kg). The simulated realized gain of the FSP antenna when placed on human body at 400 MHz and 2.4 GHz are 1.37 dBi and 3.10 dBi, respectively. This suggests that the realized gain is not significantly affected by the human body.

Table 6.3: Comparison of Realized Gain and Radiation Efficiency (Simulation) of the Proposed FSP Antenna in Free-Apace and On-Body

Frequency (GHz)	Realized Gain (dBi) Sims/Meas (Free-Space)	Radiation Efficieny (%) Sims (Free-Space)	Relaized Gain (dBi) Sims (On-Body)	Radiation Efficiency (%) Sims (On-Body)
0.4	1.50/1.40	54	1.37	50
2.4	3.40/3.20	70	3.10	65

The simualated radiation efficiency of the FSP antenna in free space is 54% and 70% at 400 MHz and 2.4 GHz, respectively, and when the antenna is on human body it is 50% and 65%. Table 6.3 outlines the simulated and measured realized gain at 400 MHz and 2.4 GHz in free-space along with simulated radiation efficiency. The simulated realized gain and radiation efficiency when antenna is place on-body are compared with free-space values (see Table 6.3). The antenna could be considered to have a low efficiency and realized gain at the dominant mode but this is not a major concern since the FSP is acting as a beacon antenna requiring low data rates. At 2.4 GHz, the realized gain and efficiency achieved is efficient for WiFi communications as similar efficiency and gain values were reported for wearable antennas. For example, in [22] and [23] wearable antennas were designed at 2.45 GHz and the radiation efficiency when antenna is placed on body was reported to be 22% and 26%, respectively.

6.5 FSP Antenna Optimization

6.5.1 Tuning Procedure

A tuning procedure is also reported here to optimize antenna matching and radiation performance at the operational frequency. This study is important to facilitate the understanding of the relevant design parameters needed to tune within the FSP for designers interested to replicate this work, quickly change the resonant frequency or introduce some active elements. For example, should TM_{001} operation be required at 2.4 GHz while antenna operation needs to be varied from about 400 MHz to another frequency. The width W_2 can be altered by ΔW_2 with a 5 % variation from its original size and keeping W_3 constant. In Table 6.4, it can be observed that the resonant frequency of the higher order mode is constant (at 2.4 GHz) but the resonant frequency of the dominant mode is tuned around 400 MHz.

Table 6.4: Widths Variation for Layers 2 and 3 for Constant TM_{001} Mode (see Fig. 6.4)

W_3 (mm)	ΔW_2 (mm)	TM_{010} Mode Best Matching (MHz)	$\lvert S_{11}\rvert$ [dB]	TM_{001} Mode Best Matching (GHz)	$\lvert S_{11}\rvert$ [dB]
40	38	404.6	-12.03	2.40	-13.20
40	39	402.2	-13.90	2.40	-14.73
40	40	401.0	-12.82	2.40	-15.03
40	41	399.0	-11.55	2.40	-16.91
40	42	398.0	-13.30	2.40	-17.43

Table 6.5: Length Variation for Layer 3 for Constant TM_{010} Mode (see Fig. 6.4)

L_3 (mm)	ΔL_3 (mm)	TM_{010} Mode Best Matching (MHz)	$\lvert S_{11}\rvert$ [dB]	TM_{001} Mode Best Matching (GHz)	$\lvert S_{11}\rvert$ [dB]
40	0	401.0	-16.95	2.46	-21.55
41	1	401.0	-14.45	2.39	-21.20
42	2	401.0	-12.80	2.35	-21.66
43	3	401.0	-12.15	2.30	-21.16

A similar procedure was performed for L_3 which was altered by ΔL_3. It can be observed that the dominant mode frequency is constant but the higher order mode frequency changes. These variations are reported in Table 6.5. Hence, the tuning procedure suggests that the higher or lower frequency can be controlled independently while keeping one of the operating frequencies constant.
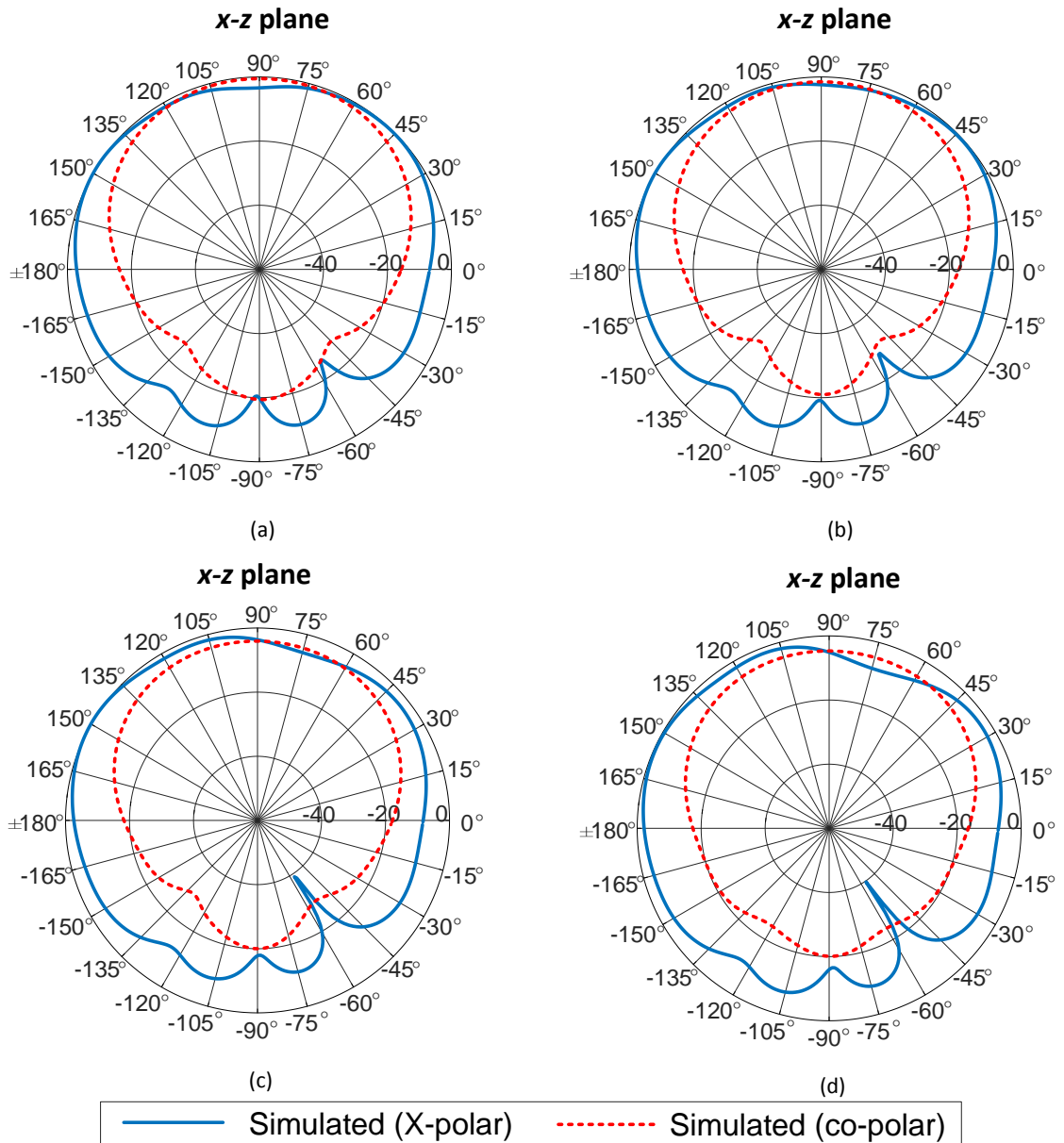
6.5.1.1 Structure Optimization

Figure 6.12: Beam pattern for the three-layer FSP antenna at 2.4 GHz for different substrate (PDMS) dimensions in the xy- plane for the TM_{001} higher order mode.(a) 60×60 mm, (b) 100×100 mm, (c) 140 $times$ 140 mm, and (d) 180×180 mm

In addition, for the FSP an analysis of the beam pattern was done by increasing

the substrate size beyond the radiating element. The substrate size was increased gradually until its size same as the ground plane size. Fig. 6.12 shows beam patterns at the range of different substrate sizes. It is observed that the size of substrate is influencing the beam pattern as compared to beam pattern of the cavity model where the substrate size is truncated to the edges of the radiating element. The reason this analysis was done because the proposed FSP antenna is a wearable antenna and has substrate size equivalent to ground plane to provide robustness to the structure.

An analysis on the size of the ground plane and height of the proposed FSP antenna was also carried out. The size of the ground plane was reduced up to 30% keeping the height of the antenna at 30 mm. The radiating element of the antenna was fixed at the centre. It was observed that the realized gain of the antenna was decreased and also the matching of antenna 400 MHz was worse. Same trend was noted for 2.4 GHz frequency band. Table 6.6 sumarizes the results from this analysis.

Table 6.6: Summary Results of Simulated Ground Plane Size Variation at 400 MHz

Ground Plane Size (mm)	Height (mm)	S_{11} (dB)	Realized Gain (dBi)
140 × 140	30	-6.80	0.4
150 × 150	30	-6.50	0.5
160 × 160	30	-7.60	0.6
170 × 170	30	-8.50	0.8
180 × 180	30	-10.20	0.9
190 × 190	30	-11.50	1.2

6.6   Summary

In this chapter, the fabrication and measurement of a dual-band three-layer FSP antenna operational at the TM_{010} (400 MHz) and the TM_{001} (2.4 GHz) modes. The major dimensions of the FSP prototypes are $0.27\lambda_o \times 0.27\lambda_o \times 0.025\lambda_o$ based on the lower design frequency of 400 MHz. Also, the reported measurements are generally in close agreement with the simulated results. Radiation is at broadside for 400 MHz and 2.4 GHz and maximum realized gain values of 1.4 and 3.0 dBi are observed, respectively. The FBW of the antenna can be improved by increasing the thickness of the FSP antenna or by introducing slots as mentioned in [12] but this will increase

the overall size of the antenna and its design complexity which might not be suitable. The radiation performance of the developed PDMS-based and low-profile FSP, when operating both in free-space and when placed on a human phantom, suggests that the antenna can be suitable for wearable applications such as military search and rescue operation and emergency services where antenna robustness is important.

References

[1] J. R. James, A. J. Schuler, and R. F. Binham, "Reduction of antenna dimensions by dielectric loading," *Electronics Letters*, vol. 10, no. 13, pp. 263–265, June 1974.

[2] T. Lo, Y. Hwang, E. Lam, B. Lee *et al.*, "Miniature aperture-coupled microstrip antenna of very high permittivity," *Electronics Letters*, vol. 33, no. 1, pp. 9–10, 1997.

[3] J. S. Colburn and Y. Rahmat-Samii, "Patch antennas on externally perforated high dielectric constant substrates," *IEEE Transactions on Antennas and Propagation*, vol. 47, no. 12, pp. 1785–1794, Dec 1999.

[4] W.-S. Chen, "Single-feed dual-frequency rectangular microstrip antenna with square slot," *Electronics Letters*, vol. 34, no. 3, pp. 231–232, Feb 1998.

[5] K.-P. Yang and K.-L. Wong, "Inclined-slot-coupled compact dual-frequency microstrip antenna with cross-slot," *Electronics Letters*, vol. 34, no. 4, pp. 321–322, Feb 1998.

[6] K.-L. Wong and K.-P. Yang, "Compact dual-frequency microstrip antenna with a pair of bent slots," *Electronics Letters*, vol. 34, no. 3, pp. 225–226, Feb 1998.

[7] J. L. Volakis, C.-C. Chen, and K. Fujimoto, *Small antennas: miniaturization techniques & applications.* McGraw-Hill New York, 2010, vol. 1.

[8] Z. Li and Y. Rahmat-Samii, "Optimization of PIFA-IFA combination in handset antenna designs," *IEEE Transactions on Antennas and Propagation*, vol. 53, no. 5, pp. 1770–1778, May 2005.

[9] R. Li, G. DeJean, M. M. Tentzeris, and J. Laskar, "Development and analysis of a folded shorted-patch antenna with reduced size," *IEEE Transactions on*

Antennas and Propagation, vol. 52, no. 2, pp. 555–562, Feb 2004.

[10] S. K. Podilchak, M. Caillet, D. Lee, Y. M. M. Antar, L. C. Y. Chu, J. Cain, M. Hammar, D. Caldwell, and E. Barron, "A compact circularly polarized antenna using an array of folded-shorted patches," *IEEE Transactions on Antennas and Propagation*, vol. 61, no. 9, pp. 4861–4867, Sept 2013.

[11] A. Holub and M. Polivka, "A novel microstrip patch antenna miniaturization technique: A meanderly folded shorted-patch antenna," in *2008 14th Conference on Microwave Techniques*, April 2008, pp. 1–4.

[12] K. L. Lau, K. C. Kong, and K. M. Luk, "A miniature folded shorted patch antenna for dual-band operation," *IEEE Transactions on Antennas and Propagation*, vol. 55, no. 8, pp. 2391–2398, Aug 2007.

[13] R. Joshi, C. Constantinides, S. K. Podilchak, M. N. Ramli, H. Lago, and P. J. Soh, "Robust and compact PDMS antennas for search and rescue operations and emergency communications," in *12th European Conference on Antennas and Propagation (EuCAP 2018)*, April 2018, pp. 1–5.

[14] R. Joshi, C. Constantinides, S. K. Podilchak, and P. J. Soh, "Dual-band folded-shorted patch antenna for military search and rescue operations and emergency communications," in *2018 18th International Symposium on Antenna Technology and Applied Electromagnetics (ANTEM)*, Aug 2018, pp. 1–2.

[15] D. E. Brocker, Z. H. Jiang, M. D. Gregory, and D. H. Werner, "Miniaturized dual-band folded patch antenna with independent band control utilizing an interdigitated slot loading," *IEEE Transactions on Antennas and Propagation*, vol. 65, no. 1, pp. 380–384, Jan 2017.

[16] C. A. Balanis, *Antenna theory: analysis and design*. John wiley & sons, 2016.

[17] S. Maci and G. B. Gentili, "Dual-frequency patch antennas," *IEEE Antennas and Propagation Magazine*, vol. 39, no. 6, pp. 13–20, 1997.

[18] D. M. Pozar, *Microwave engineering*. John Wiley & Sons, 2009.

[19] R. Joshi, S. K. Podilchak, D. E. Anagnostou, C. Constantinides, M. N. Ramli, H. Lago, and P. J. Soh, "Analysis and design of dual-band folded-shorted patch

antennas for robust wearable applications," *IEEE Open Journal of Antennas and Propagation*, pp. 1–1, 2020.

[20] D. Corning, "Sylgard 184 silicone elastomer," *Technical Data Sheet*, 2008.

[21] R. Garg, P. Bhartia, I. J. Bahl, and A. Ittipiboon, *Microstrip antenna design handbook*. Artech house, 2001.

[22] A. Ruaro and J. Thaysen and K. B. Jakobsen, "Wearable Shell Antenna for 2.4 GHz Hearing Instruments," *IEEE Transactions on Antennas and Propagation*, vol. 64, no. 6, pp. 2127–2135, June 2016.

[23] S. Su and Y. Hsieh, "Integrated Metal-Frame Antenna for Smartwatch Wearable Device," *IEEE Transactions on Antennas and Propagation*, vol. 63, no. 7, pp. 3301–3305, July 2015.

Chapter 7

Conclusion

This thesis has investigated new antenna and transmission line designs for wearable applications. Two dual-band wearable antennas, one based on polymer material and the other on textile material have been introduced. An antenna operating at the TM_{001} mode, which is broadside and easy to design compared to the TM_{030} mode, was also analysed. In addition, two new state-of-the-art flexible transmission line designs, which are low cost, flexible and lightweight, were presented.

In Chapter 1 literature review and background theory was discussed. It can be concluded that wearable antennas have been significantly investigated in last two decades, with applications related to various sectors. Wearable antennas are lightweight, low cost, flexible, robust and resilient to harsh environmental conditions. They can also be designed in different shapes and sizes, which allow their designs to be more versatile. A detailed analysis on various flexible substrates available in the literature has been discussed and compared. Advantages of integrating metasurfaces, such as EBG and AMC, and the challenges faced whilst performing on-body measurements have been discussed. Designs were focused on a wearable antenna which can operate at UHF and ISM band frequencies, and can be an alternative to complex designs present in current literature. These complex designs also exploited higher order TM_{030} modes which have unwanted nulls.

Flexible transmission lines were also reviewed. From this review, the importance of a flexible transmission line which is an alternative to rigid or semi-rigid comerically available cables was highlighted.

In Chapter 2, a new flexible coaxial cable has been designed, simulated, fabricated and presented. Two prototypes were manufactured, one using polyester (PES) and the other using polytetrafluoroehtylene (PTFE). The performance and analysis of the two prototyped cables were presented in this chapter. The compact and low profile textile coaxial cables posses a low reflection coefficient in the UHF and ISM band frequencies. The measured and simulated S_{11} is less than -10 dB for the PES sample 1 and the PTFE samples 1 and 2. It was observed that the S_{21} of the PES sample 1 is above -2 dB up to 3.5 GHz. Comparatively, the PTFE sample 2 has a S_{11} below -10 dB up to 6 GHz, and the S_{21} is above -2 dB up to 5.5 GHz. The cables were designed for wearable applications. The robustness tests, such as bending and wet tests, were analyzed to measure the performance of the cables in a harsh environment and the shielding effectiveness of the prototype was measured using an electromagnetic compatibility test. The shielding test was performed using three different antennas, each operating at three different frequency bands. The EMC test showed that the cable has a shielding effectiveness below -40 dB. DC analysis of the inner and outer conductors for the fabricated prototypes showed they were in close agreement with commercial cables. It can be concluded from these finding that the fabricated cables are eligible for wearable applications.

In Chapter 3, a wearable antenna was developed using the most common type of planar antenna. A single layer circular polarized patch antenna, using PDMS substrate, for military search and rescue operations and emergency services was design and fabircated. The antenna is lightweight (57.8 g), compact ($0.4\lambda_o \times 0.4\lambda_o \times 0.02\lambda_o$) and was manufactured in-house at Heriot-Watt University, and thus low cost. The antenna operates at 2.45 GHz which enables it to be used for Wi-Fi related applications. The robustness study carries out in this thesis, concludes that PDMS qualifies as a flexible (bend up to 40°), robust (antenna fully encapsulated inside PDMS) and temperature resilient, in a wide range (-20°C to 100°C), material. The antenna also has broadside radiation pattern and works well when inside a bulletproof jacket which makes it suitable for the military application.

In Chapter 4, a wearable textile antenna, with dual-band and dual-sense charac-teristics, which was designed for location tracking purposes using GPS in outdoor and WLAN in indoor environments [1]. The dual-band antenna, originated from a square patch, was integrated with slits and truncated corners to operate in the

1.575 GHz band (with circular polarization) and the 2.45 GHz band (with linear polarization). To alleviate body coupling in the dual-band antenna, an AMC plane with a 3×3 array of unit cells was integrated behind the radiating patch. The AMC unit cells were designed based on a square patch with rectangular slits on each side, and a square ring for operation at 2.45 GHz. The generated fractional impedance bandwidth in the lower and upper bands is 27% and 7.5%, respectively, with a 9% 3 dB axial ratio bandwidth in 1.575 GHz. The realized gain at 1.575 GHz and 2.45 GHz are 1.98 dBic and 1.94 dBi, respectively. The performance of the antenna was measured when bent and also when placed on-body. The overall specific absorption rate (SAR) of the antenna was 0.12 W/kg, which is below the regulatory limit 2.0 W/kg. Through this work it was that AMC plane arrays have been validated to significantly reduce the SAR and front-to-back ratio (FBR) in comparison to the antennas without the AMC plane.

In Chapter 5, a cavity model analysis of the patch and FSP antenna. The cavity model analysis was applied to compare the fields radiated by the conventional patch and FSP antenna. For first time the cavity model has been applied to predict the behaviour of multi-layer FSPs. The analysis was done on the dominant TM_{010} mode and the higher order TM_{001} mode for both antennas. Modal analysis and design equations, supported by the cavity model, were presented for the conventional patch antenna. The reported numerical model and its supporting results, will help the antenna engineer to estimate the operational frequency bands for the relevant modes, pattern shapes, polarization, and directivity values prior to any simulation and fabrication activity. This helps to reduce the design and optimization time for the antenna engineer. A comparison of the numerical results and full-wave simulations are included to support these findings [2,3].

In Chapter 6, a miniaturized and flexible folded-shorted patch (FSP) antenna with dual-band functionality for wearable applications was designed and fabricated. The fabricated antenna is operational at 400 MHz (TM_{010}) and 2.4 GHz (TM_{001}) and can be considered compact for the lower operational frequency band. No other work on FSPs has reported similar antenna performance in terms of compact size and similar impedance bandwidth at the UHF band. The fabricated FSP antenna is low-profile and compact for integration into a bullet-proof jacket. The ground of antenna is large but there are also many benefits in making use of the large effective

ground plane that is made possible by the bulletproof jacket, in that it will foster electromagnetic isolation between the user and the radiating fields generated by the antenna (reducing SAR) while also improving the cross polarization levels.

The FSP antenna in this work exploits TM_{010} and TM_{001} modes. This has never been done previously for FSP type structures. Other published work in the literature exploits TM_{030} mode for the FSP, which is a higher order patch mode. The beam pattern plot for the TM_{030} mode shows a multi-beam pattern, and this type of field configuration is unwanted for communication applications. Other work in the literatures use slots to perturb the current path reducing side lobes and force a typical patch-like pattern for the TM030 mode. On the contrary, fabricated FSP antenna in this thesis, is very easy to fabricate, and without additional slots for pattern correction. This makes the design process simpler for the antenna engineer.

Flexible PDMS was used as the substrate due to its relatively low-cost as well as its flexibility and robustness for wearable applications. The dimensions of the FSP prototypes are $0.27\lambda_o \times 0.27\lambda_o \times 0.025\lambda_o$. The reported measurements are in close agreement with the simulated results. Radiation is at broadside for 400 MHz and 2.4 GHz and maximum realized gain values of 1.4 and 3.0 dBi are observed, respectively. The radiation performance of the developed PDMS-based and low-profile FSP, when operating both in free-space and when placed on a human phantom, suggests that the antenna is suitable for wearable applications such as military search and rescue operations and for emergency services, where antenna robustness is important.

In general, research and development work carried out in this thesis demonstrates novel and cost-effective approaches to designing wearable antennas and their components. The new design analysis will allow antenna engineers to estimate the directivity and far-field beam patterns of FSP antennas before simulation. Flexible textile coaxial cables have introduced the possibility of more compact designs for transmission lines.

7.1   Future Work

The proposed implementation has many advantages but also many possibilities for future improvement and potentially for a new design. The topics covered in this

thesis can be potentially expanded to the followings:

• Textile Transmission Line

In Chapter 2, the proposed textile cable is not very desirable for a very wet environment. This issue can be solved by developing a more robust design that can sustain the performance of the cables in wet conditions. Also, it was observed that the outer conductor of the cables has gaps that can be further analyzed and develop for a potential textile based leaky feeder antenna.

• Wearable Antennas

In Chapter 3, the thickness of the polydimethylsiloxane (PDMS) substrate is 20 mm which makes it difficult to bend after approximately 45°. The proposed height was chosen for two reasons: (1) to increase the bandwidth and (2) to co-locate the PDMS patch antenna within the proposed folded-shorted (FSP) antenna. A thinner substrate will provide more degree of freedom towards the flexibility of the overall antenna.

In Chapter 6, a more miniaturized design can be achieved by integrating an AMC surface within the proposed FSP antenna structure. This will help to reduce the specific absorption rate (SAR) and radiation towards the human body. Also, an optimization can be done to make the proposed FSP a wideband wearable antenna depending on the future evolving technologies. Furthermore, an analysis can be done using different polymer-based materials such as polyester or polyamide. They both have high strength of flexibility, are water-resistant and are lightweight. The FSP antenna proposed in the thesis has linear polarization which can be modified to circular polarization depending on the application.

Also, the E-shaped multiband patch antennas proposed in [4] will be further modified to use as a wearable antenna using a PDMS substrate.

References

[1] R. Joshi, E. F. N. M. Hussin, P. J. Soh, M. F. Jamlos, H. Lago, A. A. Al-Hadi, and S. K. Podilchak, "Dual-band, dual-sense textile antenna with amc backing for localization using GPS and WBAN/WLAN," *IEEE Access*, vol. 8, pp. 89 468–89 478, 2020.

[2] R. Joshi and P. J. Soh, "Dual-band folded-shorted patch antenna for military search and rescue operations and emergency communications," in *2018 18th International Symposium on Antenna Technology and Applied Electromagnetics (ANTEM)*, 2018, pp. 1–2.

[3] R. Joshi, S. K. Podilchak, D. E. Anagnostou, C. Constantinides, M. N. Ramli, H. Lago, and P. J. Soh, "Analysis and design of dual-band folded-shorted patch antennas for robust wearable applications," *IEEE Open Journal of Antennas and Propagation*, vol. 1, pp. 239–252, 2020.

[4] A. G. Koutinos, D. E. Anagnostou, R. Joshi, S. K. Podilchak, G. A. Kyriacou, and M. T. Chryssomallis, "Modified easy to fabricate e-shaped compact patch antenna with wideband and multiband functionality," *IET Microwaves, Antennas Propagation*, vol. 12, no. 3, pp. 326–331, 2018.